NANO-OPTICS-ENABLED HIGH-EFFICIENCY SOLAR CELLS

by

Myungji Kim

B.S. in Electrical and Computer Engineering, Korea University, 2008

M.S. in Electrical and Computer Engineering, Korea University, 2010

Submitted to the Graduate Faculty of

Swanson School of Engineering in partial fulfillment

of the requirements for the degree of

Doctor of Philosophy

University of Pittsburgh

2014

UNIVERSITY OF PITTSBURGH

SWANSON SCHOOL OF ENGINEERING

This dissertation was presented

by

Myungji Kim

It was defended on

July 2nd, 2014

and approved by

Dietrich W. Langer, Ph.D., Professor Emeritus, Department of Electrical and Computer

Engineering

William E. Stanchina, Ph.D., Professor, Department of Electrical and Computer Engineering

Guangyong Li, Ph.D., Assistant Professor, Department of Electrical and Computer

Engineering

Thomas E. McDermott, Ph.D., Assistant Professor, Department of Electrical and Computer

Engineering

Sung Kwon Cho, Ph.D., Associate Professor, Department of Mechanical Engineering and

Materials Science

Dissertation Director: Hong Koo Kim, Ph.D., Professor, Department of Electrical and

Computer Engineering

NANO-OPTICS-ENABLED HIGH-EFFICIENCY SOLAR CELLS

Myungji Kim, PhD

University of Pittsburgh, 2014

Glancing angle coupling of light into dielectric media is a desirable feature that can benefit the performance of solar cells. At a highly refractive dielectric interface, however, the transmission angle is limited small (e.g., ~15 deg for air/Si) by Snell's law. In this thesis, we propose a new method of light coupling that overcomes the conventional limits of refractive transmission. A vertical dipole structure is designed to enable glancing propagation into high-index media, enhancing light absorption and carrier collection for a given thickness of active medium. A vertical-dipole nano-optic structure was introduced to a conventional finished silicon cell (~16% efficiency). The vertical dipoles reradiate incident light into oblique directions inside the active medium (Si). The glancing propagation along the junction interface results in a synergistic, uncompromised improvement of cell performance (i.e., enhancing photocarrier generation without sacrificing carrier transport) and demonstrates 20% cell efficiency. We have further studied low-voltage, broadband photocarrier multiplication in a graphene/SiO_2/Si structure and demonstrate external quantum efficiency 146-200% (internal quantum efficiency 218-384%) as measured with photocurrent in UV-to-NIR (325-850nm). The self-induced electric field (~10^6 V/cm) in 2D electron gas enables impact ionization at low bias (< 2V), in a way promising and compatible with photovoltaic operation.

TABLE OF CONTENTS

LIST OF TABLES

PREFACE

This thesis would not have been possible without generous support, helpful guidance and good wishes from others. First and foremost, I would like to express my eternal appreciation to my advisor, Dr. Hong Koo Kim. It has been an honor and privilege to be his student. I am immensely grateful to him for his thoughtful guidance, encouragement, and inspiration throughout my doctoral program. Furthermore, I express a sincere gratitude to the members of my dissertation committee, Dr. Dietrich W. Langer, Dr. William E. Stanchina, Dr. Guangyong Li, Dr. Thomas E. McDermott, and Dr. Sung Kwon Cho, for their taking time to serve on my committee and giving me invaluable comments and suggestions on this dissertation.

I would also like to thank my colleagues, Siyang Liu and Daud Emon, and former colleagues, Dr. Yun-Suk Jung, Dr. Yonggang Xi, Dr. Dongxiao Li, Dr. Siwapon Srisonphan, Jinxuan Wu, I-Hung Ting and Zhenlv Han. I enjoyed sharing ideas and thoughts with them, and fun moments together.

Lastly, I would like to thank my family and parents, Jungho Kim and Youngim Cho, for their encouragement and support. They have provided great guidance in life and supported me in all my pursuits. And I would like to express my great appreciation to my husband, Sehyuk Yim, for his unfailing love, faithful support and patience during my doctoral period.

1.0   INTRODUCTION

Solar photovoltaics has achieved a total capacity of 136 GW worldwide in 2013 [1], becoming the third of the installed capacity of renewable energy sources behind hydro and wind power. Compared to hydro and wind power requiring a large scale set-up, solar energy can be easily deployed at home or business places. Furthermore, solar power is a non-polluting, clean, reliable and renewable energy source. Due to these reasons, photovoltaics has been the field of extensive research and development.

Silicon is the most commonly used material for photovoltaic applications because of its abundance, low cost, reliability and maturity. The performance of solar energy conversion is determined by various factors such as light trapping/absorption and carrier transport/collection processes. High-efficiency cells require careful design and control of both materials and device structures to attain maximum efficiency. From the material's perspective, the refractive index of Si is high (~3.9), therefore a bare surface of Si shows relatively high reflectance (~35 %). The absorption coefficient of Si is not large enough in most part of solar spectrum, and this requires a significant amount of thickness of Si substrate or film for full absorption of incident light. Figure 1.1 shows the reflectivity and absorption coefficient of Si over a broad range of wavelength.

1
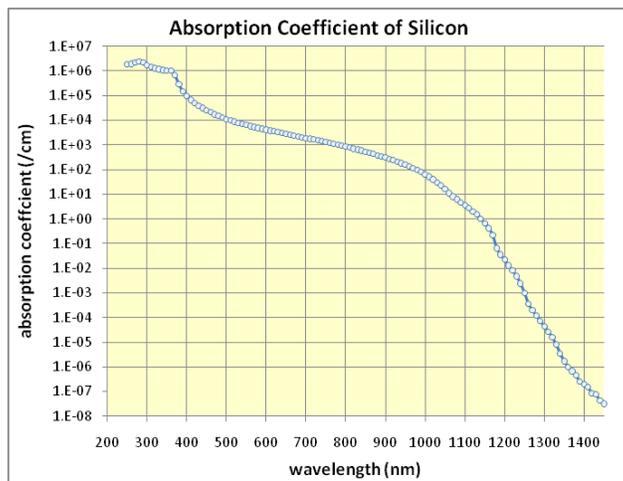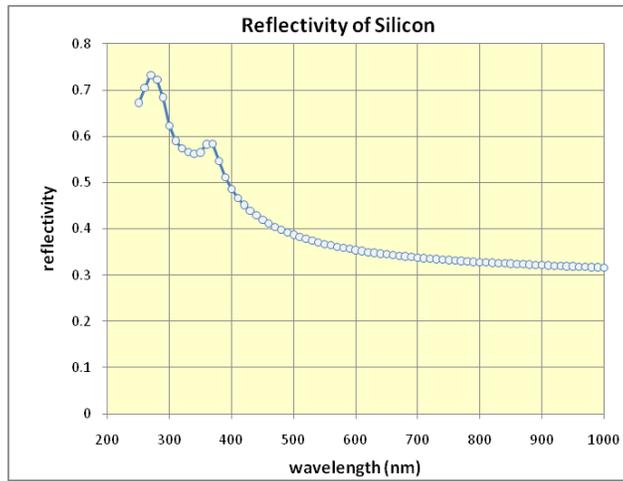
Figure 1.1 Reflectivity and absorption coefficient of silicon. [2]

Minimizing reflection losses over a solar spectrum and a wide range of incident angles is an essential requirement for high efficiency solar cells, and a variety of surface structures have been developed to this end [3-16]. A common approach is adding antireflection (AR) coatings based on destructive interference in quarter-wavelength-thick-dielectric layers. Such AR coatings, however, exhibit a satisfactory performance only in a narrow spectral range and for specific incident angles. Micron-scale textures, such as pyramids of several micron base width chemically etched on crystalline Si, can provide an AR effect mainly via geometric optics, that is, giving a reflected light at a pyramidal facet a second chance to enter another pyramid. The pyramid-textured surfaces are usually coated with an AR layer to further reduce reflection (and also to provide surface passivation). Figure 1.2 shows the passivated emitter, rear locally diffused (PERL) cell having "inverted" pyramidal structure on the surface, formed by anisotropic etching of (100)-oriented silicon. Pyramidal structure can reduce the reflection of external incident light and induce higher reflection of internal incident light returning from back surface [17]. The pyramidal texturing, however, cannot be applied to thin film solar cells because of the relatively large size of texture. The size of pyramids is typically 10 μm, while the thickness of thin silicon film is usually 1-2 μm. Many complicated processes such as soaking in KOH solution are also needed to get textured surface. Furthermore, AR coatings offer only a limited improvement of the spectral and angular performances.

Nanoscale-textured Si, i.e., a density-graded surface, often called 'black Si', can also provide an AR effect and can be applied to thin-film cells [12-16]. Such structures can take a randomly nanoporous morphology or moth-eye texture composed of nanoscale periodic structures. Such nanostructured surfaces can provide a better AR effect compared to conventional AR coatings in terms of spectral and angular performance, but they commonly

3

suffer from high recombination losses due to the large surface area of nano-textured Si [12-16, 18-19].
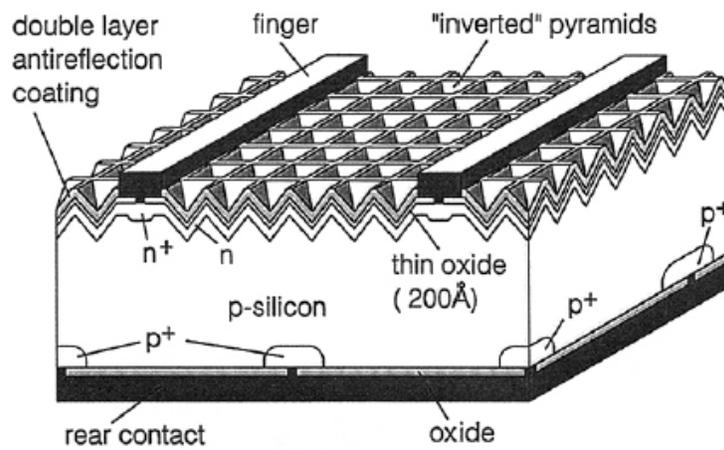
Figure 1.2 The typical PERL (passivated emitter, rear locally-diffused) cell with the efficiency

of 24%. [20]

In this thesis we explore a new method of light coupling into the active layer of solar cell that is designed to enhance fundamental photovoltaic processes such as light absorption and photocarrier collection, thereby the overall conversion efficiency. In the proposed device structures, an array of nanoscale vertical steps introduced on the emitter surface enable glancing-angle coupling of light into the active layer. Investigation of this vertical nano-optic structure is motivated by our recent finding that the radiation pattern of a nanoslit aperture can be customized to orient to oblique direction by tilting the dipole axis to the substrate normal. An array of such vertical-dipoles implemented by vertical nano-texturing is utilized in altering the way that an incident light interacts with a dielectric interface, overcoming the conventional refraction limit. High-throughput, oblique transmission of light into a high-index active layer can be achieved for a wide range of incident angle.

With glancing angle transmission/propagation, most light can be absorbed near/along junction interface. Besides absorption enhancement, the photo-carrier collection is also expected to improve, a feature particularly important for thin-film solar cells where the materials quality (e.g., minority carrier diffusion length) practically limits the maximum thickness of active layer. The solar panels based on the proposed nano-optic-textured cells will be suitable for mounting in a 3D configuration, and can generate constant output power for an extended period of time of a day, promising for urban/residential area, building-integrated photovoltaic applications.

In Chapter 1, the management of light and the operation of photovoltaic cells will be reviewed. Chapter 2 describes the concept of a vertical-dipole nano-optic structure by simulating radiation patterns of vertical dipole in a different medium. The optical and electrical characteristics of holographically fabricated one-dimensional (1D) nano-mesa structures on the surface of solar cells will be discussed in Chapter 3. Two-dimensional (2D) nano-mesa structures

applied to a finished c-Si cell using thin Ag or TiO$_2$ film for nonlithographic, self-organized island formation will be optically and electrically analyzed in Chapters 4 and 5. Chapter 6 reports a further study on low-voltage (<~2V) broadband photocarrier multiplication in a graphene/SiO$_2$/Si structure, which may enable a potentially very high efficiency solar cell operation. Finally, conclusions of this thesis will be summarized in Chapter 7.

1.1 LIGHT MANAGEMENT

1.1.1 Photon flux [21]

In order to reduce the volume of cell material for lower cost and to improve the performance for better efficiency, photon flux density in photovoltaic cells should be increased. Let's assume a semiconductor layer with thickness of w on a similar semiconductor substrate as shown in figure 1.3. For light normally incident on the cell surface, some part of it will be reflected (R), some will be absorbed and some will pass through the substrate. The photon flux density of energy E at a depth of x within the cell is given by

$$b(E,x) = (1 - R(E))b_s(E)e^{-\int_0^x \alpha(E,x')dx'} \tag{1.1}$$

where $b_s(E)$ is the incident photon flux density normal to the surface, $R(E)$ is the reflectivity of the surface and $\alpha(E,x)$ is the absorption coefficient of the semiconductor layer at x. When all absorbed photons lead to band gap excitation, the rate of electron-hole pair generation is

$$g(E,x) = \alpha(E,x)b(E,x) = (1 - R(E))\alpha(E,x)b_s(E)e^{-\int_0^x \alpha(E,x')dx'} \tag{1.2}$$

per unit volume.

For a cell with thickness w, an absorbed fraction of incident photons is

$$f_{abs} = 1 - R(E) - \frac{b(E,w)}{b_s(E)} \tag{1.3}$$

A fraction passed through is

$$f_{trans} = \frac{b(E,w)}{b_s(E)} \tag{1.4}$$

For a uniform absorber, each fraction is given by

7

$$f_{abs} = (1 - R(E))(1 - e^{-\alpha(E)w}) \tag{1.5}$$

$$f_{trans} = (1 - R(E))e^{-\alpha(E)w} \tag{1.6}$$

When αw is small, for wavelength close to the band gap or for indirect semiconductor such as silicon, the unused fraction is high.

It is desirable maintaining $R(E)$ and $b(E, w)$ as small as possible in order to maximize absorption of light in the active layer for efficient light utilization. The photogeneration rate would increase if $b(E, x)$ could be increased within the cell. Then, we could achieve the same photogeneration rate with a smaller volume, reducing the requirements of materials.

$\beta(E, r, \theta, \phi)$ is the spectral photon flux density, that is, the number of photons of energy E that pass through unit area per unit solid angle per unit time. For material having volume of V and surface of S, conservation of photons requires

$$\int_S \beta(E, s, \theta, \phi) d\Omega \cdot dS = \int_v (g_{ph}(E, r) - u_{ph}(E, r)) dV \tag{1.7}$$

where s is a point on the surface, $g_{ph}(E, r)$ is the rate of photon emission and $u_{ph}(E, r)$ is the rate of photon absorption per unit volume. $u_{ph}(E, r)$ can be defined as net absorption, which means the difference between absorption and stimulated emission. Based on Gauss's law, at any point within the volume V,

$$\int_\Omega \nabla \cdot \beta(E, s, \theta, \phi) d\Omega = g_{ph}(E, r) - u_{ph}(E, r) \tag{1.8}$$

The photon absorption rate for a given flux direction is proportional to β, the magnitude of the photon flux in that direction. The photon emission rate is proportional to the magnitude of the emitted flux. Therefore,

$$u_{ph}(E, r) = \int_\Omega \alpha(E, r) \beta(E, r, \theta, \phi) d\Omega \tag{1.9}$$

where α is the absorption coefficient at r

$$g_{ph}(E,r) = \int_\Omega \varepsilon(E,r)\beta_e(E,r,\theta,\phi)d\Omega \tag{1.10}$$

where ε is the emission coefficient and β_e is the emitted flux density.

From (1.8) to (1.10),

$$\nabla \cdot \beta = \varepsilon\beta_e - \alpha\beta \tag{1.11}$$

$$\frac{d\beta}{dl} = \varepsilon\beta_e - \alpha\beta \tag{1.12}$$

where l is the length coordinate along (θ, φ) [Chandrasekhar, 1950].

The emitted flux induced from the carrier radiative recombination is usually negligible in real materials, therefore,

$$\frac{d\beta}{dl} + \alpha\beta = 0 \tag{1.13}$$

When the $\theta = 0$ and $\varphi = 0$, that is, the incident flux propagates normal to the surface, $\beta = b(E,x)$ and the equation (1.13) becomes

$$\frac{d\beta}{dl} + \alpha b = 0 \tag{1.14}$$

and

$$b(E,x) = b(E,0)e^{-\int_0^x \alpha(E,x')dx'} \tag{1.15}$$

This is known as the Beer-Lambert law. $b(E, x)$ represents the flux at depth x directing normal to the surface of planar structure.

There are several ways to increase photon flux; concentrating the light, trapping the light or exploiting of photon recycling. In a real solar cell, anti-reflection coating is used to reduce reflection. Also, concentration of light can increase incident photon flux density. Confining the light helps internal reflection (light trapping) and reabsorption of photons created from radiative recombination helps recycling photons.
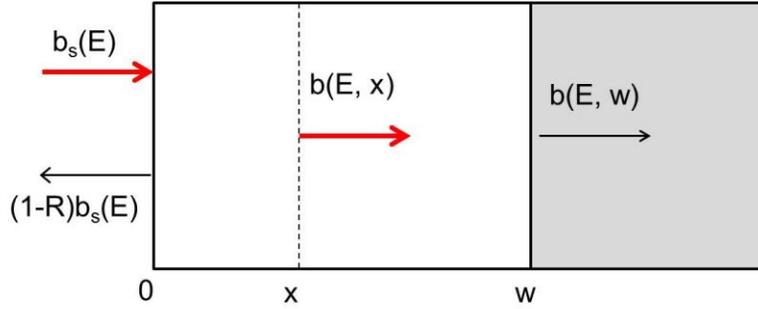
Figure 1.3 Attenuation, transmission and reflection of incident light in a semiconductor layer of active width w.

1.1.2 Minimizing reflection [21]

1.1.2.1 Optical properties of semiconductors

The dielectric constant ε_s describes the optical properties of a solid material. ε_s is a complex number which is given by

$$\sqrt{\varepsilon_s} = n_s - i\kappa_s \qquad (1.16)$$

where n_s is the material refractive index and κ_s is associated with the material absorption coefficient, that is,

$$\alpha = \frac{4\pi\kappa_S}{\lambda} \qquad (1.17)$$

ε_s, n_s and κ_s are dependent on wavelength and may also depend on direction. The reflection and transmission of light at the interface between two materials are determined by the ratio of two

refractive indices. Assume that light is striking the plane interface between materials with refractive index n_0 and n_s at normal incidence, the reflectance is determined as

$$R = (\frac{n_0 - n_s}{n_0 + n_s})^2 \qquad (1.18)$$

The refractive index (n_s) of semiconductor is typically $3 - 4$ at visible wavelength. Based on the equation (1.18), the reflectance from free space to semiconductor surface should be in the range of $30 - 40$ %.

At oblique incidence, assuming that θ_0 is the angle between incident light and the normal axis of surface and θ_s is the an angle between transmitted light and the normal axis of surface, then

$$R = (\frac{\eta_0 - \eta_s}{\eta_0 + \eta_s})^2 \qquad (1.19)$$

where

$$\eta_s = n_s \sec\theta_s \qquad (1.20)$$

for p-polarized light (magnetic field vector normal to the plane of incidence) and

$$\eta_s = n_s \cos\theta_s \qquad (1.21)$$

for s-polarized light (electric field vector normal to the plane of incidence)

According to the Snell's law,

$$n_0 \sin\theta_0 = n_s \sin\theta_s \qquad (1.22)$$

The reflectance for unpolarized light corresponds to the average reflectance of s- and p-polarized light, and increases from minimum at normal incidence to maximum (≈ 1) at large angle. Reflectance of $30 - 40$ % at normal incidence for silicon is quite high for photovoltaic applications.

At an angle greater than the critical angle (θ_c), light travelling within the semiconductor to the surface is internally reflected. For an air-semiconductor interface, θ_c is given by

$$\theta_c = \sin^{-1}(\frac{n_0}{n_s})$$ (1.23)

θ_c is 16.9° for the air-silicon interface.

1.1.2.2 Anti-reflection coatings

An anti-reflection (AR) coating, dielectric thin film(s), is used to reduce the reflection at air-semiconductor interface. Consider an AR coating with refractive index n_1 that is placed between semiconductor with refractive index n_s and air (free space) with refractive index n_0 (Fig. 1.4). The reflectance of the AR-coated surface is now expressed as

$$R = \frac{(\eta_0 - \eta_s)^2 + (\eta_0 \eta_s / \eta_1 - \eta_1)^2 \tan^2 \delta_1}{(\eta_0 + \eta_s)^2 + (\eta_0 \eta_s / \eta_1 + \eta_1)^2 \tan^2 \delta_1}$$ (1.24)

where δ_1 is the phase shift in a film, that is,

$$\delta_1 = \frac{2\pi \eta_1 d_1 \cos \theta_1}{\lambda}$$ (1.25)

where θ_1 is the angle between the incident light and the normal within the film and d_1 is the thickness of film. When $\delta_1 = \pi/2$, the reflectance R becomes minimum. At normal incidence, d should be quarter wavelength ($\lambda/4$) in the thin film to get the first minimum R. R goes to zero when it also satisfies

$$n_1 = \sqrt{n_0 n_s}$$ (1.26)

With a semiconductor coated with a thin dielectric layer of refractive index $\sqrt{n_s}$, the reflectivity can be reduced to zero at particular wavelength λ_0. λ_0 is usually chosen to be in the middle of wavelength range that can be efficiently absorbed for that semiconductor. Near λ_0, R increases

with wavelength approximately $(\Delta\lambda/\lambda_0)^2$. R approaches maximum at wavelengths where the phase shift is equal to multiple of π. As a result, AR coating that is optimized at one visible wavelength might be highly reflective at other wavelength. Reflectivity of AR coating depends not only on wavelength but also incident angle. This can be a limitation of AR coating. By the way, since the absorption of most semiconductor at visible wavelength is relatively small ($\kappa_s \ll n_s$), the absorption of the optical material is neglected in the above explanation of AR coating.

The refractive index of optimal AR coating material for silicon and GaAs should be around 1.84 and 1.90 from the equation (1.26). Silicon nitride ($n_1 = 1.97$) and tantalum oxide ($n_1 = 2.1$) are good candidates for AR coating materials resulting in less than 1% reflectivity at normal incidence at optimum wavelength.

Two or more layers of thin AR films can be used to improve reflectivity over a broad range of wavelength. However, multilayer AR coating increases the manufacturing cost, so double layers are used for higher efficiency solar cells. Assuming that the refractive index of each layer is increasing from air (n_0) to first coating (n_1) to second coating (n_2) to semiconductor (n_s), reflectivity vanishes when first and second layer have the thickness of quarter-wave and

$$(\frac{n_2}{n_1})^2 = \frac{n_s}{n_0} \tag{1.27}$$

This gives more flexibility for choosing the AR coating materials than the single layer case. In conclusion, the purpose of AR coating is to reduce reflectivity R, and so increase the photon flux density (Equation 1.1) and generation rates (Equation 1.2).
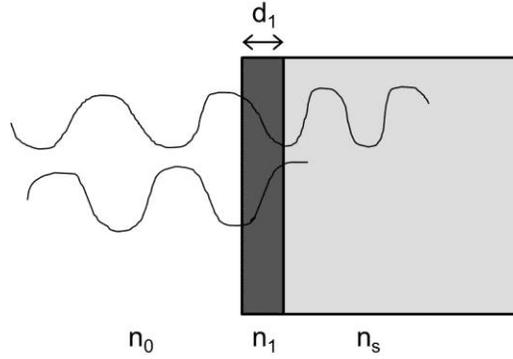
Figure 1.4 Single layer AR coating.

1.1.3 Concentration [21]

To reduce the cost of photovoltaic conversion system, incident light can be concentrated, that is, light in large area is concentrated on a cell in small area. A concentration factor X is given by the collection and cell areas ratio. Incident flux density can be increased by X in the concentration system.

The concentration of incident light means expanding the range of angles crossed by the source. Assume that a spherical concentrator focuses sunlight by a concentration factor X. The angular range will be increased to θ_x and the total incident flux will be enhanced by a factor

$$X = \frac{\int_0^{2\pi}\int_0^{\theta_X} d\Omega}{\int_0^{2\pi}\int_0^{\theta_s} d\Omega} = \frac{\sin^2\theta_X}{\sin^2\theta_{sun}} \qquad (1.28)$$

where θ_{sun} is 0.26°, the half angle subtended by the sun source. Compared to the unconcentrated case, the flux normal to the surface is increased by the factor of X in concentrated case because most light coming in the semiconductor is directed close to the normal. At normal incidence,

14

$$b(E,x) = (1 - R(E)) X b_s(E) e^{-\int_0^x \alpha(E,x')dx'} \qquad (1.29)$$

The rate of generation (Eq. 1.2) is also increased by the factor X. A geometrical factor which occurs from integrating over the relevant range of angles can be written by

$$F_X = \pi \sin^2 \theta_X = X \sin^2 \theta_{sun} \qquad (1.30)$$

When θ_X is 90 °, X is 46050 and the maximum theoretical concentration happens. The maximum concentration is lower in cylindrical than in spherical symmetry ($X = 1/\sin \theta_{sun}$).

1.1.4   Light confinement [21]

1.1.4.1 Light paths

Unlike AR coating which increases the fraction of photons entered into the cell or concentration of light which increases the incident photon flux, light confinement increases the length of path of photons inside the cell. By increasing the path length of photons, photogeneration per incident photon can be increased. When structures are larger than the coherence length of light and light rays do not interfere, light trapping concept can be considered. In micron scale structure such as silicon cells, light is considered as coherent. In addition, interference becomes important factor and photogeneration rate should be calculated by the gradient of the Poynting vector.

Within the cell, scattering and reflection of light rays is involved in light trapping. The entered light ray will travel along one of the paths, P_i, which is dependent on geometry of cell. The total flux at some point in the cell can be calculated by summation of contributions for different paths. The relevant photogeneration quantity is the light absorption rate (Eq. 1.9)

$$u_{ph}(E,r) = \alpha(E,r) \sum_{P_i} \beta_i(E,r,\theta_i,\phi) \qquad (1.31)$$

where the integral over angle is changed to a sum over paths and β_i is the photon flux at r from the direction (θ_i, φ_i). Equation (1.2) should be replaced for photogeneration calculation based on Eq. (1.31). However, determining the β_i at a general point is not easy due to the different history of rays. Therefore, we approach with 'ray tracing' to get the total absorbed flux which comes from absorption along the length of each ray path.

$$f_{abs} = \frac{(1-R(E))}{b_s(E)} \left\{ 1 - R(E) - \sum_i \beta_i(E,0) \exp\left(-\alpha(E) \int_{P_i} dl_i\right) \right\} \qquad (1.32)$$

where the integral is taken over the path of ray from entry to exit, l_i is a length co-ordinate along the path P_i and $\beta_i(E,0)$ is the ith ray flux at the starting point of path that satisfies

$$\sum_{P_i} \beta_i(E,0) = (1-R(E))b_s(E) \qquad (1.33)$$

Higher attenuation of the ray and higher f_{abs} can be achieved by longer ray path. The average path length

$$<l> = \sum_{P_i} \beta_i(E,0) \int_i dl_i \, / \sum_{P_i} \beta_i(E,0) \qquad (1.34)$$

is compared to evaluate different light trapping schemes. The path length is related to cell geometry and the probabilities of reflection and transmission, but not related to the probabilities of photon absorption.

1.1.4.2 Mirrors

The mirror reflects more than 95% of rays so that it is used at the rear surface of thin-film solar cells to reflect admitted light inside the cell. Since a good performance cell has low reflectivity at the surface, the rear mirror doubles the path length of ray. For an ideal mirror having $R = 1$ and ideal front cell surface having $R = 0$, the path length becomes $2w$ (Fig 1.5).

16

If $\theta_s > \theta_c$, which means if rays travel the front surface at a wider angle than the angle they are admitted, total internal reflection occurs and we can achieve light trapping. In that case, light will not escape from the cell and be reflected back for another double pass.
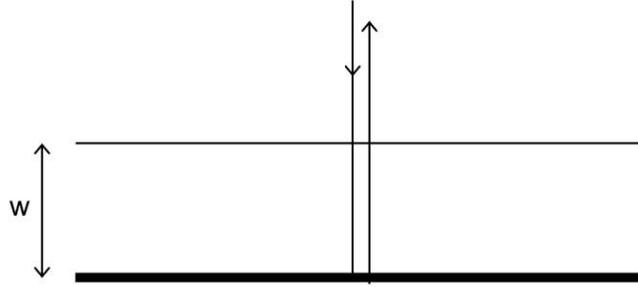
Figure 1.5 Double path-length in a rear mirror cell.

1.1.4.3 Randomizing surfaces (Lambertian surface)

Lambertian surface, a perfectly randomizing surface, is used as a roughened surface so the light can be scattered or randomized. At normal incidence, the light goes into the cell and is scattered at the rear surface. As we discussed in 1.1.4.2, the average path length of reflected light back to front surface will be twice of cell width.

$$< l >= \frac{w}{< \cos \theta_s >} = 2w \tag{1.35}$$

Now, only $\frac{1}{n_s^{2}}$ of the rays with $\theta_s < \theta_c$ can escape the cell, the rest rays will be reflected from the surface and be scattered again at the rear surface making a second path length $2w$. The mean path length of light rays before leaving the cell is sum of each path length for the number of times they scattered.

$$< l >= \frac{1}{n_s^{2}} \times 2w + \frac{1}{n_s^{2}} \times (1 - \frac{1}{n_s^{2}}) \times 6w + \frac{1}{n_s^{2}} \times (1 - \frac{1}{n_s^{2}})^{2} \times 10w + \cdots \tag{1.36}$$

17

For the first pass (normal incidence) and the last pass (only small θ_s can escape), the path length is w while for other intermediate passes, the path length is $2w$. When the order goes to infinity, Eq. (1.36) is simplified as,

$$< l >= (4n_s^2 - 2)w \approx 4n_s^2 w \qquad (1.37)$$

Therefore, the effective absorption enhancement factor is $4n_s^2$ in semiconductor at normal incidence. For silicon or GaAs, the number of $4n_s^2$ is around 50, which is promising for light trapping systems. [Lush, 1991].

Even though Lambertian surface is desirable for light trapping system, the surface cannot be perfectly randomized in a real application. Therefore, more practical techniques such as regular geometrical texturing are used for light trapping.
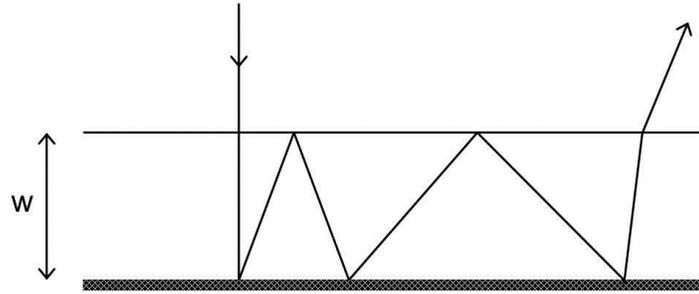
Figure 1.6 Ideally randomized rear surface.

1.1.4.4 Textured surfaces

Regarding a simple structure of light trapping, rear surface tilted with an angle θ_{tilt} relative to the planar front surface can be considered. For $\theta_{tilt} > \frac{1}{2}\theta_c$, normally incident light will be reflected from the rear surface at an angle greater than θ_c and be totally reflected at the front surface. In the case that positive and negative tilt angles are the same, a multiple of four passes

18

occurs from each ray. A 'double bounce' is the worst case. The mean path length of ray is given by

$$< l > \geq 2(1 + \sec 2\theta_{tilt})w \geq 4w \qquad (1.38)$$

Higher path length is given by higher tilt angles and longer textured faces and a higher probability of multiple passes is given by shallower angles.

Front surface texturing also can enhance the path length as the rear surface case. The angle that normally incident rays hitting the textured surface are refracted into the cell is

$$\gamma = \theta_{tilt} - \sin^{-1}(\frac{\sin \theta_{tilt}}{n_s}) \qquad (1.39)$$

In a symmetrical texturing case, the ray striking the front surface on a face will propagate to the opposite tilt face and leave the cell. As a result, only a double pass occurs in this symmetrical texturing (Figure 1.7 (a)).

$$< l > \geq 2w \sec \gamma > 2w \qquad (1.40)$$

In an asymmetrical texturing case, however, a four passes path occurs at certain tilt angle shown in figure 1.7 (b). In general, more light trapping occurs when the surface texturing is low order symmetry. For example, 3D pyramidal structure scatters more than 2D groove structure.
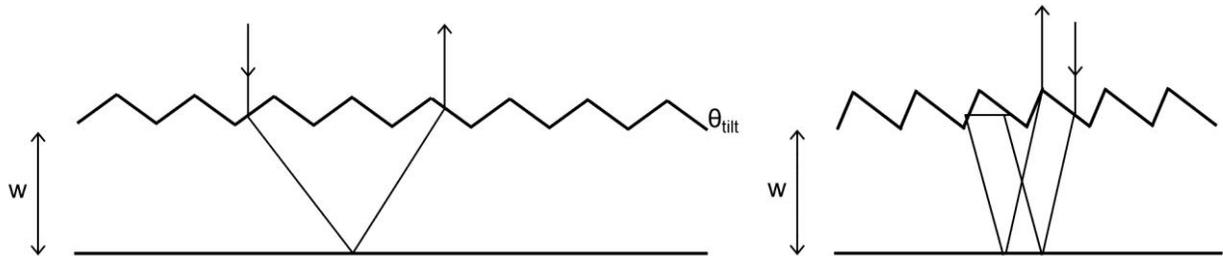
Figure 1.7 (a) Reflection path in a symmetrically textured surface (b) Four passes of light in an asymmetrically textured surface.

1.2   SOLAR CELL OPERATION

1.2.1   Solar cell principle

Solar cell is an electrical device that converts the energy of sunlight into electricity. For a solar cell operation, photocarrier generation and carrier separation/transport/collection are two fundamental processes. If the energy of photons is greater than that of band gap, electron-hole pairs can be generated in the cell. Since photogenerated electrons and holes can exist only for the duration of minority carrier lifetime, the carriers should be collected by the p-n junction before they disappear through a recombination process. If the solar cell is connected to an external circuit, carriers will flow in the external circuit producing a photocurrent.

1.2.2   Solar cell parameters

The *I-V* characteristic of the cell can be approximated as a superposition of the short circuit photocurrent and the dark current shown in equation 1.40. [22] Notice that the *I-V* curve shifts as the light generated current contributing generating power.

$$J = J_{SC} - J_0(e^{\frac{qV}{k_B T}} - 1) \tag{1.40}$$

When there is no current flow in the cell, the potential difference becomes maximum which is the open circuit voltage, V_{oc}.

$$V_{OC} = \frac{kT}{q}\ln(\frac{J_{SC}}{J_0} + 1) \tag{1.41}$$

There are several parameters that are indicative of solar cell performance, but the most important, commonly referred figure-of-merit is the efficiency of photovoltaic conversion, also

called solar cell efficiency. The cell efficiency can be calculated from the short-circuit current (I_{sc}), the open-circuit voltage (V_{oc}), the fill factor (FF) and the input power (P_{in}).

The short-circuit current is the current flowing through a cell when the voltage across the cell is zero. The open-circuit voltage is the maximum voltage from a cell when the current through the device is zero (equation 1.41). The short-circuit current and the open-circuit voltage are important factors that determine the cell efficiency. Figure 1.8 illustrates a typical *I-V* characteristic of a solar cell and the points corresponding to I_{sc} and V_{oc} are marked.

The fill factor (FF) is determined as the ratio of the maximum power from a solar cell to the product of the short-circuit current and the open-circuit voltage. The FF is graphically defined as a measurement of the "squareness" of the *I-V* curve regarding Figure 1.8.

$$FF = \frac{V_{MP} I_{MP}}{V_{OC} \cdot I_{SC}} \tag{1.42}$$

where V_{MP} and I_{MP} are voltage and current at maximum power. The FF is limited by parasitic resistive losses mainly caused by series and shunt resistance.

The cell efficiency is defined as the ratio of output power from the cell to input power.

$$P_{max} = V_{MP} \cdot I_{MP} = V_{OC} \cdot I_{SC} \cdot FF \tag{1.43}$$

$$\eta = \frac{V_{OC} \cdot I_{SC} \cdot FF}{P_{in}} \tag{1.44}$$

From the equation (1.44), three parameters, V_{oc}, I_{sc} and FF are expected to have high values to achieve high efficiencies.

In real cell, two parasitic resistances can be involved resulting in the degradation of cell efficiency. One is series resistance (R_s) which arises from resistive contact. Shunt resistance (R_{sh}), also called parallel resistance, comes from leakage currents around the edges of the cell. The FF is strongly affected by series and shunt resistance; thereby the area of the maximum

power can be reduced for lower conversion efficiency. Maintaining the series resistance as small as possible and the shunt resistance as large as possible are the key issues for high-efficiency photovoltaic cells.
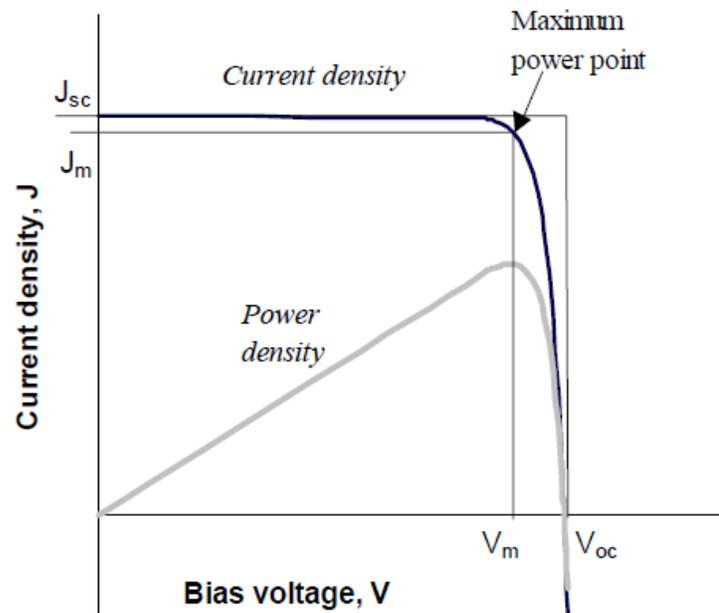
Figure 1.8 Current versus voltage graph showing open-circuit voltage (V_{oc}), short-circuit current (I_{sc}) and fill factor (FF) [21].

2.0   ANALYSIS OF VERTICAL DIPOLE FOR GLANCING RADIATION

2.1   INTRODUCTION

A solar cell operation involves a two-step process, light absorption (therefore, photocarrier generation) followed by carrier separation/transport/collection, and both steps need to be of high throughput for high efficiency cells. Reducing reflection losses usually results in enhanced absorption of light in a cell. The way that an incident light couples into a cell, however, is critically important since it can further enhance both light absorption and carrier transport depending on the transmission angle. Glancing coupling, for example, effectively increases the path length (therefore absorption) of light in a given thickness of active layer. Oblique propagation of light along the junction interface also results in photocarrier generation near/around the junction so that carrier separation/transport/collection becomes easier/better than normal propagation case.

Transmission of light at a dielectric interface is governed by the ratio of refractive indices of media. In the air/Si case, for example, the transmission angle is limited small (~15 deg), and even with AR-coating the maximum transmission angle in Si remains the same (Fig. 2.1 (a)). Likewise the graded-index AR coatings are still governed by the Snell's law and the transmission angle remains small. In the proposed cells the front surface is textured to vertical nanoscale steps (Fig. 2.1 (b)). This nano-optic texture is designed to alter the mechanism that an incident light

couples into the active layer. Unlike the case of transmission/reflection at a bulk dielectric interface, an incident light can make glancing-angle transmission into a high-index active layer via the vertical dipole oscillators induced on side walls. Transmission efficiency can be made high over a wide range of incident angle. Since the light coupled into the active layer propagates along the glancing angle direction (in-plane direction), the path length in the layer can be made significantly greater than the layer thickness. The directions of optical transmission and electrical transport are orthogonal to each other, and this configuration would allow greater flexibility in designing junction structures such that enhanced light absorption is achieved simultaneously with improved carrier collection, therefore enhanced conversion efficiencies (Fig. 2.1 (c)).
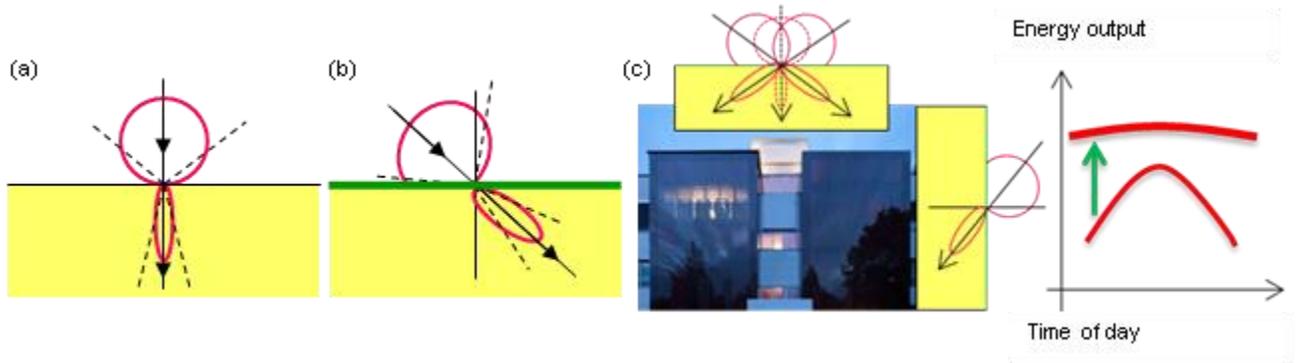
Figure 2.1 (a) Refractive transmission at conventional dielectric interface: the maximum transmission angle is limited small, e.g., ~15° for air-to-Si. (b) Glancing angle transmission through a proposed vertical-dipole, nano-optic texture (green). Note the range of incidence angle for high-throughput transmission is now shifted to oblique direction. (c) The solar panels based on the proposed nano-optic-textured cells will be suitable for mounting in a 3D configuration, and can generate more constant output for an extended period of time of a day.

2.2   GLANCING TRANSMISSION THROUGH A NANOAPERTURE

Introducing a grating structure on the dielectric surface, such as metal wires or grids placed in periodic arrangement, can induce diffractive transmission, and depending on the ratio of grating period to wavelength some diffraction beam can attain glancing angle transmission [23].

In conventional gratings, however, the transmitted power is mostly carried by the zero-order diffraction, whose maximum angle of transmission is limited small for an interface of high index-contrast media, and other higher-order diffraction is usually of minor intensity. The difficulty in achieving high-throughput glancing-angle transmission stems from two reasons: the scattering patterns of arbitrarily-designed diffractive elements in conventional grating structures do not contribute much power to the glancing angle direction, therefore higher-order-diffraction beams of significant intensity cannot build up in that desired direction; the diffractive elements' coverage of dielectric surface and their light coupling efficiency are usually low in conventional grating structures, therefore most incident power transmits through the dielectric surface without interacting with grating elements.

Imagine a hypothetical nanoaperture structure formed in an optically-thick (opaque) film, whose radiation pattern is designed to be highly anisotropic, orienting to glancing angle direction (Fig. 2.2a). Since the dielectric surface is masked except for the nanoapertured region, transmission of an incident light is only through that aperture. Therefore the transmission characteristic is now exclusively governed by the aperture radiation pattern itself, which is oriented to oblique direction. Now consider an array of such hypothetical nanoaperture formed on a dielectric surface (Fig. 2.2b). Interference among the aperture radiations can result in diffraction beams of different orders. The diffraction beam of particular order whose direction is within the angular range of aperture radiation pattern can make strong transmission, while other beams orienting to the direction outside the

radiation pattern cannot develop into a propagating wave. Fig. 2.2c illustrates the phase matching condition (wave vector relationship) for the case of a dielectric surface covered with a hypothetical nanoaperture array. In this diagram, the $+1^{st}$ order diffraction beam on the transmission side is designed to match the nanoaperture radiation pattern, that is, to orient to the glancing angle direction for oblique incidence, and the zero-order and other higher-order diffractions are suppressed. We should note here that the glancing angle transmission in high-index media is enabled by employing highly-directional nanoaperture radiation patterns and their interference effect, and the operating principle differs from those of conventional refraction at bulk dielectric interface.
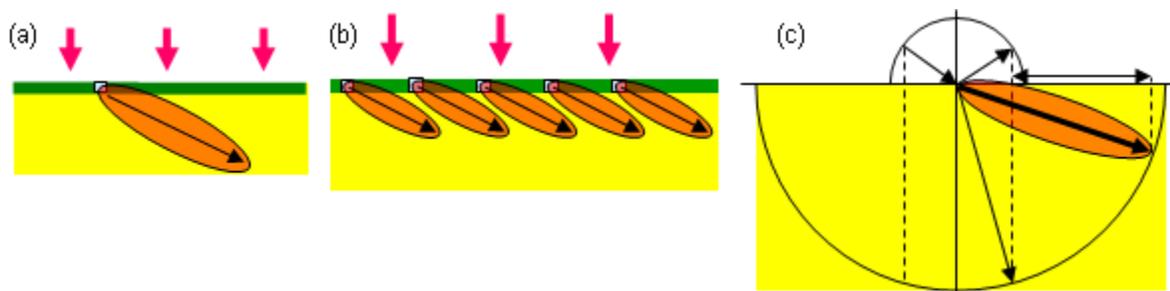
Figure 2.2 (a) Highly-directed radiation pattern of a vertical dipole nanoaperture. (b) Radiation from an array of nanoaperture. (c) Phase matching condition for glancing angle transmission through a nanoaperture array.

2.3 RADIATION PATTERNS OF VERTICAL DIPOLE IN THE AIR SIDE

Consider a nanoscale vertical dipole placed on or underneath a dielectric surface. The vertical dipole can be implemented by forming a narrow stripe or trench structure (two-dimensional) or a post or pore structure (one-dimensional) of high aspect ratio. Under illumination the vertical dipole responds by reradiating the incident light into a characteristic radiation pattern.

The radiation pattern of a vertical dipole placed on a dielectric surface is composed of two contributions, one from the direct propagation to an observation point in far field and another from the reflection at the interface [24].

Fig. 2.3 (a) shows the radiation patterns in the air side calculated for three different media, SiN, Si and Ag at 633nm wavelength. Here a 2D vertical dipole is assumed with dipole length (height) of 75nm. All three cases demonstrate a tilt radiation (30-40 deg from the horizontal direction). This oblique radiation pattern is experimentally confirmed by forming a vertical dipole nanoaperture on metal (Ag) surface. The sample was prepared by angle deposition of a Cr film on a quartz substrate, whose surface was focused-ion-beam (FIB) etched to an asymmetric saw-tooth profile with one side vertically step-etched (step height of ~200 nm) and the other side taper-etched over a tilt span of 760 nm. A vertically aligned nanoslit structure (~100-nm slit width) was fabricated on a quartz substrate by performing focused-ion-beam (FIB) etching followed by angle deposition of Ag film (100-nm thickness) (Fig. 2.3 (b)). The sample was illuminated at the bottom side by a 633nm-laser beam, and the radiation pattern through the vertical nanoslit was measured by scanning a near-field scanning optical microscope (NSOM) probe in the near to far field region [25, 26, 72]. The sensitivity of a nanoapertured NSOM probe varies depending on beam incident angle, that is, showing lower sensitivity for larger incidence

angle. In this work, scanning was performed with the probe axis tilt-oriented to the peak radiation direction (Fig. 2.3b) for maximum signal strength. The NSOM-scan result reveals ~45° tilt of the main lobe, well matching the model calculation. Finite-difference-time-domain (FDTD) analysis of nanoslit transmission was also performed for both vertical and horizontal dipole cases (Fig. 2.4) [73]. For a planar wave normally incident from the bottom side, the nanoslit transmission shows a radiation pattern tilt-oriented from the substrate normal (Fig. 2.4a-d). For the case of a vertical slit formed in a Ag film, for example, the main lobe is oriented to $\varphi = -50^o$ tilt direction from the substrate normal with a full-width-at-half-maximum (FWHM) angle of 50°. This is a striking contrast to the radiation pattern of a conventional slit whose dipole axis is horizontal, parallel to the film surface (Fig. 2.4e,f). The latter structure shows a nearly uniform distribution of power for radiation angle φ of -70° to +70°. The nanoslit aperture formed in a metal film serves as a dipole-like radiation source under illumination. Being placed on a horizontal metal surface the vertical dipole's radiation pattern is comprised of the direct propagation and reflection components. The FDTD simulation of a vertical nanoslit confirms a tilt radiation pattern (~40 deg from the horizontal direction), distinctly different from the horizontal dipole's Lambertian-like pattern.

The amount of dipole charges induced on slit corners and edges depends on the aperture geometry/dimension and the orientation of incident field vectors with respect to the edges. An electromagnetic wave interacting with slit edges can induce polarization surface charges, whose surface density can be expressed as [27]:

$$\sigma_{pol} = \varepsilon_0 (\mathbf{E}_2 - \mathbf{E}_1) \cdot \mathbf{n}_{21} = \varepsilon_0 \left(1 - \frac{\varepsilon_2}{\varepsilon_1} \right) \mathbf{E}_2 \cdot \mathbf{n}_{21}.$$

Here E_1 and E_2 are the electric field in the medium 1 (ε_1) and medium 2 (ε_2) side of the interface, respectively, and n_{21} is the normal vector to the surface. ε_0 is the dielectric permittivity of free space.

In the case of an air-gap ($\varepsilon_2 = 1$) nanoslit formed in a metal film ($\varepsilon_1 = \varepsilon_M$), $\varepsilon_2/\varepsilon_1 = 1/\varepsilon_M$. Mostly $\left|\varepsilon_M\right| \gg 1$, therefore, the amount of dipole charges induced on the surface is determined by the normal component of electric field in air gap. In the case of an air-gap nanoslit formed in a dielectric film (e.g., silicon, $\varepsilon_1 = 12$), the index contrast is also high, and the dipole charge density at the interface can be expressed by the same formula.
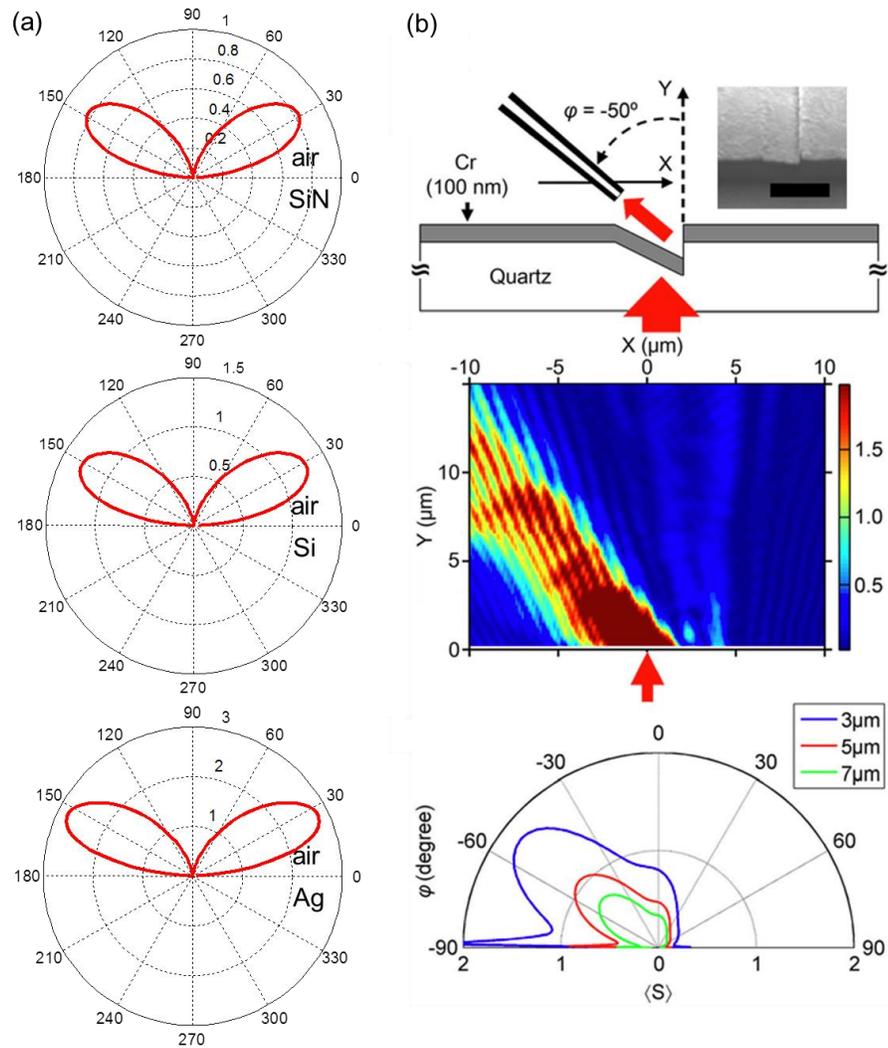
Figure 2.3 (a) Radiation patterns in the air side calculated for three different media, SiN, Si and Ag at 633nm wavelength. (b) Scanning probe measurement of radiation pattern of a vertical nanoslit formed in Cr film (top), radiation pattern measured at 633 nm wavelength (middle), FDTD simulation of radiation patterns at three different radial distances from the aperture center.
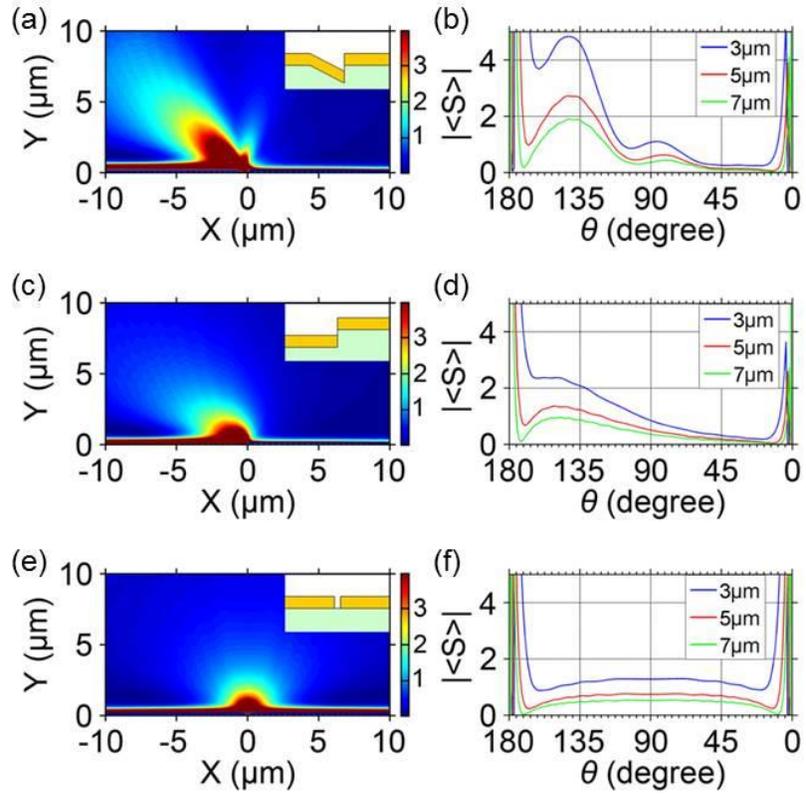
Figure 2.4 FDTD calculation of optical transmission through vertical nanoslit structures. Radiation

patterns of Ag nanoslits (gap size: 60 nm). (a)-(d) Vertical nanoslit structures (inset: cross-section).

The main lobes are tilt-oriented to 50-60$^{\text{o}}$ direction. (e),(f) Conventional horizontal nanoslit.

The transmission throughput of a vertical nanoslit was also calculated for different incident angles (Fig. 2.5) [73]. While the radiation pattern remains tilt-oriented at the same angle ($\varphi = -50^o$) for varying incident angles, the throughput changes significantly. The transmission efficiency, defined as the total transmitted power divided by the incident power that falls on the slit cross-section, reaches 80 % level at $\theta = +45^o$ incidence or normal incidence angle, and 350 % at $\theta = -45^o$ incidence. Here the transmission efficiency's being greater than 100 % indicates a funneling effect, that is, the nanoslit efficiently captures incident power and transmits more than the amount of power that falls on the aperture area (Fig. 2.5). For the case of a horizontal slit with same metal thickness and slit width, the transmission efficiency reaches maximum 53 % at normal incidence.

This implies that a vertical nanoslit structure can outperform a horizontal nanoslit in transmitting incident power. For thicker films, this performance contrast becomes even stronger, and this trend can be understood in view of the fact that in horizontal nanoslits a significant degree of transmission loss occurs in the narrow channel region whereas in the vertical slit case there is no such waveguide constriction and therefore no attenuation. The high-throughput transmission and highly-directed radiation pattern of a vertical nanoslit structure offers interesting potential for overcoming the limits of conventional refractive optics.
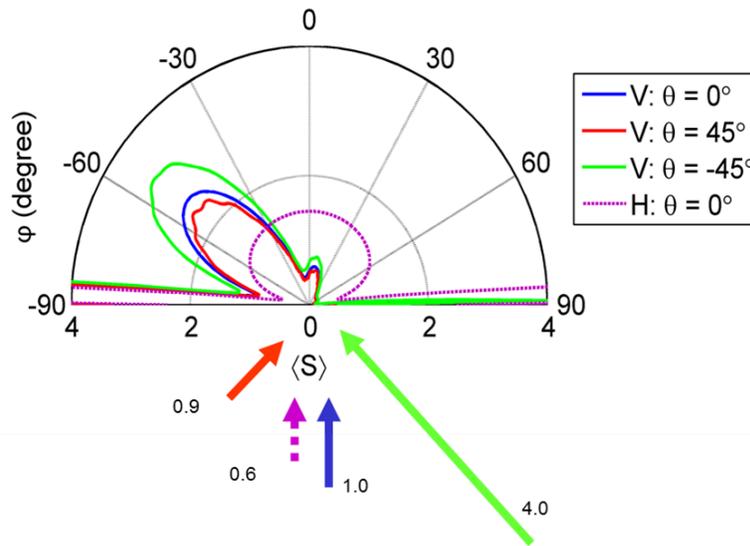
Figure 2.5 Radiation patterns of a vertical nanoslit calculated at three different incident angles. The transmission throughput ratio is marked by the arrow length.

2.4   RADIATION PATTERNS OF VERTICAL DIPOLE IN THE DIELECTRIC SIDE

Now consider a 2D vertical dipole placed underneath a dielectric surface. Fig. 2.6 shows the radiation pattern in the dielectric side calculated for air/Si at 633nm wavelength. Here the vertical dipole length is assumed to be 75 nm. The main lobe is tilt-oriented to ~50 deg. Note that this angle is significantly larger than the maximum transmission angle (~15 deg) attainable from the refraction at a planar dielectric interface. An incident light, once coupled into a vertical dipole inside the dielectric, is reradiated into the directions far more glancing than the refractive transmission case. Similar to the case of a dipole placed in the air side, the radiation of a dipole in the Si side is a superposition of the direct propagation and the reflection components. A main difference in the latter configuration is that the reflection in the Si side becomes a total internal reflection for oblique incidence. The spectral dependence of glancing coupling is governed by the phase difference between the direct transmission and reflection components. For a given dipole length (height) the tilt radiation becomes stronger for shorter wavelengths. Alternatively, for a given wavelength the longer the vertical dipole, the stronger the glancing radiation becomes. In either case, the tilt angle remains in the same range, indicating the robustness of glancing coupling through a short dipole. For a given dipole structure (as specified by dimensions, aspect ratio and index contrast) the excitation efficiency depends on the incident angle relative to dipole axis, and is expressed as a cosine function.

2.5   RADIATION PATTERNS OF VERTICAL DIPOLE EMBEDDED IN THE

PASSIVATION LAYER OF A SI CELL

Next we consider the case that a vertical dipole is embedded in the antireflection/passivation layer of a Si cell. The radiation transmitted into Si is comprised of two contributions: the direct transmission through an evanescence coupling in the near-field region at the interface and the multiple internal reflections of radiative propagation inside the AR layer. Fig. 2.7 shows the radiation pattern in the Si side calculated assuming a 80-nm-thick SiN passivation layer and a 75-nm-high vertical dipole.

Compared to the air/Si case (Fig. 2.6), the tilt radiation is significantly enhanced in both the angular range and its intensity: the lobe at ~60 deg is now stronger and there is another lobe spanning a wide range of glancing angles. This wide-range glancing radiation is due to the direct evanescent coupling of dipole radiation into Si. The enhanced radiation at 60 deg is explained as follows: the dipole radiation propagating inside the SiN layer experiences multiple internal reflections; the top interface (air/SiN) is mostly reflective (i.e., total internal reflecting for glancing incidence), whereas the bottom one (SiN/Si) is transmissive; these asymmetric reflection characteristics at the top/bottom interfaces results in a preferred transmission of dipole radiation to the Si side, not to the air side.
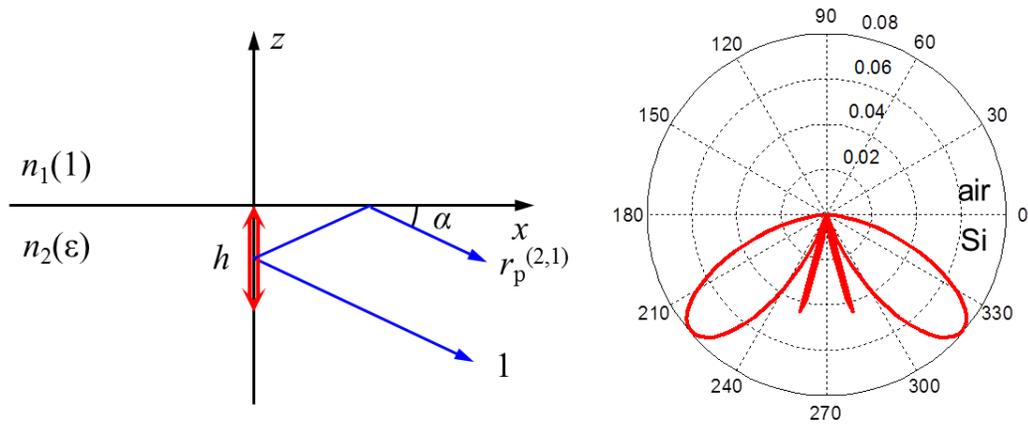
Figure 2.6 Radiation patterns of a vertical dipole placed underneath a dielectric surface.
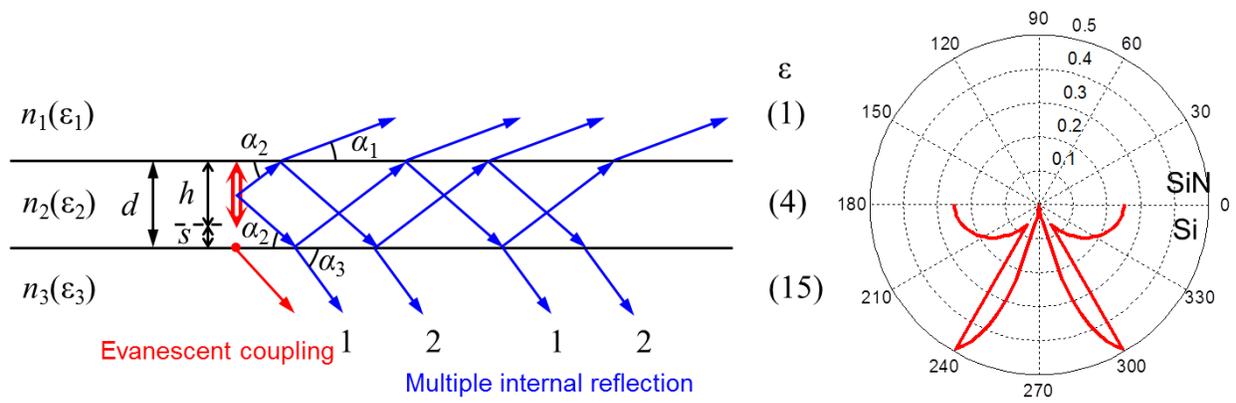
Figure 2.7 Radiation patterns of a vertical dipole embedded in the passivation layer of a Si cell.

2.6   SUMMARY

Surface nano-texturing is designed to provide glancing angle coupling of light into high-index active layer of solar cells. The concept of glancing angle transmission is firstly presented assuming an array of hypothetical nanoaperture formed on a dielectric surface. Then, the radiation patterns of a vertical dipole on or underneath a dielectric surface have been calculated to demonstrate the glancing radiation. A vertical dipole placed in the air side shows $30 - 40$ deg tilt radiation from the horizontal direction. Scanning probe measurement of radiation pattern on a vertical dipole nanoaperture formed on metal surface experimentally confirms a tilt radiation pattern. Tilt-oriented (~50 deg) transmission also occurs for a vertical dipole placed underneath the dielectric. Both the direct propagation in far field and the reflection at the interface contribute for the radiation pattern. Finally, the radiation patterns of a vertical dipole embedded in the passivation layer of Si has been investigated and compared to the air/Si case. The transmission radiation is a superposition of the direct evanescent transmission of dipole at the interface and the multiple internal reflections inside the SiN layer. Interference of the two components results in enhanced tilt radiation in terms of angular range and intensity. We identify that vertical nano-steps formed on dielectric interface can also serve as vertical dipole radiators that relay incident light into glancing direction.

3.0 ONE-DIMENSIONAL VERTICAL NANO-STEPS USING HOLOGRAPHIC LITHOGRAPHY

3.1 INTRODUCTION

3.1.1 Interference of two coherent beams

Holographic lithography, also called interference lithography, is a highly efficient, agile technique for patterning periodic sub-micrometer gratings over large area. In addition, it is mask-free, therefore it can be implemented in a low cost and simple process. Holographic lithography is based on interference of two coherent laser beams, which can create a standing wave pattern recorded in a photoresist.

Consider plane waves of the same frequency ω, produced by two beams reaching the photoresist. The electric fields of the two beams can be written as

$$\vec{E}_1 = \vec{E}_{01} e^{i(\vec{k}_1 \cdot \vec{r}_1 - \omega t + \phi_1)}$$

$$\vec{E}_2 = \vec{E}_{02} e^{i(\vec{k}_2 \cdot \vec{r}_2 - \omega t + \phi_2)}$$

(3.1)

For coherent sources, $\phi_1 - \phi_2$, the phase difference between the two fields is constant.

According to the superposition principle, the net electric field can be described as the vector sum of two sources.

$$\vec{E} = \vec{E}_1 + \vec{E}_2$$

(3.2)

The intensity of radiation field is proportional to the square of the amplitude. Thus,

$$I = \left|\vec{E}\right|^2 = \vec{E} \cdot \vec{E}^* = (\vec{E}_1 + \vec{E}_2) \cdot (\vec{E}_1^* + \vec{E}_2^*)$$

$$= \left|\vec{E}_{01}\right|^2 + \left|\vec{E}_{02}\right|^2 + 2\vec{E}_{01} \cdot \vec{E}_{02} \cos \delta$$

$$= I_1 + I_2 + 2\sqrt{I_1 I_2} \cos \delta \tag{3.3}$$

Where

$$\delta = \vec{k}_1 \cdot \vec{r}_1 - \vec{k}_2 \cdot \vec{r}_2 + \phi_1 - \phi_2 \tag{3.4}$$

For coherent sources, the phase difference δ can be generalized as

$$\delta = k \cdot (r_1 - r_2) + \phi_1 - \phi_2 \tag{3.5}$$

where $k = 2\pi/\lambda$.

Depending on the interference term, $2\sqrt{I_1 I_2} \cos \delta$, the irradiance I is greater or less than I_1 + I_2. For sources having equal amplitude, that is, $I_1 = I_2 = I_o$, we have

$$I = 2I_0(1 + \cos \delta) = 4I_0 \cos^2 \frac{\delta}{2} \tag{3.6}$$

For δ being even multiple of π,

$$\delta = 2m\pi, \qquad m = 0, \pm1, \pm2,\ldots \tag{3.7a}$$

$\cos\delta$ is equal to 1, and constructive interference occurs resulting in maximum irradiance $I_{max} = 4I_0$. In this case, I_{max} (= $4I_0$) is greater than $I_1 + I_2$ (= $2I_0$).

For δ being odd multiple of π,

$$\delta = (2m+1)\pi, \qquad m = 0, \pm1, \pm2,\ldots \tag{3.7b}$$

$\cos\delta$ is equal to -1, and the destructive interference occurs resulting in minimum irradiance $I_{min} = 0$. In this case, I_{min} (= 0) is less than $I_1 + I_2$ (= $2I_0$).

Note that there are two cases having no interference patterns. For two incoherent sources, the phase difference ϕ_1 - ϕ_2 varies randomly with time, leading to zero mean value of cosδ. In this situation, the interference term in the two beam interference formula becomes zero. The other case occurs when two waves are orthogonally polarized. $\vec{E}_{01} \cdot \vec{E}_{02}$ becomes zero thus no interference appears.

3.1.2 Grating period

When two coherent equally polarized plane waves with equal intensity intersect, interference fringes occur in an intersection area. The regions of constructive interference having minimum intensity will not be exposed, while the regions of destructive interference having maximum intensity will be fully exposed. As a result, periodic gratings will be formed on photoresist. Based on the equation (3.7), the grating period d can be calculated by

$$d = \frac{\lambda}{2n\sin\theta} \qquad (3.8)$$

where λ is the free space wavelength of an illuminated light, n is a refractive index of ambient and θ is the half the angle between two beams. In the case of exposer in air ambient, n is equal to 1.

3.2   FABRICATION AND CHARACTERIZATION

3.2.1   1-D gratings by holographic lithography

The optical setup for holographic lithography is shown in Figure 3.1. All optical equipment was placed on an optical table to avoid vibration. During the lithography process, only yellow or red light was allowed because the photoresist is sensitive to shorter wavelength (UV-blue) light.
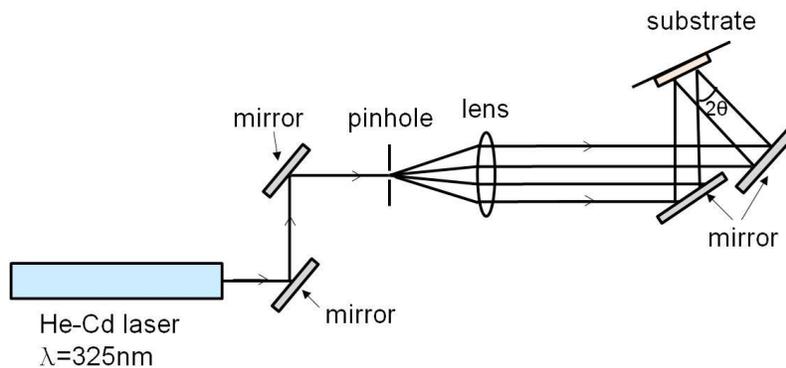
Figure 3.1 Schematic of holographic lithography setup.

P-type silicon substrates were cleaned by acetone, methanol and DI water to remove organic contaminants and dusts from the surface. As an etch mask, a 35-nm-thick chromium film was thermally deposited on the silicon substrates. A 100-nm film of positive photoresist (Shipley 1805) and thinner (Shipley type-P thinner) was then spin-coated on the surface at 5000 rpm for 30 seconds followed by baking at 90℃ for 30 min.

He-Cd laser (5 mW at 325 nm) was used as a coherent light source to make holography patterns. As shown in Figure 3.2, a sample was placed at the center of the area where the two

41

beams intersect. The grating period can be changed by adjusting the beam crossing angle, referring to equation (3.8): the smaller the angle, the larger the grating period. We fabricated patterns starting from 720 nm grating period, and then decreased to 492 nm and 365 nm. The minimum grating period in holographic lithography is theoretically $\lambda/2$ for beam crossing angle (2θ) of 180 degrees; however, it is increasingly difficult for large angles. In practice, grating periods smaller than 300 nm is unattainable because of the large angle requirement. To overcome this problem, we introduced a prism and index matching fluid [28] which could increase the refractive index (n), and therefore decrease the grating period based on the equation (3.8). By using an appropriate angle ($90°$) prism and index matching fluid having 1.5 of refractive index, we could reduce the grating period to 270-280 nm range. The detailed calculation of grating period including scheme is shown in Figure 3.2. The exposure time was usually in the range of 25 s to 35 s. Xylene was used as an index matching fluid between a prism and photoresist since it does not react with photoresist.
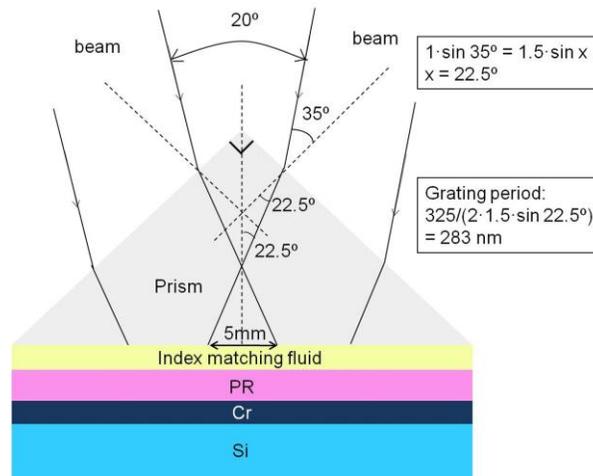
Figure 3.2 Schematic of exposure through a prism.

The photoresist was developed in a developing solution (one part of Shipley 351 developer diluted with four parts of DI water) for 20 – 25 sec. The samples were baked at 110℃ for 30 min to harden the photoresist and improve adhesion between silicon and photoresist.

The photoresist grating pattern was transferred to silicon substrate using a reactive ion etching (RIE) process. We used Unaxis ICP-RIE 790 system to etch chromium and silicon. Chromium etching in Cl_2+O_2 gas ambient (7 nm/min) was followed by silicon etching in SF_6+O_2 gas ambient (16 nm/min). Chromium film played the role of a masking layer in silicon etching. The etching depth of Si was 130 – 150 nm. After etching of silicon, residual chromium on silicon was removed by chemical etching in the solution of NaOH (1g) and $K_3Fe(CN)_6$ (3g) and DI water (11ml). Figure 3.3 shows the schematic of process steps and Figure 3.4 shows scanning electron microscope (SEM) images of grating structures fabricated with different periods (720 nm, 500 nm, and 270 nm).
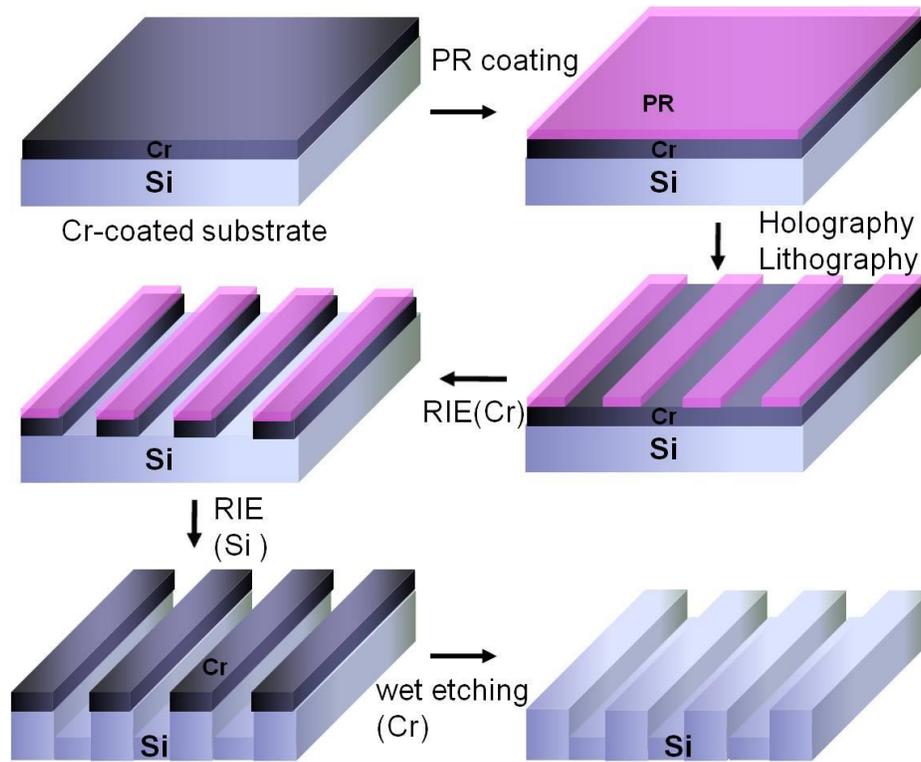
Figure 3.3 Schematic of fabricating gratings using holographic lithography.
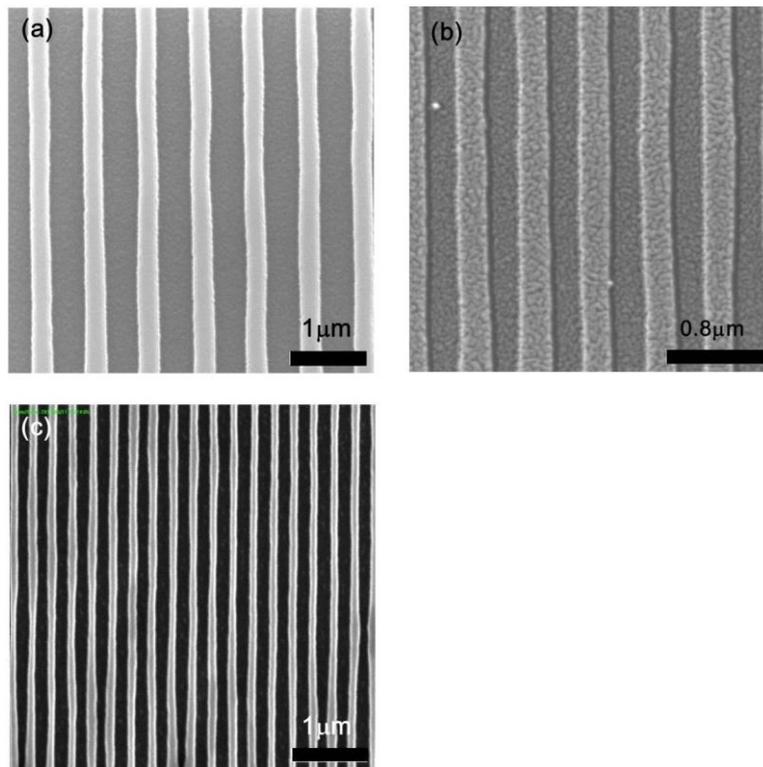
Figure 3.4 SEM images of gratings with (a) 720, (b) 500 and (c) 270 nm period.

3.2.2 Solar cell fabrication

1) Substrate

i) prototype Si pn-junction (p-epitaxial) wafer

In order to test the beneficial effects of vertical mesa grating on solar cell performance, silicon pn-junction cells were fabricated. A n-type (100)-Si (0.005 Ω-cm or 10^{18} cm^{-3}) wafer having a 3-µm-thick p-type epilayer (1.5 Ω-cm or 10^{16} cm^{-3}) was used as a solar cell substrate. Here the 3-µm epilayer serves as the main layer for light absorption, therefore this epitaxial pn-junction cell corresponds to a thin-film Si cell, rather than a bulk Si cell in terms of active layer thickness.

For low contact resistance, a p^+-doped thin layer was prepared on the p-epilayer by performing p-type (boron) diffusion. The p-type dopant (boron from BoronPlus GS-126, TECHNEGLAS) was diffused at 850℃ for 45 min, which is expected to produce approximately 250-nm junction depth. After diffusion, a boronglass layer formed on the surface was removed by chemical etching in a solution of DI water and HF (10:1) for 1 min.

ii) Si n^+pp^+-junction (diffusion) wafer

The prototype Si pn-junction wafer is not an optimum structure because of poor Ohmic contact and shallow active layer (3 µm). Therefore, we have introduced a diffusion process for an n^+pp^+ structure to improve cell performance.

2) Oxidation

Bare silicon surface is known to provide channels (interface and defect states) for various surface recombination losses of photo-generated carriers, which degrades solar cell performance.

46

A 50-nm-thick oxide layer was grown for passivation of the front surface by performing dry oxidation at 1000 ℃.

3) Metallization

After oxidation, the top electrode (20-μm finger width and 180-μm finger spacing) was prepared on the front surface by photolithography, chemical etching and lift-off deposition of Al. The metal coverage on the cell surface was 10 %. The bottom side SiO_2 was also removed by BHF, and then Al was deposited on the etched silicon surface. Finally, Ohmic contact annealing was performed in forming gas ($N_2/H_2 = 90\%/10\%$) at 420 ℃ for 30 min.
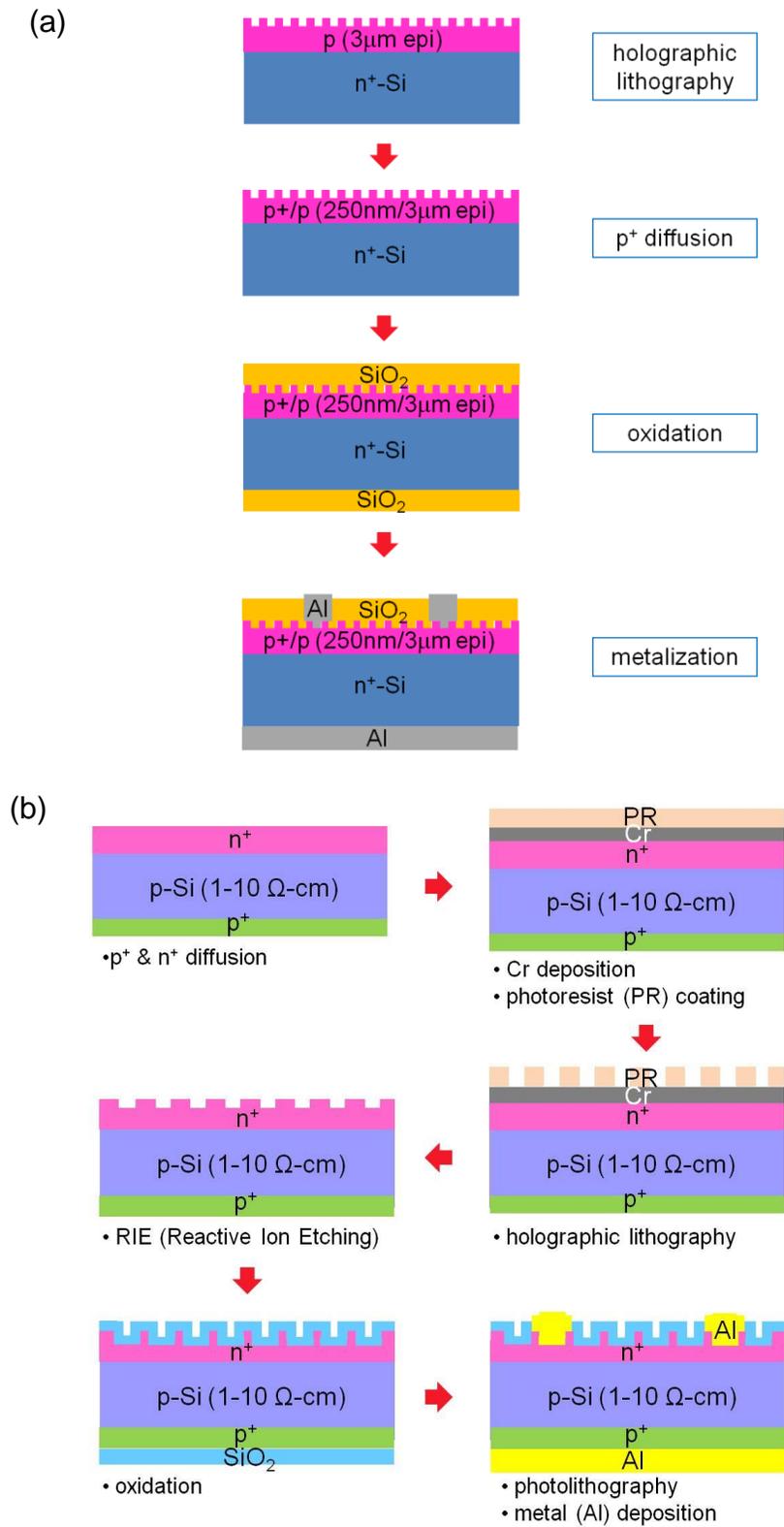
Figure 3.5 Schematic of fabrication process for (a) a Si pn-junction (p-epitaxial) solar cell (b) a Si n^+pp^+-junction (diffusion) solar cell.

3.3   OPTICAL CHARACTERIZATION

3.3.1   Introduction

Snell's law

When light propagates from one medium (refractive index, n_1) to another one (n_2), it produces reflection and (refractive) transmission waves (Figure 3.6). From the phase matching condition of the three wave components at the interface (at $x = 0$), we obtain

$$n_1 \sin \theta_i = n_1 \sin \theta_r = n_2 \sin \theta_t \tag{3.9}$$

where θ_i, θ_r and θ_t are the incident, reflection, and transmission angles. This equation dictates the relationships between the incident and reflection angles (the law of reflection) and the incident and transmission angles (Snell's law of refraction), which is,

$$\frac{\sin \theta_i}{\sin \theta_t} = \frac{n_2}{n_1} \tag{3.10}$$

Fresnel equations

1) Reflection and transmission of *s*-wave (TE wave)

The *s*-wave, also called transverse-electric (TE)-polarized wave, corresponds to the case that the electric field vector of the wave is perpendicular to the plane of incidence. In other words, there is no electric field in the direction of propagation. The reflection and transmission coefficients can be calculated by applying the field boundary conditions, specifically the continuity of E and H field, at the interface. Referring to Figure 3.6, we obtain,

$$r_s = \frac{n_1 \cos \theta_i - n_2 \cos \theta_t}{n_1 \cos \theta_i + n_2 \cos \theta_t} \tag{3.11}$$

$$t_s = \frac{2n_1 \cos \theta_i}{n_1 \cos \theta_i + n_2 \cos \theta_t} \tag{3.12}$$

where we assume the same permeability of the two media ($\mu_1 = \mu_2$).

2) Reflection and transmission of p-wave (TM wave)

The p-wave, also called transverse-magnetic (TM)-polarized wave, corresponds to the case that the magnetic field vector of the wave is perpendicular to the plane of incidence. In other words, there is no magnetic field in the direction of propagation. The reflection and transmission coefficients can be calculated in the same way with s wave case,

$$r_p = \frac{n_1 \cos \theta_t - n_2 \cos \theta_i}{n_1 \cos \theta_t + n_2 \cos \theta_i} \tag{3.13}$$

$$t_p = \frac{2n_1 \cos \theta_i}{n_1 \cos \theta_t + n_2 \cos \theta_i} \tag{3.14}$$

where we assume the permeability of two materials are equal ($\mu_1 = \mu_2$).

In the previous sections we discussed that the reflection and transmission of a planar wave at a dielectric interface depend on the beam polarization. Note that the beam polarization is defined as the orientation of *E*-field vector with respect to the plane of incidence. When the dielectric interface has a 1D grating structure on it, the beam incident plane needs to be specified with respect to the grating vector. In general, then, we can consider the following four configurations in terms of polarization and incident plane orientation with respect to the grating vector): TM, TE, TM' and TE' waves.

Here we define normal and prime configurations based on the direction of grating vector and the plane of incidence. In normal configuration, the grating vector (line) is parallel

(perpendicular) to the plane of incidence. In prime configuration, the grating vector (line) is perpendicular (parallel) to the plane of incidence. Four configurations are drawn in Figure 3.7.
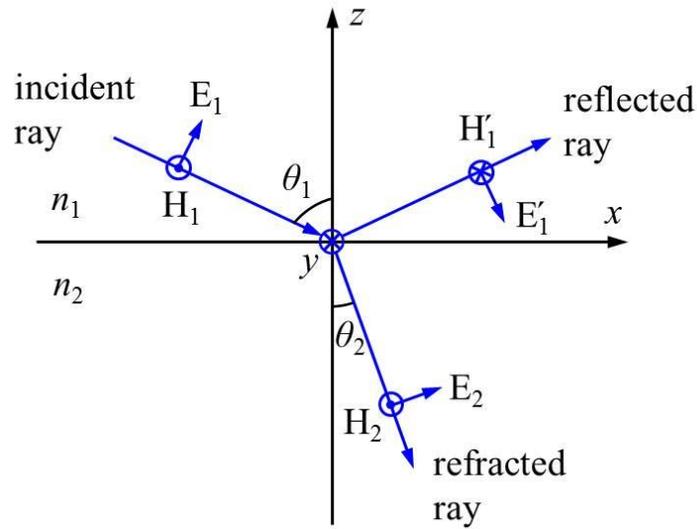
Figure 3.6 Reflection and refraction waves at an interface of two dielectric media.
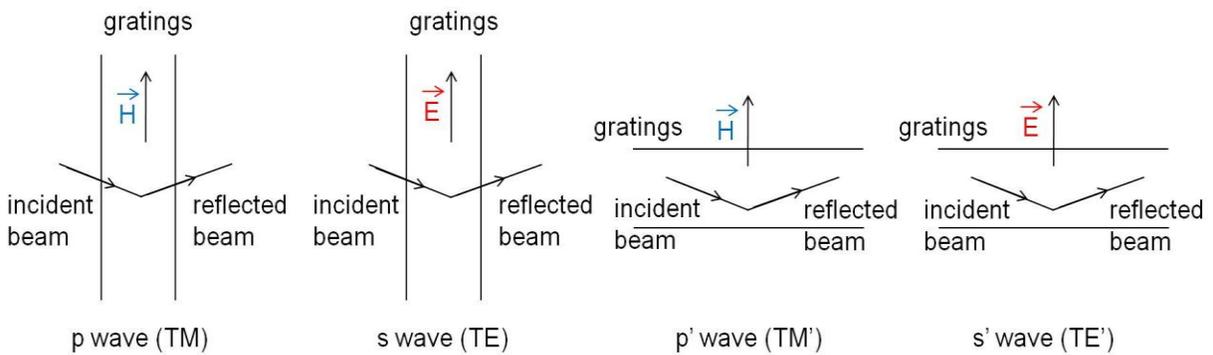
Figure 3.7 Four configurations of our optical measurement.

Now, the vertical dipole concept applied to a 1D grating structure will be explained. It is important to note that dipole oscillators can be induced at dielectric/dielectric interfaces besides the metal/dielectric interface, as discussed in chapter 2.3 with surface polarization charges on slit edges. Consider a mesa-etched grating structure formed on silicon surface (Fig. 3.8). Each mesa comprises one horizontal facet and two vertical sidewalls, and each facet is defined by a pair of parallel edge lines of sub-wavelength scale spacing. Similar to the boundary diffraction phenomenon discussed above with nanoslit edges, each dielectric facet can serve as a dipole radiator with polarization charges induced on the edges. The strength of dipolar response of each facet depends on incident beam direction and polarization, and there are four possible configurations for a 1D grating structure: TM, TE, TM' and TE'. Here the latter two configurations (TM' and TE') correspond to the case that the grating vector is normal to the incident plane, and the other two are for the case that they are parallel.
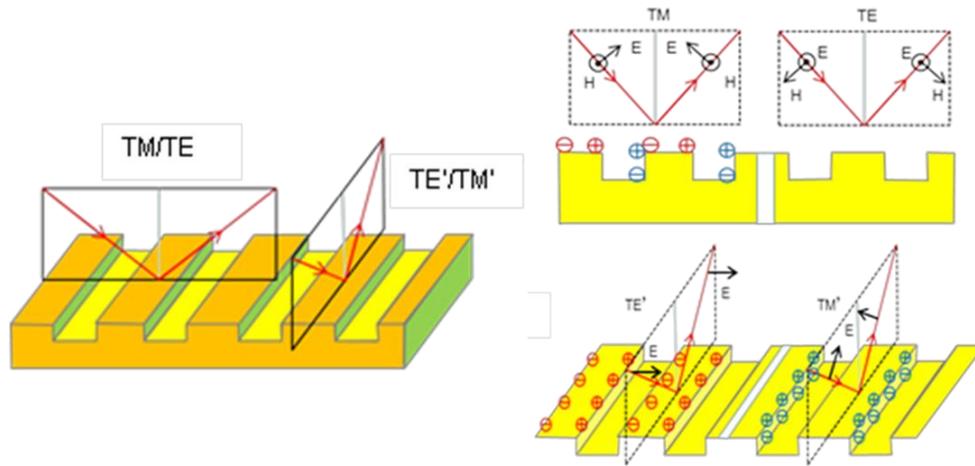
Figure 3.8 Four possible configurations of beam polarization incident to a 1D grating. Reflectance spectra measured at 633 nm wavelength on thin-film Si vertical-mesa array (bottom left) and planar Si surface (bottom middle). Vertical dipoles (blue) and horizontal dipoles (red) are marked on mesa facets (right).

Fig. 3.9 shows FDTD simulation of vertical dipole radiation at a single step of Si for normal incident light (633 nm, TM). At step height of 220 nm, a glancing angle radiation from vertical dipole is clearly observed inside Si, whereas the boundary diffractions [29] also show destructive interference, implying that an incident wave experiences minimal/negligible reflection at step edges. The peak intensity of the dipole radiation component in Si is almost two times stronger than the planar transmission component. For tilt incidence the vertical dipole radiation is expected to grow even stronger as the phase difference of excitations at the top and bottom edges decreases.
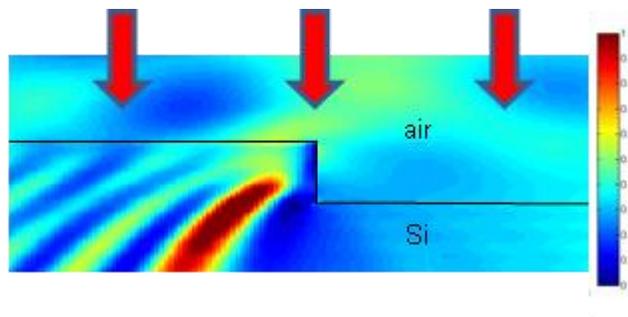
Figure 3.9 FDTD simulation of light transmission through a single vertical nano-step surface of Si: step height, 220 nm; normal incidence of 633 nm, TM polarized light. Glancing angle transmission mediated by vertical dipole excitation is clearly visible.

3.3.2 Measurement set-up

Figure 3.10 shows the optical set-up to measure the incident angle dependence of reflection at a fixed wavelength (633 nm) using a He-Ne laser (~1 mm diameter, power ≈ 8 mW). The incident angle can be varied by rotating the sample holder. Here positive angles refer to the clockwise direction, and negative angles to the counterclockwise direction. A germanium optical detector (LM-2) connected to an optical power meter was used to measure reflected and diffracted beams in far field.
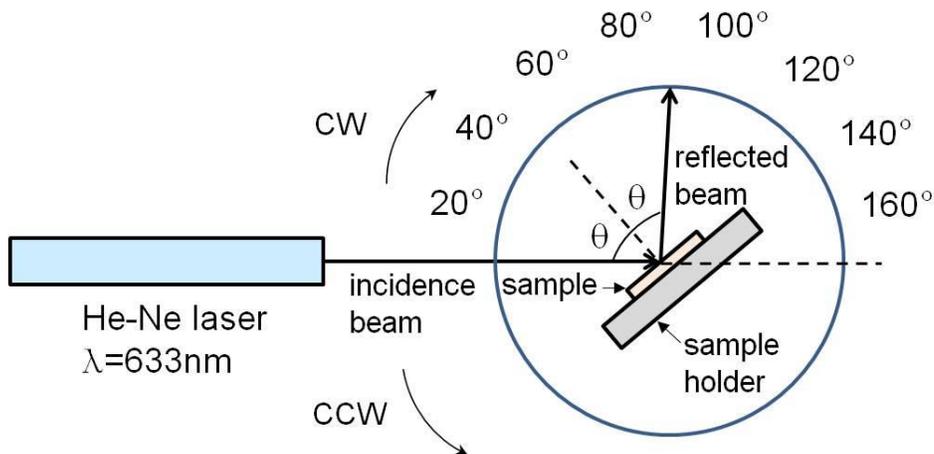
Figure 3.10 Scheme of optical measurement to characterize the angular dependence of reflection.

3.3.3 Results and discussion

planar silicon

1) Angular spectrum of reflection

For a beam incident from air to silicon at a given angle the reflection and transmission coefficients can be obtained from the Fresnel's equations (3.11) to (3.14) [30]. For normal incidence ($\theta_i = 0$), the reflection and transmission coefficients are given by

$$r_s = r_p = \frac{n_1 - n_2}{n_1 + n_2} \tag{3.15}$$

$$t_s = t_p = \frac{2n_1}{n_1 + n_2} \tag{3.16}$$

The reflectance and transmittance are given by

$$R_s = R_p = (\frac{n_1 - n_2}{n_1 + n_2})^2 \tag{3.17}$$

$$T_s = T_p = \frac{4n_1 n_2}{(n_1 + n_2)^2} \tag{3.18}$$

Since our silicon is thick enough (500 μm), we can ignore transmission of light. The refractive index of intrinsic silicon at 300 K with a wavelength of 633 nm is about 3.87 [2]. Therefore, reflection from equation (3.17) is

$$R = (\frac{1 - 3.87}{1 + 3.87})^2 = 0.35 \tag{3.19}$$

This number well matches the experimental result shown in Figure 3.11 (a).

The refractive index of amorphous silicon 633 nm wavelength is about 4.52 [31]. For normal incidence, reflection can be calculated by (3.17)

$$R = (\frac{1-4.52}{1+4.52})^2 = 0.41 \qquad (3.20)$$

This number is slightly different from our measured value, 0.38 (Figure 3.11 (b)), which is from a 1-μm-thick amorphous Si film. The transmission of our silicon film was almost zero.

2) Polarization dependence: Brewster angle

The Fresnel reflection coefficients r_s and r_p depend on incidence angle. The reflectance of s-wave, R_s is always greater than the reflectance of p-wave, R_p. Consider the case that incidence angle is such that,

$$n_2 \cos\theta_i = n_1 \cos\theta_t \qquad (3.21)$$

then, r_p becomes zero from (3.13). This leads to zero reflectance.

Applying the Snell's law (3.11) to (3.21), we obtain this particular angle of incidence:

$$\theta_B = \tan^{-1}\frac{n_2}{n_1} \qquad (3.22)$$

This angle is known as Brewster's angle. At Brewster's angle, the reflectance falls to zero. For crystalline silicon case, the Brewster's angle is calculated as

$$\theta_B = \tan^{-1}\frac{3.87}{1} = 75.5° \qquad (3.23)$$

This number well matches the experimental result shown in Figure 3.11. For amorphous silicon case,

$$\theta_B = \tan^{-1}\frac{4.52}{1} = 77.5° \qquad (3.24)$$

(a)

(b)
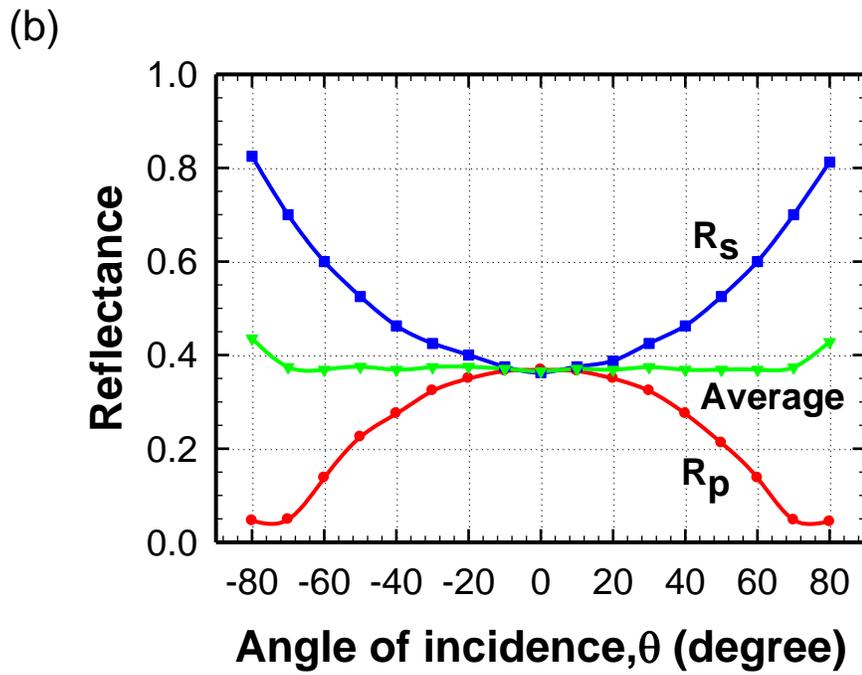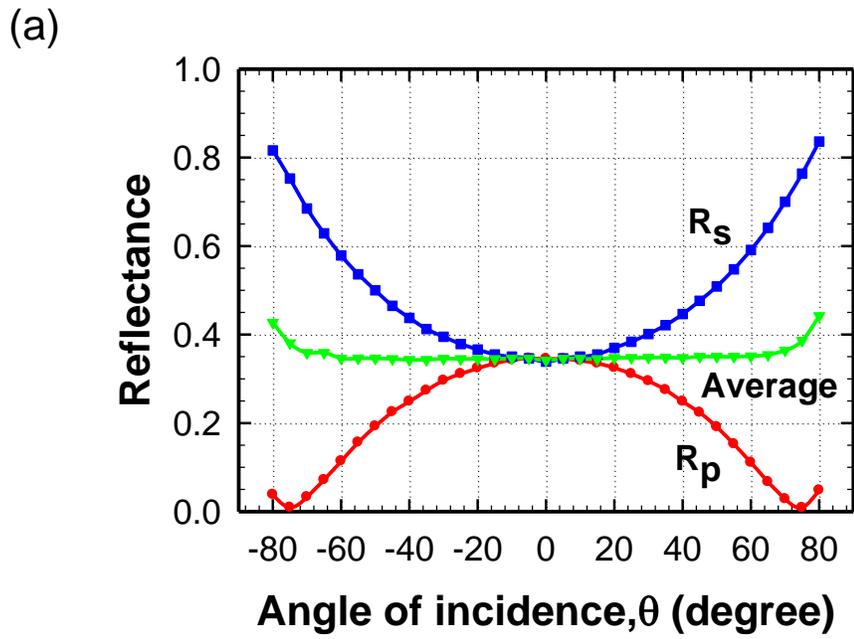
Figure 3.11 Angular-dependent reflectance of (a) crystalline silicon (b) amorphous silicon (1μm) on quartz at 633nm wavelength.

Gratings on silicon

1) Grating effects

When light is incident to a grating structure, the beam can diffract into different directions depending on the grating period relative to the wavelength. Here diffraction is a more generalized concept in that reflection is considered a special case of diffraction (the 0-th order diffraction) that does not involve any interaction with grating vector. Diffraction phenomena at grating surface can be best understood referring to a wave-vector/phase diagram. A phase-matching condition basically states the conservation of momentum of all wave components at the interface. Figure 3.12 shows the phase matching diagram when light propagates from air to silicon.

$$K_{ix} + K_g = K_x^{(m)} \tag{3.25}$$

$$K_{ix} = k_0 \sin\theta, \qquad 0 < \theta < \frac{\pi}{2} \tag{3.26}$$

$$K_g = m\frac{2\pi}{d} = m\frac{\lambda}{d}k_0, \qquad \text{m=0, ±1, ±2 …} \tag{3.27}$$

where $k_0 = 2\pi/\lambda$ (λ is the wavelength of incident beam), θ is an incident angle, d is a grating period and m is the order of grating vector [32].

In introducing a grating structure on solar cell surface, we are interested in eliminating all possible diffraction beams (and also to reduce reflection) in an effort to maximize beam transmission to and absorption inside Si. In developing gratings we started from the grating period of 720 nm because gratings with large period are easier to fabricate than those with small period.

For $\lambda = 633$ nm, $d = 720$ nm and the +1st order ($m = 1$), the light can "see" the grating structures when θ satisfies

$$k_0 \sin \theta + \frac{633}{720} k_0 \le k_0 \tag{3.28}$$

$$\sin \theta \le 0.12 , \ \theta \le 6.89°$$

Thus, the +1st order diffraction will occur when the incident angle is less than 6.89°. From the Figure 3.13, we can confirm that +1st order diffraction beam only exists at -5°, 0°, and 5°.

For $\lambda = 633$ nm, $d = 720$ nm and the -1st order ($m = -1$), backward coupling takes place when θ satisfies

$$k_0 \sin \theta - \frac{633}{720} k_0 \ge -k_0 \tag{3.29}$$

$$\sin \theta \ge -0.12 , \ \theta \ge -6.89°$$

Since the incident angle θ is always greater than 0, this condition applies at all angles, implying that the -1st order diffraction occurs at all angles.

To see the -2nd order diffractions ($m = -2$),

$$k_0 \sin \theta - 2 \cdot \frac{633}{720} k_0 \ge -k_0 \tag{3.30}$$

$$\sin \theta \ge 0.76 , \ \theta \ge 49.5°$$

Therefore, the -2nd order diffraction occur from the incident angle of 50°. For grating period of 720 nm, many high order diffraction beams can exist. Next we gradually reduced the grating period until all high order diffraction beams disappeared.

If the grating period is much smaller than the wavelength of incident light, only m = -1 order backward coupling is possible at certain range of incident angles. For $\lambda = 633$ nm, $d = 500$ nm and the +1st order ($m = 1$), $K_{ix} + K_g$ is always greater than k_0 because $\dfrac{\lambda}{d} = \dfrac{633}{500} \ge 1$ and

$\sin\theta > 0$. Therefore, the +1st order diffraction will not appear at any angle. For the -1st order (m = -1), coupling takes place when

$$k_0 \sin\theta - \frac{633}{500}k_0 \geq -k_0 \qquad (3.31)$$

$$\sin\theta \geq 0.266, \quad \theta \geq 15.4°$$

Therefore, the -1st order diffraction occurs at 20° shown in Figure 3.14.

Similarly, for $\lambda = 633$ nm, $d = 370$ nm and the +1st order ($m = 1$), $K_{ix} + K_g$ is always greater than k_0 because $\dfrac{\lambda}{d} = \dfrac{633}{370} \geq 1$ and $\sin\theta > 0$. Therefore, the +1st order diffractions will not appear at all angles. For the -1st order ($m = -1$), coupling takes place when

$$k_0 \sin\theta - \frac{633}{370}k_0 \geq -k_0 \qquad (3.32)$$

$$\sin\theta \geq 0.71, \quad \theta \geq 45.2°$$

Hence, the -1st order diffraction occurs from the 50° angle (Figure 3.15). Even though we greatly decreased the grating period, diffraction still occurs at over 50 ° angles.

All diffractions completely disappeared for $\lambda = 633$ nm and $d = 270$ nm (Figure 3.16). K_{ix} + K_g is always greater than k_0 because $\dfrac{\lambda}{d} = \dfrac{633}{270} \geq 1$ and $\sin\theta > 0$. K_{ix} - K_g is always less than -k_0 because $k_0 - \dfrac{633}{270}k_0 = -1.34k_0 < -k_0$ when $\sin\theta = 1$ (maximum). Therefore, the light cannot see gratings resulting in no diffractions. By reducing the grating period from 720 nm to 270 nm, we have found the optimum grating structure that demonstrates minimum/suppressed high-order diffractions.

With our structure, gratings having 270 nm periods and 130 nm depths, we can eliminate all diffractions except the zero-order. Besides, the edges of gratings form an array of vertical

dipole giving rise to enhance light coupling through nano-aperture. Vertical dipole nanoslits can send the incident light in glancing angles; therefore more transmission and less reflection are achieved.

From the Figure 3.16, the reflectance of mesa silicon with 270 nm grating period at normal incidence is approximately 13 % which is much less than 35 %, the reflectance of planar silicon at normal incidence.
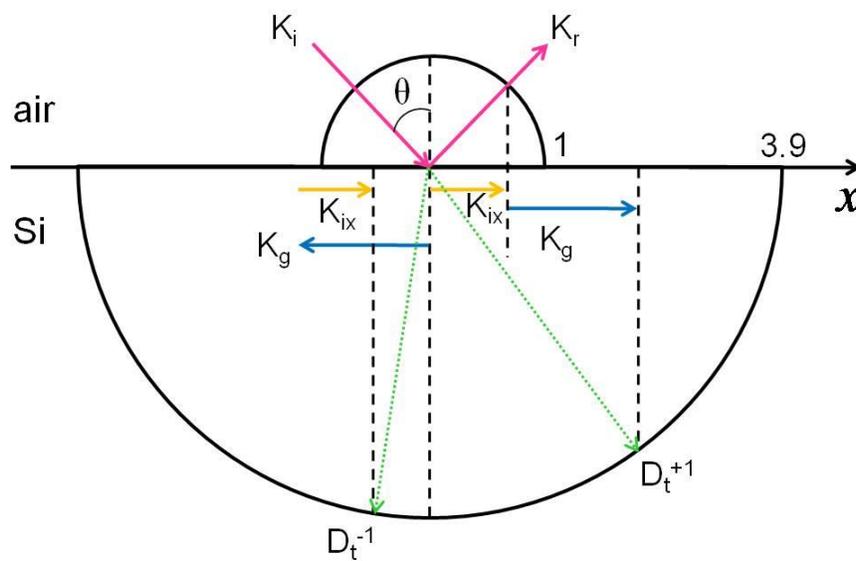
Figure 3.12 Phase matching diagram between air and silicon.
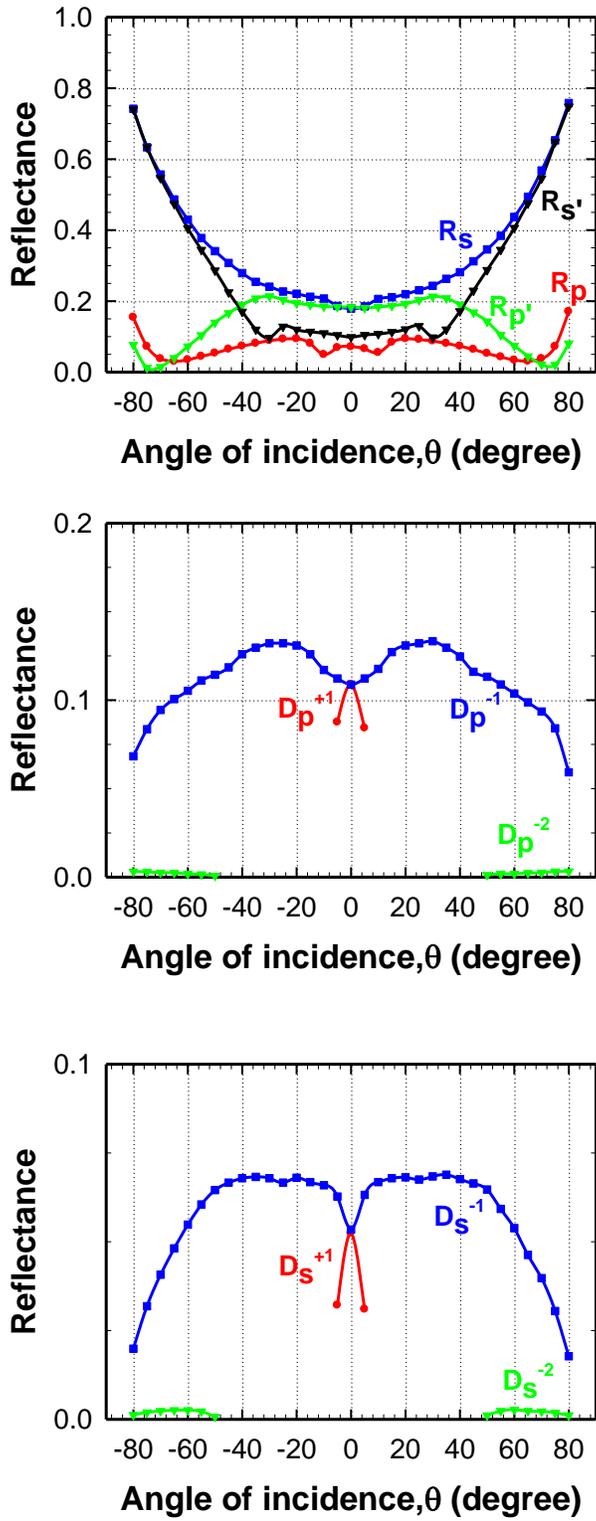
Figure 3.13 Angular dependence of reflectance when the grating period d = 720 nm and λ = 633 nm.
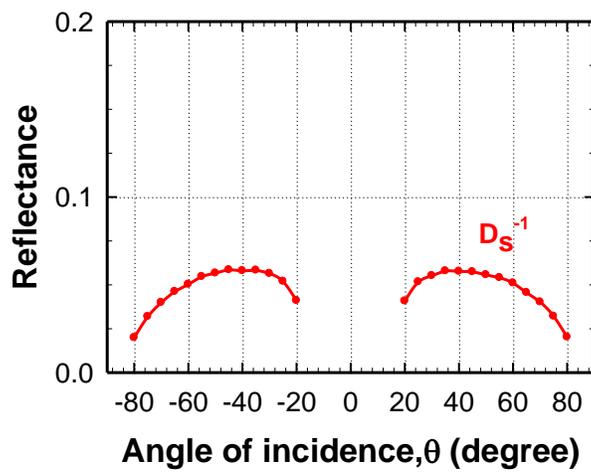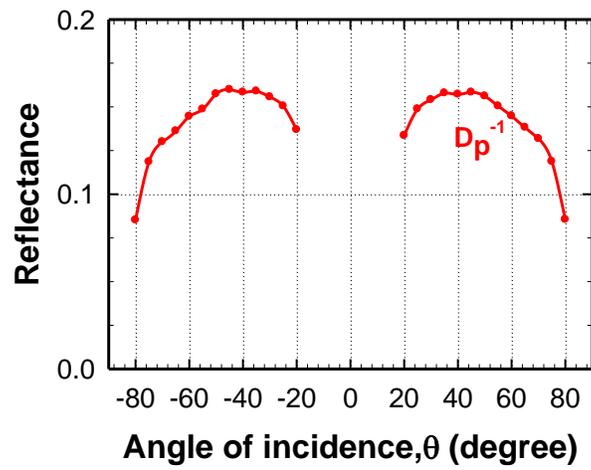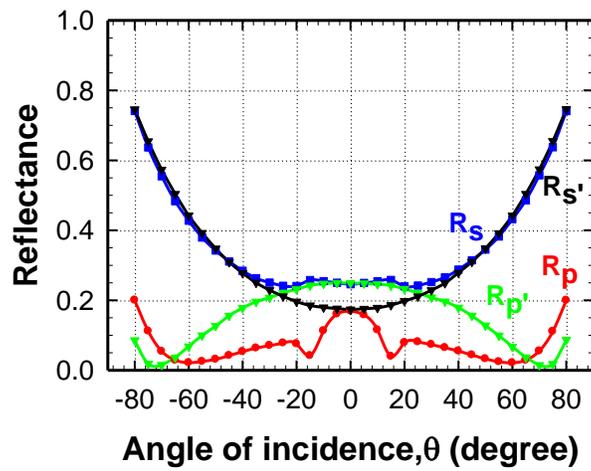
Figure 3.14 Angular dependence of reflectance when the grating period d = 500 nm and λ = 633 nm.
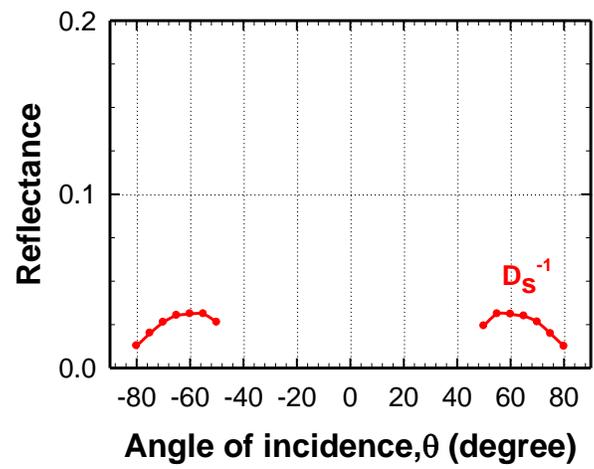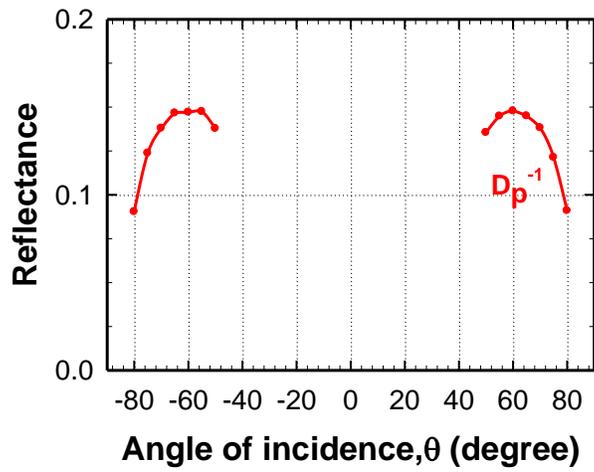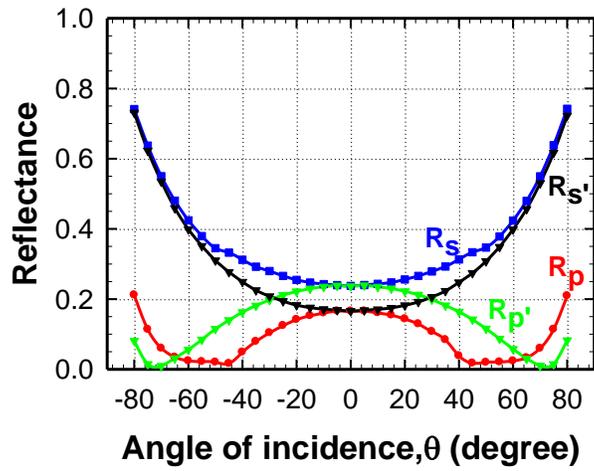
Figure 3.15 Angular dependence of reflectance when the grating period d = 370 nm and
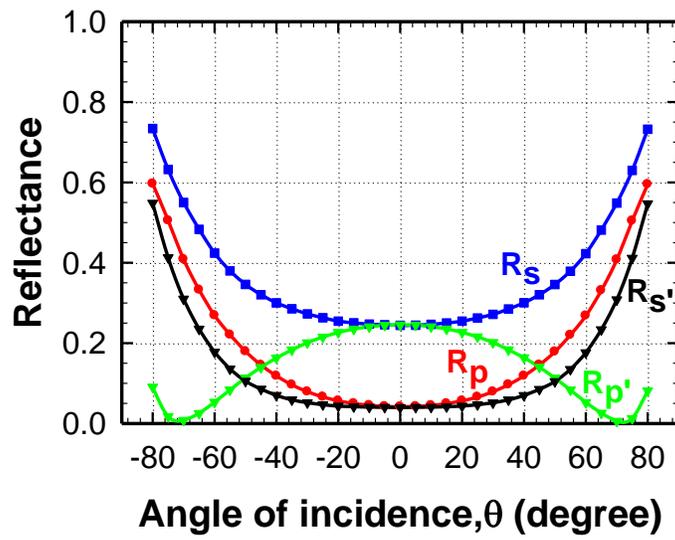
λ = 633 nm.

Figure 3.16 Angular dependence of reflectance when the grating period d = 270 nm and

λ = 633 nm.

2) Oxidation effects

The reflection was dramatically reduced when we introduced a 50-nm-thick oxide layer on top of silicon. An oxide layer is commonly used as a passivation layer in silicon solar cells to reduce surface recombination. The overall reflectance in Figure 3.17 is significantly lower compared to the reflectance in Figure 3.16. At normal incidence, the average reflectance decreased from 13 % to 4 %. This can help improving cell efficiency because the reflectance from the surface becomes now very low.

An interesting feature of prime modes is that the reflectance in those modes is less than that of normal modes over all angles. From -60° to 60°, the reflectance of prime modes is mostly below than 4 %.
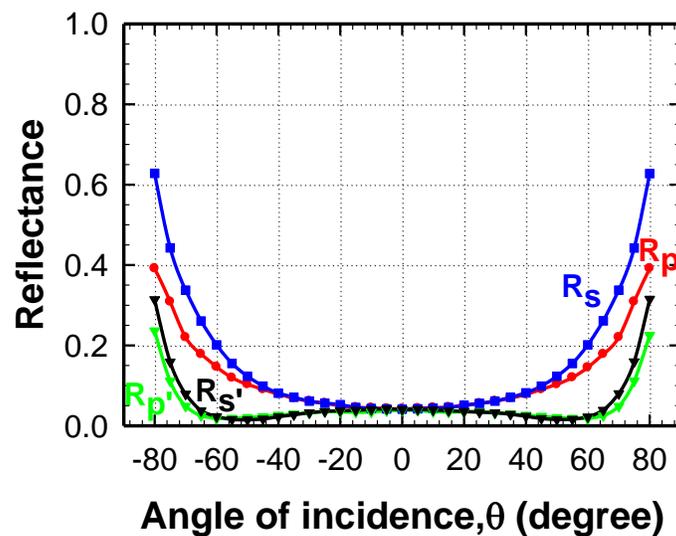
Figure 3.17 Angular dependence of reflectance when the grating period d = 270 nm and $\lambda = 633$ nm with an oxide layer.

66

Fig. 3.17 shows reflection spectra measured at 633 nm wavelength with a mesa array that was formed on a 1-µm-thick silicon film deposited on quartz substrate. The mesa depth is 170 nm. The grating period (270 nm) was chosen significantly smaller than the wavelength of light (633 nm) so that there would be no high-order diffraction (other than the zero-order reflection) in the air side. For comparison, a planar Si surface was also measured for both TM and TE polarizations (Fig. 3.11). Whereas the planar Si shows 35 % reflectance, the mesa-etched surface shows significantly reduced reflectance (3 - 7 %) over a wide range of incident angle. This dramatic reduction of reflection indicates that the incident beam excites dipole oscillations at each facet edges (vertical or horizontal), and they re-radiate the incident power into different directions depending on the orientation of dipole axis.

For TM case, horizontal (or vertical) facets respond most efficiently to normal (or glancing) incident waves. For TM' case, vertical facets respond with dipole oscillations to obliquely incident wave. For TE' case the E-field is always perpendicular to horizontal facet edges, therefore top surfaces can serve as a dipole radiator for any incident angle. For TE case, the E-field is co-linear to any edge lines, therefore no dipolar surfaces are available for any incident angle. Yet the measured reflectance of mesa surface shows a major reduction in a wide range of incident angle. This is mainly due to the phase retardation of reflection at two different levels (mesa top and bottom surfaces), which has the effect of forming destructive interference. The retarded oscillations across vertically displaced levels can also be viewed as quasi-vertical-dipole oscillation. Overall this preliminary result clearly demonstrates that dipole oscillations can be easily excited on dielectric mesa surfaces. Reduced reflection of light at mesa surface implies enhanced coupling into substrate. While the horizontal dipoles would re-radiate incident light

mostly into normal direction, the vertical dipoles at sidewalls would direct it into glancing angle direction.

In maximizing the antireflection effect and glancing angle coupling of light, the following parameters are identified: mesa depth and width, grating period, and dielectric function of mesa/cladding materials. Mesa depth is considered one of the critical parameters that determine the strength of vertical dipoles for a given wavelength and incident angle. Vertical facets are most efficiently excited by obliquely incident TM or TM' waves (Fig. 3.8). For small mesa depths, the dipole polarization will grow proportional to the depth. If too thick, however, the polarization charges will become out of phase, and the dipolar strength will diminish. For TE case, the quasi-vertical-dipole effect occurs across mesa depth for normal incidence, and the maximum polarization condition is expected to be approximately half-wavelength thickness of mesa depth. Mesa width will play a similar role for horizontal dipoles. Horizontal facets are most responsive to TE' and TM normal incidences. The distribution of coupling contributions via vertical and horizontal dipoles will be analyzed as a function of mesa structure and dimensions.

In designing array structures the most critical parameter would be grating period with respect to incident wavelength and angle. With an array of mesas, the vertical dipole radiations from individual sidewalls can constructively interfere forming diffraction beams of higher orders. If the diffraction angle of particular order is designed to be within the radiation pattern, the beam can make a glancing propagation to far fields (Fig. 2.2c). In alternative designs, where the grating period is significantly smaller than the wavelength, there would be no high-order diffraction beams. Recall that the zero-order refraction at a planar interface usually orients to the direction of small transmission angle in the high-index medium. In the case that the zero-order refraction angle is not supported by the vertical dipoles, the radiations mediated by the dipoles

68

would not make far-field propagation, since they would eventually interfere destructively. In that case the dipole radiation will behave similar to evanescent wave propagation. The evanescent tail (dipole radiation) can easily extend to wavelength scale (see Fig. 2.4a&c), and the absorption enhancement effect would be more distinctly observable in thin-film cells. Considering the discrete nature of dipole distribution at interface, the detailed nature of evanescent coupling is expected to be different from the conventional evanescent wave propagation in a total internal reflection (TIR) scheme, and understanding the underlying mechanism is a subject of study in this program.

3.4 ELECTRICAL CHARACTERIZATION

3.4.1 Measurement set-up

A He-Ne laser (633 nm wavelength) was used as an input light source in this work. The beam incident angle was varied from 0 to 80 degrees. All measurements were performed in a completely dark room. By sweeping the voltage from -1V to 1V, dark current and photocurrent were measured. Electrical parameters such as the short-circuit current and the open-circuit voltage were obtained at each incident angle, 0°, 30° and 60°. To measure *I-V* characteristics, the HP 4145B (Semiconductor parameter analyzer) was connected to the probes, which directly contact to the electrodes.
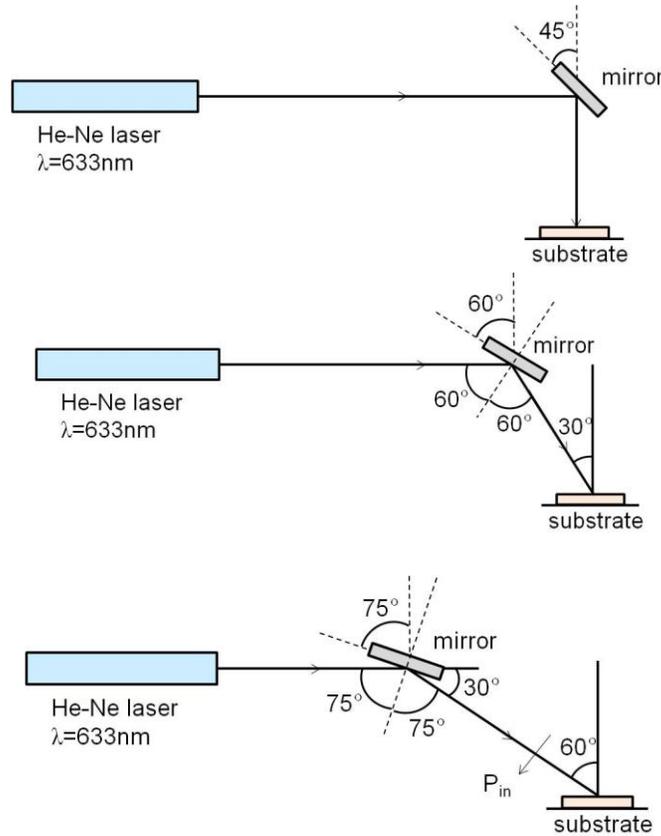
Figure 3.18 Optical set-up for measuring angular dependence of efficiencies.

3.4.2   Results and discussion

Prototype Si pn-junction (p-epitaxial) wafer

The beneficial role of vertical dipoles was further tested by fabricating a Si pn-junction solar cell with nano-textured surface (270-nm grating period, 170-nm mesa depth on Si surface). Fig. 3.19 shows a prototype cell fabricated and tested in this study: Al electrode (20-µm finger width; 200 µm spacing)/p-Si active layer (3 µm thickness; low doped, ~1016 cm-3)/n+-Si substrate. For comparison purpose, samples with planar surface (without mesa structure) were also fabricated as well as the ones with a 50-nm-thick oxide layer on planar or mesa-etched Si surface. Two stages of efficiency improvement were observed. First, incorporating a vertical mesa array on emitter surface increased the cell efficiency (from ~5 % to ~7 %) over a wide range of incident angle. Adding an oxide passivation layer on Si-mesa surface further improved the efficiency to ~8 %. Note this prototype is not optimized yet in its structure: that is, no p+-layer was introduced to make low contact resistance; the high series resistance effect caused by poor Ohmic contact and lateral conduction limits the cell performance; also the active layer (3 µm) is not thick enough to make full absorption of incident photons; therefore the reference sample itself (planar surface without mesas) did not show good efficiency. Despite these deficiencies the beneficial role played by vertical dipoles is clearly revealed when we compare the oxide layer effects: whereas adding a thin oxide layer on planar surface resulted in a marginal improvement of efficiency (0.2-0.4 %), the same oxide layer on mesa surface increased the efficiency by a far greater margin (1.0-1.5 %) over a broad angular range. This corresponds to an overall improvement of ~60 % (from ~5 % to ~8 %), and confirms that vertical dipoles induced

71

on mesa sidewalls allow glancing angle coupling of light, enabling absorption enhancement in an active layer of relatively small thickness.
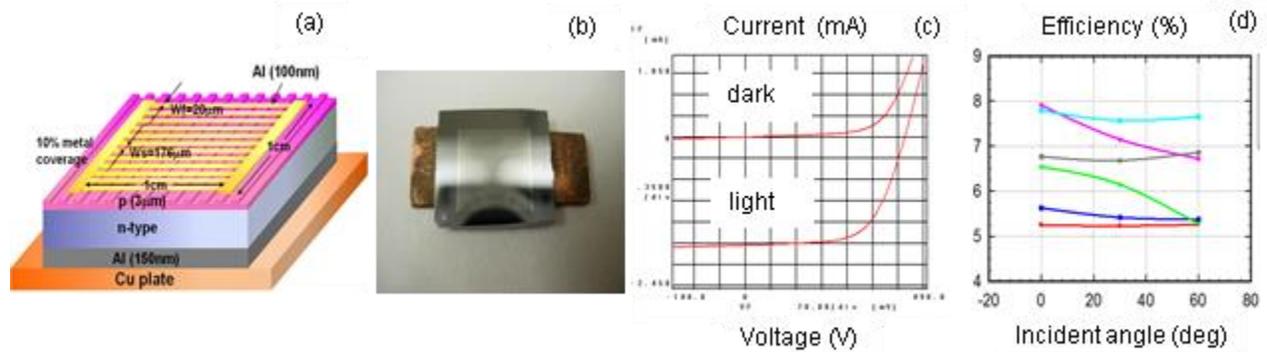
Figure 3.19 (a),(b) A prototype Si pn-junction solar cell fabricated in this study. (c) I-V characteristic at 633 nm wavelength (6.85 mW, TM normal incidence): Isc = 1.85mA; Voc = 0.42V; FF = 0.7; efficiency = 7.95 %. (d) Efficiency vs incident angle: reference cell (planar without oxide) (red); planar with oxide (blue); mesa without oxide (TE/TM) (green); mesa without oxide (TE'/TM') (grey); mesa & oxide (TE/TM) (purple); mesa & oxide (TE'/TM') (light blue).

Si n⁺pp⁺-junction (diffused) wafer

Even though the Si pn-junction (p-type epi-layer) wafer has been used for convenience, it cannot overcome drawbacks such as low contact resistance and shallow active layer. Therefore, p-type Si substrate has been introduced for n^+-diffusion on the front side and p^+-diffusion on the back side to improve cell performance including series resistance. The cell structure and the I-V measurement data is shown in Fig. 3.20. Compared to the efficiency of reference cell (planar with oxide) which was ~ 8 %, the efficiency of mesa-etched Si cell was much higher (15 ~ 16 %) due to mesa effect. It is interesting that the efficiency of 2D mesa Si cell depending on incident angle lies between the efficiency of TE/TM average and the efficiency of TE'/TM' avg. in Fig. 3.19 (c). Eventually 2D mesa is better than 1D mesa in terms of inducing more vertical-dipoles to send light into Si.
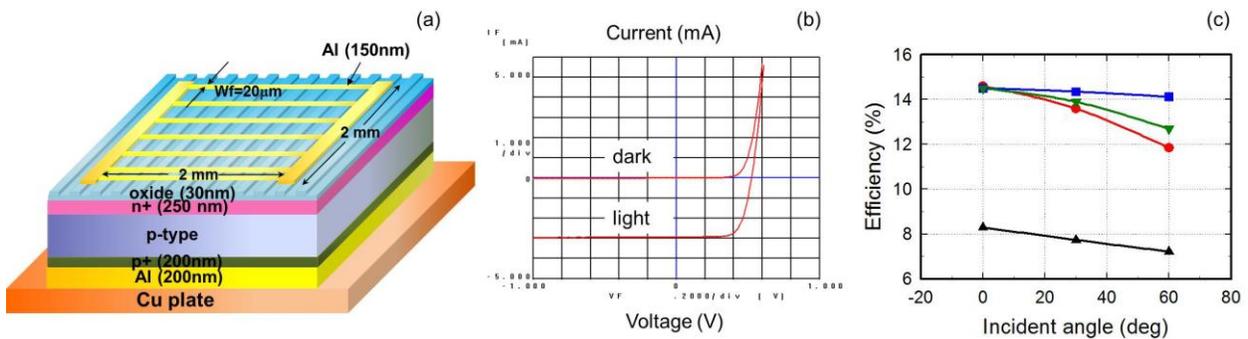
Figure 3.20 (a) A Si n+pp+-junction (diffused) solar cell (b) I-V characteristic at 633 nm wavelength (7 mW, TE normal incidence): Isc = 2.94mA; Voc = 0.53V; FF = 0.71; efficiency = 15.7 %. (c) Efficiency vs incident angle: reference cell (planar with oxide) (black); 1D mesa & oxide (TE/TM avg) (red); 1D mesa & oxide (TE'/TM' avg) (blue); 2D mesa & oxide (green).

3.5   SUMMARY

We have characterized the optical and electrical properties of nano-grating structures formed on Si using holographic lithography. The holographic lithography technique utilizes an interference of two coherent beams that can create grating patterns. The grating period depends on the angle between two beams. Optical characteristics of planar Si and gratings on Si are studied by measuring the angular-dependent reflectance. Starting from the reflectance of 35 % on bare Si, the reflectance has been suppressed by eliminating all diffraction beams in grating structures on Si. The control of diffraction beams is based on the phase matching condition. By reducing the grating period from 720 nm to 270 nm, the reflectance at normal incidence is reduced to 13 %. Besides the elimination of high-order diffractions, an array of vertical dipole formed on the edges of gratings can make glancing coupling of light that contributes reducing reflection and increasing transmission. Grating structures are applied to Si cells to test beneficial role of vertical dipoles. With a He-Ne laser, we have achieved the cell efficiency of 15 % with mesas from the cell efficiency of 8 % without mesas.

4.0 VERTICAL DIPOLE INTRODUCED TO A FINISHED CELL: TWO-DIMENSIONAL NANO-MESAS USING SILVER

4.1 INTRODUCTION

In order to demonstrate the enabling nature of glancing coupling for solar cells, we explored implementing the vertical dipole nano-optic structure on a finished Si cell. Commercial c-Si cells typically employ the following surface structure: a micron-scale pyramid-textured surface coated with a 80-nm-thick SiN antireflection/passivation layer.

Conventional pyramid-textured surface is designed to provide an AR effect by allowing a reflected light a second chance to enter Si. It should be noted that the pyramid texture offers another important benefit: the junction area, where built-in field develops, is significantly increased over the planar case; for the same incident flux the increased junction area enhances carrier transport (separation and collection). In pyramid-textured cells an incident light is highly refracted in Si and propagates in the direction near normal to the junction interface. From the ray-optics point of view, each pyramid serves as a convex lens sharply focusing the incident beam (Fig. 4.l). This lensing effect is equivalent to concentrating a large area of sunlight into a small area, which usually results in significantly reduced carrier lifetimes due to Auger effect [33, 34].

The vertical dipoles introduced to the AR layer on pyramid surface alter the beam propagation inside Si. Glancing coupling of light increases the effective path length along the junction interface. This would result in enhanced light absorption and carrier transport/collection. This benefit will be more prominent in shorter wavelengths, where the absorption depth is smaller than the pyramid dimension, therefore most carriers are generated near/around the junction interface. Note also that the glancing coupling has the effect of reducing/alleviating the focusing effect of pyramid lens (Fig. 4.1). The reduced lensing-effect will benefit the longer wavelength regime, where absorption depth becomes comparable to or longer than pyramid dimension, since the pyramid region is now less prone to Auger effect.
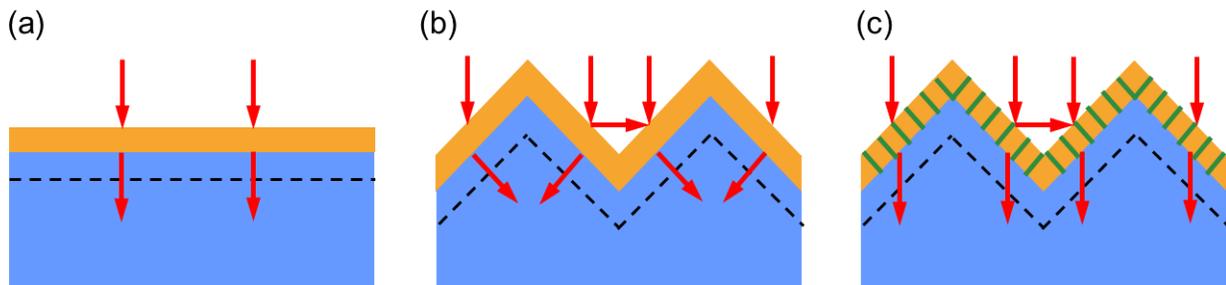
Figure 4.1 Schematic of light propagation on (a) planar surface, (b) pyramid-textured surface, (c) pyramid-textured surface with vertical dipoles.

Now, the efficacy of nanoscale vertical textures in light coupling will be analyzed and compared for both surfaces. Pyramid etching is an anisotropic etching process that preferentially reveals {111} faces, and is commonly employed in texturing of crystalline Si for light trapping via randomization. It is important to note that the pyramid dimensions are typically in micro/macro scale (10-15 µm base width), and a significant level of reflection loss occurs at the macroscale facets. Imagine a ray component that is incident normal to the substrate, that is, at ~45 degree to a pyramid facet (Fig. 4.2b). The reflection component propagates to a neighboring facet and makes a partial transmission into Si. The overall transmittance in this two-step process is estimated to be 0.88 (= 0.65 + 0.35x0.65). In the case of glancing incidence, that is, near-normal incidence to a facet, there is no second chance for entrance, and the overall transmittance is limited to 0.65. The average transmittance is then approximately 0.77. By contrast, the vertical nano-textured pyramid surfaces are expected to show 0.90-0.95 reflectance at single incidence (Fig. 4.2c). Another important benefit with nano-texturing would be that most light is coupled to the direction along the junction interface, as opposed to the near-perpendicular direction in the case of planar interface. Since photo-carrier generation and collection occurs most efficiently near junction interface, the glancing coupling through nano-textures is expected to benefit cell efficiency.

According to the discussion above on polarization charges on dielectric interface, a higher index contrast is desirable for stronger dipole oscillations. Nano-vertical steps will be formed on a SiO_2/Si interface or in a SiO_2 layer in close proximity to Si surface. Oxide passivation of Si surface is commonly required to alleviate surface recombination losses. Compared to bare silicon surface in air, the index contrast of Si/SiO_2 is lower (12/3.9 versus 12/1), but reasonably large enough to induce strong polarizations. Methods to further enhance

index contrast, therefore dipole strength, will also be investigated by introducing a thin (~10nm), non-absorbing (transparent) layer of relatively high-index material (e.g., SiN, TiO_2, ZnO, a-Si) on mesa surfaces.
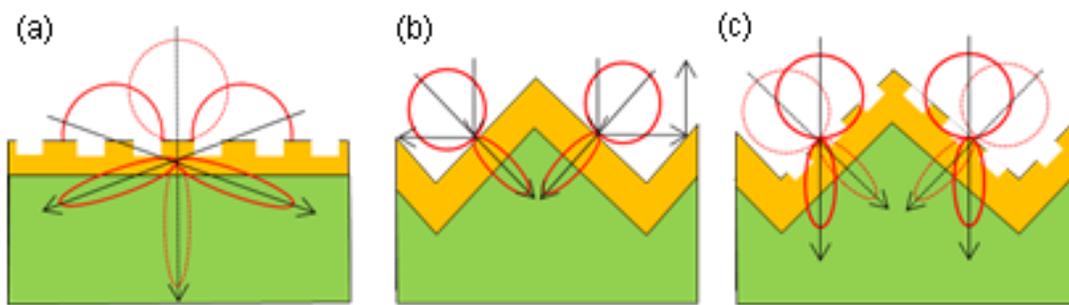
Figure 4.2 Coupling of light into Si: (a) planar surface with nano-vertical steps; (b) pyramid-etched surface; (c) pyramid surface textured with nano-vertical steps. Note nano-vertical dipoles enable glancing coupling of light.

4.2   FABRICATION PROCESS

4.2.1   Nano-vertical steps using self-organized metal nanoislands

For larger area (wafer scale or beyond) patterning with nano-vertical steps, a self-organization-based non-lithographic method will be explored. It is well known in literature that a thin layer of metal (e.g., Ag, Al or Au) deposited on silica surface can ball up forming nanoislands/disks upon receiving a heat treatment at intermediate temperature (200-300 ^{o}C) [35]. Figure 4.3a shows Ag nanodisks formed on silica surface (prepared in this study; sputter deposition of 10-nm Ag at room temperature, followed by annealing at 300-400 ^{o}C). Average particle size of ~40 nm and spacing of ~100 nm is observed. The self-organized island pattern will be transferred to substrate (Si or SiO$_2$) by performing chemical or plasma etching with the metal islands as an etch mask [36]. By employing an anisotropic etching process, the etched profiles will be designed to form mesa arrays with vertical sidewalls. The average spacing between nanoislands is designed to be smaller than the shorter wavelength part of solar spectrum, and this is achieved by adjusting the metal thickness and annealing condition. This self-organization-based nano-pattering will be particularly suitable for nano-texturing of pyramid-etched Si surfaces. In inductively-coupled-plasma reactive-ion etching (ICP-RIE), the RF power levels (2) can be adjusted to independently control kinetic energy and plasma density. By use of more kinetic plasma and also by tilt-mounting a wafer to plasma flux, an asymmetric mesa profile (similar to asymmetric saw-tooth profile in 1D grating case) will be obtained. This tilted mesa column, having vertical sidewalls only on one side, will be studied for enhancing glancing coupling in one direction, and the results will be compared with symmetric mesa array case. If the mesas are to be formed in silica or relatively low-index medium, a thin layer of

higher index, non-absorbing dielectric will be introduced for stronger vertical dipole couplings. The average spacing and island size distributions will be varied by adjusting the film thickness and anneal condition. Being aperiodic, the grating vectors available in the nano-island arrays will show a distribution in their magnitude (Fig. 4.3b). The range/distribution of grating vectors will set the diffraction condition for coupling into higher order beams. A quantitative relationship between the two (grating vector distribution and coupling efficiency into zero- or first-order glancing transmission) will be established for a wide range of incident angle and wavelength.

According to the reflection measurement (Fig. 3.16), the 1D mesa arrays reveal a certain degree of polarization dependence, with the TE' and TM' polarizations being identified as the ideal configuration for minimum reflectance in a wide angular range. An un-polarized light incident to a 2D mesa array can be viewed as a mixed state of four polarization configurations (TE/TM and TE'/TM'), and the overall reflectance can be approximated as an average of four cases.
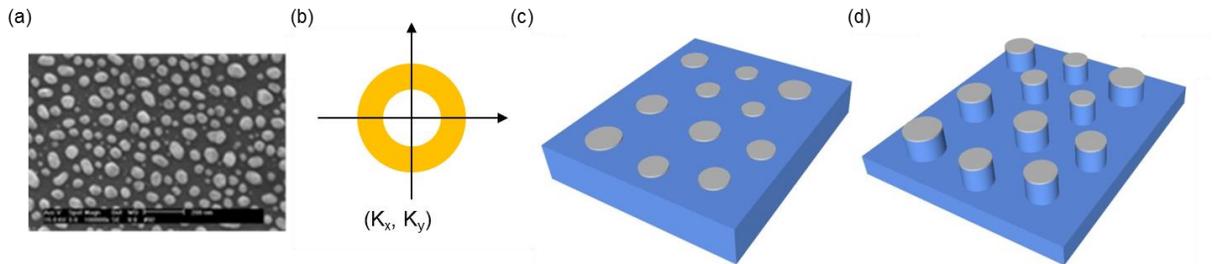
Figure 4.3 (a) SEM image of Ag nano-disks formed on silica surface. (b) Grating vector distribution of the Ag nano-particle array. (c)&(d). A schematic of fabricating nano-vertical steps: Self-organized metal nano-disks are used as an etch mask in plasma or chemical etching of silica or Si.

4.2.2 Applying nano-vertical steps on a finished cell

The nano-vertical steps using self-organized Ag nano-particles will be applied to finished cell surface. Fig.4.4 illustrates the schematic of process flow. A c-Si cell having a micron-scale pyramid-textured surface (ML Solar c-Si cell) and mc-Si cell having shallow round shape dent texturing (Everbright mc-Si cell) are used as a commercial cell (Fig. 4.5a,b). Commercial c-Si cell surface is typically coated with a 80-nm-thick SiN antireflection/passivation layer (Fig. 4.5c,d). An additional silicon nitride layer (~40 nm) is deposited on commercial cell surface by PECVD since the desired height of vertical dipole nano-mesas is expected to be ~80 nm. Then, the self-organization-based nano-pattering described in chapter 4.2.1 has been applied on SiN surface. A residual metal (Ag) is removed by chemical etching in nitric acid solution (diluted with DI water). Figure 4.6 shows the SEM images of each fabrication step on the mc-Si cell.
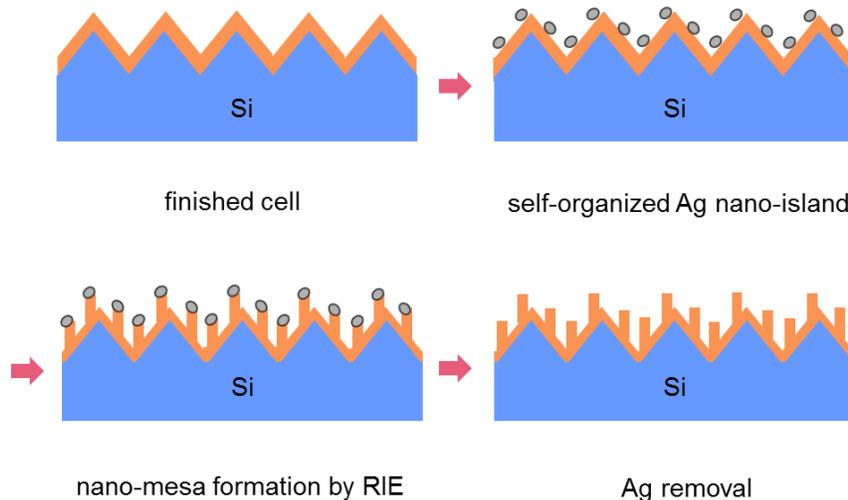
Figure 4.4 A non-lithographic manufacturing process for self-aligned vertical dipole structures.
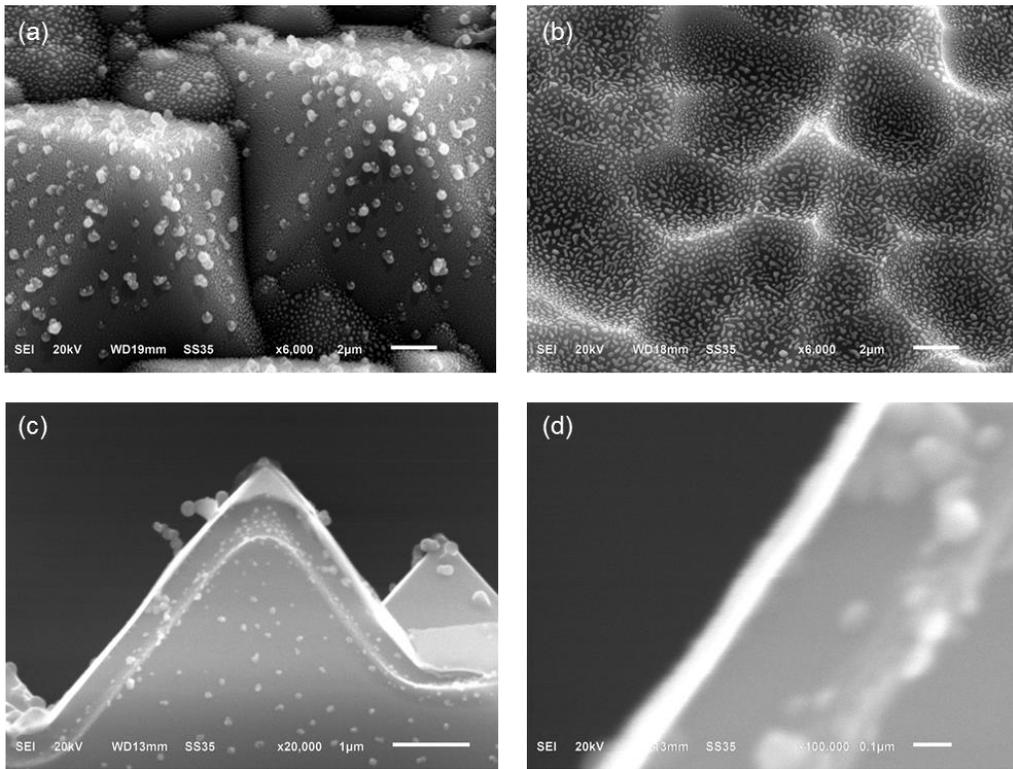
Figure 4.5 SEM images of commercial cells with Ag nanoislands. (a) ML Solar c-Si (b) Everbright mc-Si (top view) (c), (d) c-Si pyramidal textured cell (cross-sectional view).
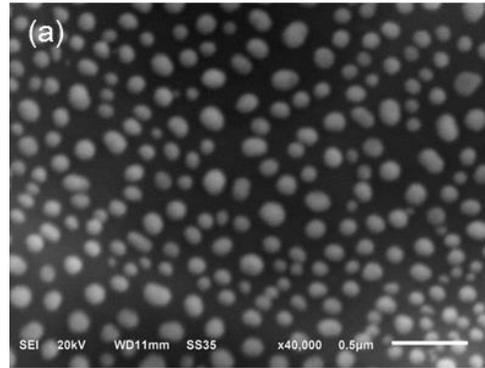
As-annealed Ag
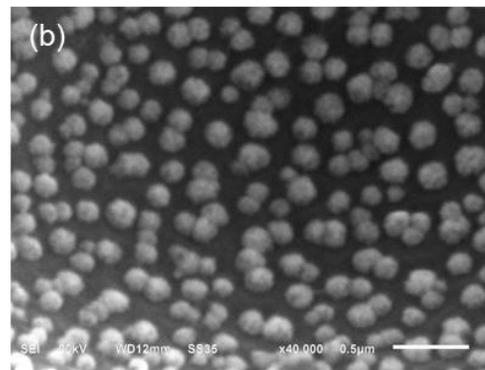
RIE
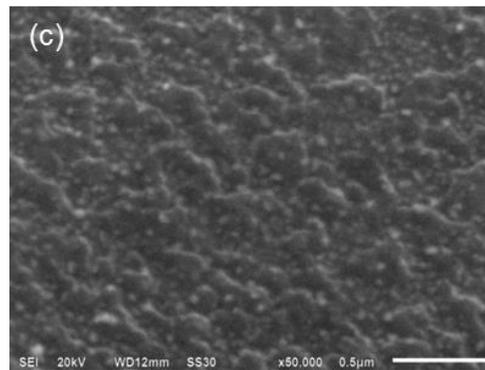
Remove Ag

Figure 4.6 SEM images of each fabrication step.

4.3 OPTICAL CHARACTERIZATION

4.3.1 Introduction

Before we proceed applying the silver nano-mesas on commercial cells and characterizing cell efficiencies, we tested the reflectance characteristics of Ag nano-mesa etched surfaces. Reflectance at 633 nm wavelength was measured on planar Si, pyramidal textured Si, silver particles on Si after annealing and nano-vertical steps on Si after removing silver. Self-organized metal nano-islands on pyramidal textured Si are used as an etch mask in plasma etching of silica or Si.

4.3.2 Results and discussion

Figure 4.7 shows the 633-nm reflectance of Ag nanoislands and nano-steps formed on planar or pyramidal Si. The reflectance shown in Fig. 4.7 (a) corresponds to planar surface with nano-vertical steps structure shown in Fig. 4.2 (a). The reflectance shown in Fig. 4.7 (b) refers to pyramid surface textured with nano-vertical steps structure shown in Fig. 4.2 (c). According to the measurement, the reflectance with pyramid-etched surface with 40-nm oxide is ~ 8 % at normal incidence. On the contrary, the vertical nano-textured pyramid surface has more chance to couple light into the direction along the junction interface so that reflection loss is expected to be less. From the graph (Fig. 4.7 (b)), the reflectance of pyramid surface textured with nano-vertical steps is further reduced, compared with the one without nano-mesas.
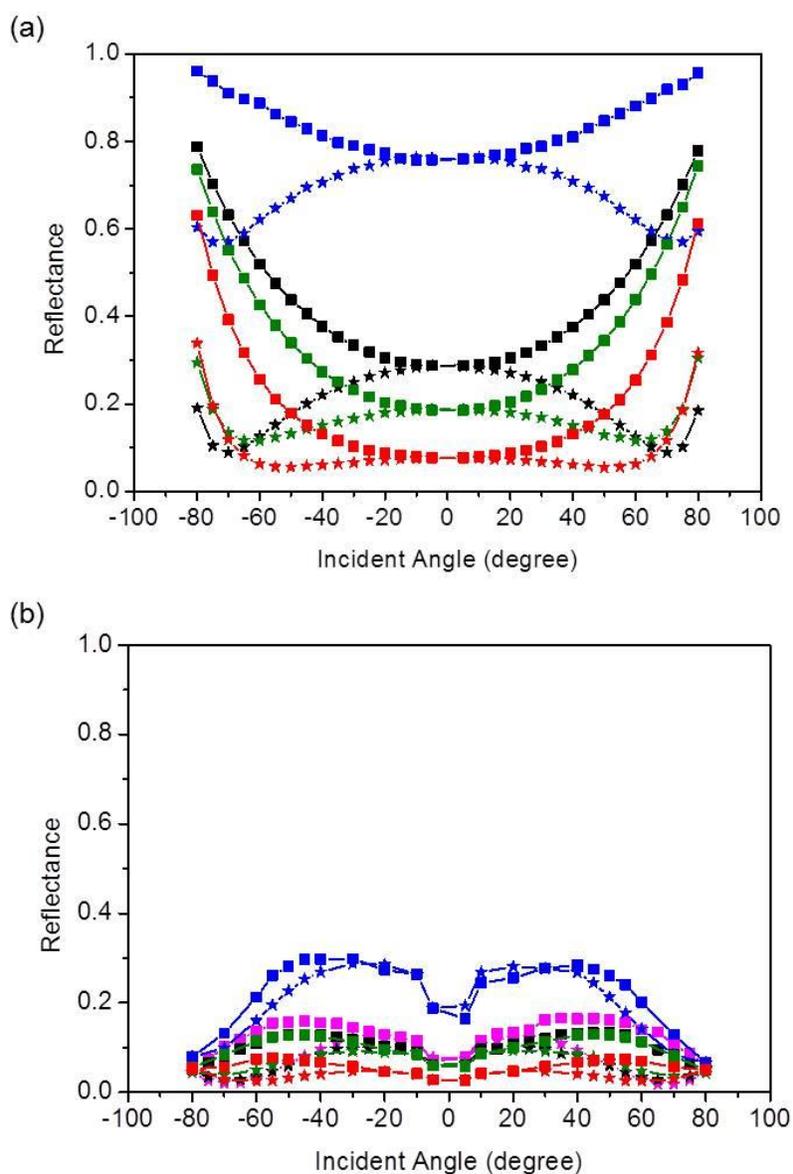
Figure 4.7 Reflectance measurement of Ag nano-steps formed on planar and pyramidal Si at 633 nm wavelength (a) planar Si with oxide (TE/TM) (black); 24 nm Ag deposition (TE/TM) (blue); Ag annealing (TE/TM) (green); removal of Ag (TE/TM) (red). (b) pyramidal Si (TE/TM) (pink); pyramidal Si with oxide (TE/TM) (black); 24 nm Ag deposition (TE/TM) (blue); Ag annealing (TE/TM) (green); removal of Ag (TE/TM) (red). The reflectance of panel (b) is with arbitrary unit and uncalibrated.

4.4   ELECTRICAL CHARACTERIZATION

4.4.1   Introduction

The standard condition for solar cell efficiency measurement is at air mass 1.5 spectrum (AM 1.5), intensity of 100 mW/cm^2 (1 kW/m^2, one-sun of illumination), cell temperature of 25 ˚C and with a four-wire *I-V* method.

In terms of defining the area of cell, three classifications can be applied. One is counting total area (t) which includes the total projected area of the cell or module. Second is called aperture area (ap) which means the illuminated area of device is masked so that the area is smaller than the total area of device but that includes essential components such as bus bars, fingers and interconnects. Designated illumination area (da) indicates the area that is masked for illumination which is smaller than the total device area, while major components of cell such as busbars are not included in the masked area [37]. In this measurement, we will use designated illumination area (da) that does not include busbars but includes fingers.

4.4.2   Results and discussion

A schematic of vertical dipole nanostructures on a finished cell and its I-V characteristic are shown in Fig. 4.8. Table 4.1 shows the efficiency table including solar cell parameters such as V_{oc}, I_{sc}, FF and conversion efficiency. Usually, the efficiency reaches to the maximum at optimum etching depth while it decreases at non-optimum etching depth controlled by time.

A c-Si has specific crystal orientation such as <100>, <111> and <110>. Therefore ML Solar c-Si cells are easily cut by a diamond pencil through crystal direction. Since the edges are already sharp and clean, edge cleaning is not necessary. We define ML Solar c-Si as-received cell as the cell which is cut into ~ 1 x 1 cm^2 with diamond pencil without any treatment.

Unlike c-Si cells that have crystal direction, mc-Si cells do not have specific direction because they consist of multiple small crystallites. Therefore, a diamond saw is used to cut a large piece of mc-Si cell into several small pieces in rectangular shape. The edges of small individual cells are then slightly etched by RIE to avoid contamination of diamond saw on the edges. Everbright mc-Si as-received cell indicates the cell which is cut into ~ 1 x 1 cm^2 with the diamond saw and edges are slightly treated by RIE.

The average efficiency of ML Solar c-Si and Everbright mc-Si as-received cell is in the range of 13.5 to 14.0 %. The as-received cell is compared to the cell treated with silicon nitride deposition, silver deposition, annealing, RIE and silver removal as described in chapter 4.2. If the RIE time is short (shallow etching depth), V_{oc} remains the same while J_{sc} slightly increases. Since nanopillars are very shallow, not optimized yet, the effect of light confinement by nanopillars may not be significant in these samples. At the optimum etching time and depth (shown in Table 4.1), V_{oc} still remains the same but J_{sc} significantly increases. Compared to as-received cells, the efficiency improves from 13.6 % to 17.0 % for ML Solar c-Si and 13.9 % to

87

16.0 % for Everbright mc-Si. The main improvement in efficiencies is coming from photo current (J_{sc} from 35.1 mA/cm^2 to 38.5 mA/cm^2 for c-Si and 35.2 mA/cm^2 to 38.4 mA/cm^2 for mc-Si) which indicates that nanopillars do help coupling light into Si.

Surface recombination has a major influence on the short-circuit current and the open-circuit voltage. If surface recombination rate is high, carriers generated in the cell can be reduced, which is harmful to get higher short-circuit current. Surface passivation is essential to reduce recombination rate by decreasing the number of dangling bonds at the top surface. Thermally grown silicon dioxide layer or silicon nitride is commonly used. Experimentally, for excessive etching of commercial cells, J_{sc} significantly decreases. Carrier collection which directly affecting the short-circuit current becomes tough because the passivation layer (Si_3N_4) might be damaged by deep etching.

Not only the current collection related to short-circuit current but also the forward bias injection current related to open-circuit voltage are affected by recombination losses. The saturation current and the light-generated current determine V_{oc}. Compared to J_{sc}, dark saturation current density J_0 has a relatively large variation; therefore V_{oc} mainly depends on J_0. Since J_0 depends on recombination, V_{oc} also depends on recombination in the solar cell. If recombination in the device increases, J_0 increases and therefore V_{oc} decreases. It was experimentally confirmed that V_{oc} decreases with long time of etching. A reduction in V_{oc} is caused by an increase in surface recombination due to passivation layer losses. As the RIE etching depth increases, the remaining surface passivation layer (Si_3N_4) reduces and eventually disappears. Some part of mesa can touch silicon which is undesirable in terms of surface passivation. Therefore, surface recombination increase and V_{oc} drop occur in consequence of surface passivation reduction. To avoid efficiency loss by J_{sc} and V_{oc} decrease, proper etching depth (time) which is enough for

making mesa but not destroying surface passivation needs to be found through rigorous optimization.
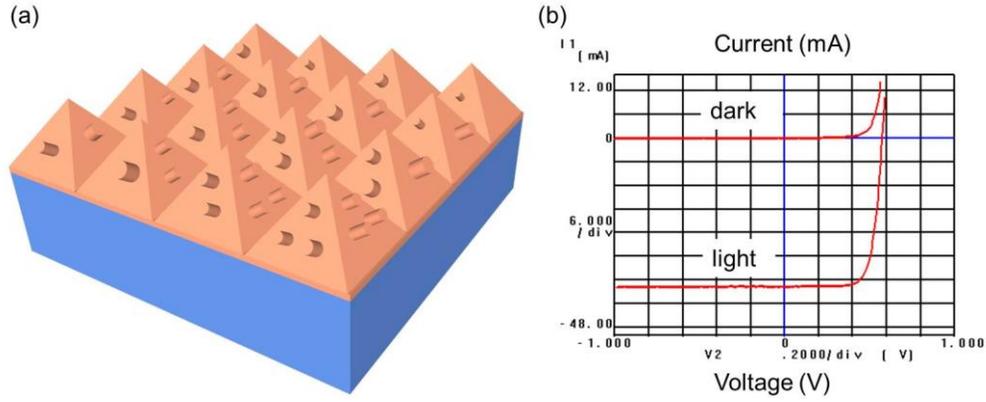
Figure 4.8 Nanoscale vertical dipole on a finished cell. (a) Schematic of nano-texture on pyramid cell. (b) I-V curves showing dark and photocurrent.

Table 4.1 Efficiency table for ML Solar c-Si and Everbright mc-Si cells (as-received and nanopillar cell)

Sample	Area (cm^2)	V_{oc} (V)	J_{sc} (mA /cm^2)	V_{max} (V)	J_{max} (mA /cm^2)	Efficiency (%)	FF (%)	R_s (Ω)	R_{sh} (Ω)
ML Solar c-Si as-received cell	1.020	0.579	35.1	0.469	29.0	13.6	67.0	1.3	4.3×10^2
ML Solar c-Si nanopillar cell	0.973	0.581	38.5	0.472	36.1	17.0	76.0	1.4	4.0×10^3
Everbright mc-Si as-received cell	1.243	0.581	35.2	0.463	30.1	13.9	68.1	1.5	1.7×10^3
Everbright mc-Si nanopillar cell	1.260	0.590	38.4	0.464	34.4	16.0	70.5	1.6	2.4×10^3

4.5   METAL-ASSISTED ETCHING

4.5.1   Introduction

In the metal-assisted etching phenomena reported in the literature it has been well known that the Si surface covered by noble metal is etched much faster than the off-metal area in an etchant composed of HF and an oxidative agent. Two possible mechanisms have been proposed: i) The reagent and byproduct occurred during oxidization and dissolution of Si atoms diffuse along the interface between the noble metal and the Si substrate. ii) A Si atom dissolved into noble metal and diffused through noble metal is oxidized and etched on the noble metal surface. [36] So far, metal-assisted etching has been mostly demonstrated in silicon with chemical etching [38] or plasma etching [39] in conjunction with use of noble metals(Ag, Au, Pt, etc.). In this study, we have observed metal-assisted etching in Ag-covered silicon nitride/Si with plasma reactive ion etching.

4.5.2   Results and discussion

For better understanding of silver nanoislands structure fabricated on commercial cells, a planar Ag(20nm)/SiN(260nm)/Si, Ag(20nm)/Si and Ag(20nm)/Quartz structure was prepared to see the effect of metal-assisted etching. Some part of top area was covered with photoresist to measure the step height between the fresh as-annealed silver area and the RIE exposed area. Table 4.2 shows the step thickness measured by surface profiler depending on etching time. An etching profile including the step and nanopillars is also explored by SEM shown in Figure 4.9.

Left part of image shows as-annealed silver nanodisks before etching while right part of image shows Ag/SiN nanopillars after plasma etching. According to the Table 4.2, metal covered SiN/Si or Si cases show much faster etch rate compared to bare SiN/Si or Si cases as a result of metal-assisted etching. SEM images support that the step between the as-annealed silver area and the plasma etched area is getting bigger as etching time increases. The silicon nitride thickness is also dramatically reduced as etching proceeds. This experiment reveals that controlling optimal mesa depth (height) and keeping an enough thickness of residual silicon nitride layer is a delicate and challenging task in terms of process optimization. Based on this study, two alternative methods have been developed. One is using AgO nanoisands that does not need to be etched or removed (chapter 4.6). The other one is using a non-metallic material as an etch mask that can form nanoislands in a non-lithographic process (chapter 5).

Table 4.2 Etched thickness of Ag (20 nm) on SiN/Si, Si and Quartz compared to bare SiN/Si, Si and Quartz.

Etching time	Ag(20nm)/SiN(260nm)/Si	Ag(20nm)/Si	Ag(20nm)/Quartz	SiN(260nm)/Si	Si	Quartz
1 min	40 nm	60 nm	15 nm	5 nm	55 nm	0 nm
2 min	130 nm	130 nm	25 nm	10 nm	75 nm	0 nm
3 min	180 nm	200 nm	27 nm	50 nm	95 nm	0 nm
4 min	310 nm	250 nm	35 nm	110 nm	105 nm	0 nm
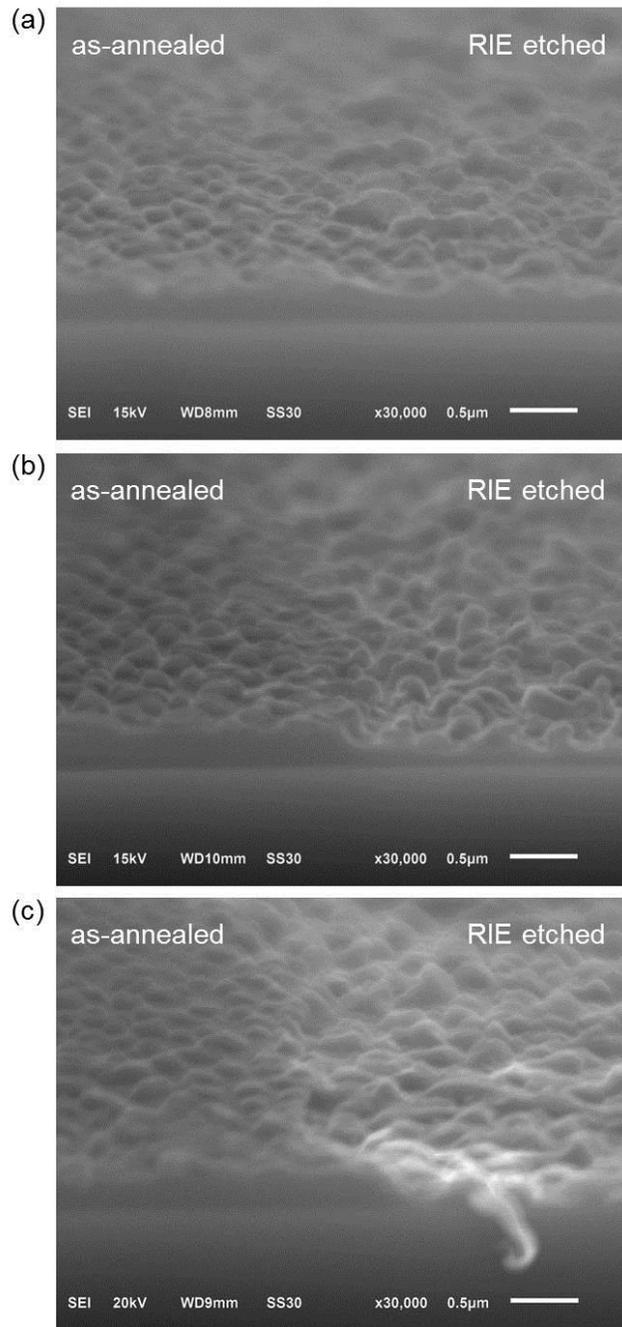
Figure 4.9 SEM images of reactive etching profile of Ag nanoparticles on SiN. Left: as-annealed

Ag, Right: RIE treated Ag (a) RIE 1 min (b) RIE 2 min (c) RIE 3 min.

4.6   REACTIVE SPUTTERED SILVER OXIDE NANOPARTICLES

4.6.1   Introduction

Use of metal as an etch mask incurs issues of excessively high etch rate of SiN caused by metal-assisted etching. As a result, it is challenging to optimize the mesa depth on SiN layer. However, we are still interested in utilizing the self-organized Ag nanodisks to make vertical dipole structures. Therefore, reactive sputtered AgO nanoparticles have been introduced on solar cell surface as an alternative to the etching process.

Considering that the thickness of AgO film will be increased after ballup of Ag, a customized cell with 50-nm-thick SiN layer was used in this work. An average thickness of AR after forming AgO nanoislands would be ~80 nm. Reactive sputtered deposition of thin AgO film in Ar/O_2 (50/50) ambient was followed by hot-plate annealing at 100 ˚C for 20 sec. The process only includes sputtered deposition and annealing which is very simple and efficient technique.

4.6.2   Results and discussion

Table 4.3 shows the comparison of solar cell parameters between the Aumex c-Si as-received cell and the processed cell. After performing AgO reactive sputtering and annealing, the cell efficiency increases from 16.2 % to 17.6 %. Since the V_{oc} remains the same while I_{sc} increases, the efficiency improvement can be explained as a result of the enhanced photocurrent. AgO nanostructures serve as vertical dipoles, therefore light transmission occurs along the glancing angle. This is a promising result that the conversion efficiency can be improved by simply introducing AgO nanoparticles on the cell surface. Non-etching process will be beneficial for reducing surface recombination loss that is proven by high V_{oc} and low contact resistance. Despite the benefit of this simple process, there exists a limitation that the height of mesas cannot be made high enough due to the non-etching based technique.

Table 4.3 Efficiency table for Aumex c-Si (as-received and nanopillar cell)

Sample	Area (cm^2)	V_{oc} (V)	J_{sc} (mA $/cm^2$)	V_{max} (V)	J_{max} (mA $/cm^2$)	Efficiency (%)	FF (%)	R_s (Ω)	R_{sh} (Ω)
Aumex c-Si as-received cell	4.424	0.618	35.49	0.516	31.41	16.2	73.9	0.30	1.8×10^2
Aumex c-Si nanopillar cell	2.823	0.620	37.41	0.520	33.94	17.6	76.0	0.43	6.0×10^2

4.7   SUMMARY

The vertical dipole nanostructures are introduced to a finished solar cell to confirm the nature of glancing transmission. Conventional pyramid-textured surface has a lensing effect, which causes Auger recombination of photocarriers resulting in reduced carrier lifetimes. In the cells with the pyramid surface with nanoscale vertical dipoles the lensing effect is alleviated, benefitting the longer wavelength regime operation of cells. The greater efficiency of nano-textured pyramid surface cells over the conventional pyramid surface cells clearly demonstrates the benefit of nanoscale vertical texturing.

The self-organized Ag nanoislands were formed on cell surface followed by reactive-ion etching. By controlling the metal thickness and the annealing condition, average spacing and island size can be adjusted.

The pyramid-textured Si with Ag nano-mesas show reduced reflectance compared to the one without nano-mesas. Since the vertical dipoles enable glancing transmission along the junction interface, reflection loss can be reduced. A solar cell with Ag nano-mesas was further characterized by performing I-V measurement at one sun AM 1.5 illumination. Photocurrent and cell efficiency improvement was observed for both c-Si cell and mc-Si cell cases.

In order to avoid excessive etching caused by metal-assisted etching, the non-etching process using reactive sputtered AgO nanoislands has been introduced. The nano-textured cell shows a better performance as a result of improved photocurrent and reduced surface recombination.

5.0   VERTICAL DIPOLE INTRODUCED TO A FINISHED CELL: TWO-DIMENSIONAL NANO-MESAS USING TIO2

5.1   INTRODUCTION

According to the silver nanoisland etching study, plasma etching of Ag incurs a complicated phenomenon through metal-assisted etching process. As an alternative method, we have introduced thin titanium dioxide (TiO_2) films as an etch mask that does not need to be removed afterwards.

TiO_2 thin films have been used as an anti-reflection coating (ARC), a mask for electroless metal plating, a passivation layer compatible with oxide, a diffusion barrier to phosphorus and a dopant source for emitter diffusion [40]. A wide use of TiO_2 thin films is based on cost effectiveness, excellent chemical resistance and optimal refractive index $n \approx 2.5$ for encapsulated silicon solar cells. In our application, discontinuous TiO_2 thin films deposited on silicon nitride serve as an etch mask to form nano-mesa structure. TiO_2 nanoislands can remain on the surface after RIE.

5.2 FABRICATION PROCESS

Similar to the Ag nanoislands case, we have employed crystalline Si cells as a base structure and applied a TiO_2 vertical-dipole nano-optic structure on the cell surface. Figure 5.1 shows the fabrication process scheme of nano-mesa formation using TiO_2 thin films. First, a thin layer (~3 nm) of TiO_2 is sputter deposited on top of a SiN passivation layer. At this nucleation stage of thickness the TiO_2 film forms discontinuous nanoislands of ~200nm diameter and 10-20nm gaps in between. The rf magnetron sputtering condition of TiO_2 is stated in a Table 5.1. A plasma reactive ion etching (RIE) is then performed to form narrow trenches/holes into SiN using the TiO_2 islands as a self-organized, self-aligned etch mask. TiO_2/SiN shows a good etch selectivity (<1/20) for CF_4/O_2 etch gas. The etch depth is controlled to be 50-70nm so that there remains a residual thickness (20-30nm) of SiN at trench bottom for surface passivation and the trench has a relatively high aspect ratio of ~1/4. Fig. 5.2 shows an SEM image of trench-etched surface of SiN-passivated Si.

RIE etching time was adjusted to get an optimum mesa profile shown in Fig. 5.3. For less-etching time of RIE (Fig. 5.3 (a)), many part of TiO_2 nanoislands were connected resulting in relatively shallow mesas. For optimum-etching time of RIE (Fig. 5.3 (b)), TiO_2 nanoislands were left on the top while silicon nitride between nanoislands was etched resulting in ideal mesas having proper depth and texturing. For over-etched case (Fig. 5.3 (c)), most part of TiO_2 nanoislands were etched away, therefore, nano-mesas became very shallow. Thus, adjusting RIE time is critical to fabricate proper TiO_2 nanoislands mesa structures.
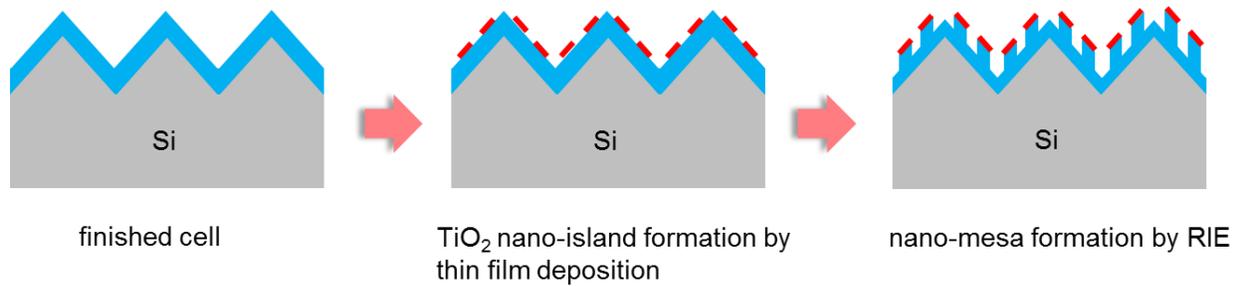
Figure 5.1 Fabrication process scheme of TiO$_2$ nano-mesa structure.

Table 5.1 The rf magnetron sputtering condition of TiO$_2$.

Target	TiO$_2$ (9/23/91)				
Target to substrate distance	2 inch				
RF power	30 W	20 W		15 W	
Gas	Ar				
Gas pressure	~ 5 mTorr				
Substrate temperature	room temperature				
Sputtering time	30 min	30 min	1 hr	1hr	2hr
TiO$_2$ measured thickness by a-step	55 nm	22 nm	42 nm	16 nm	32 nm
Deposition rate	1.83 nm/min	0.73 nm/min	0.7 nm/min	0.27 nm/min	0.27 nm/min
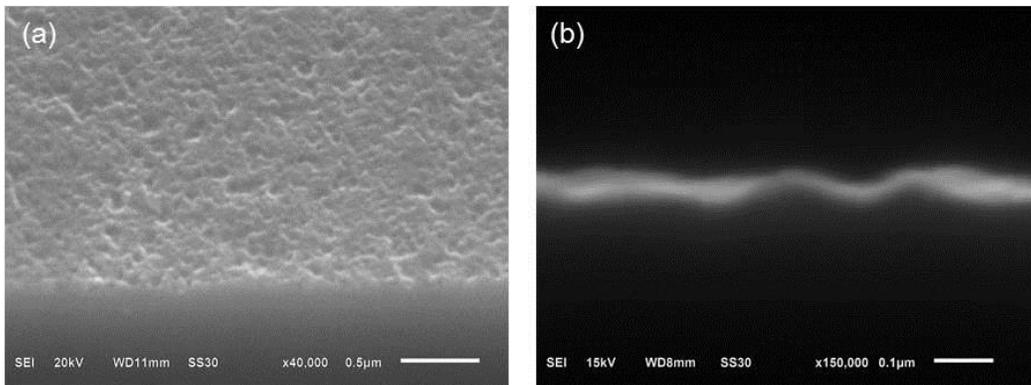
Figure. 5.2 SEM images of nano-mesas using TiO_2 masks.
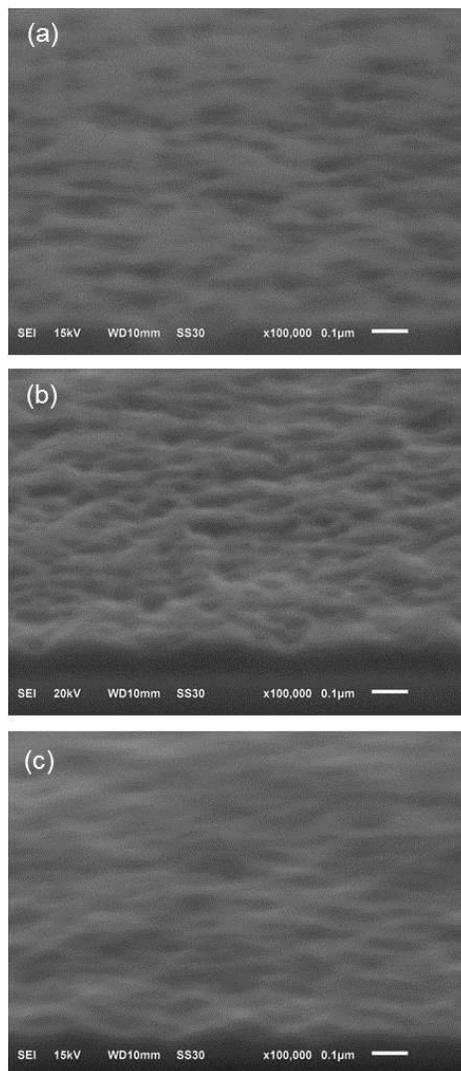
Fig. 5.3 SEM images of TiO_2 nanoislands depending on the etching time. (a) less-etching (b) optimum-etching (c) over-etching.

5.3   OPTICAL CHARACTERIZATION

5.3.1   Introduction

The reflectance of TiO$_2$ nano-mesa-etched surfaces was characterized at 633 nm wavelength. For optimum mesa depth of 70 − 80 nm (mesa center 35 − 40 nm), 110 nm-thick silicon nitride films were prepared on a planar Si substrate. Sputter deposition of TiO$_2$ nanoislands was performed, followed by RIE etching of SiN for mesa formation.

5.3.2   Results and discussion

In a broad range of incident angle from 0º to ±80º, reflectance of the TiO$_2$(2 or 2.5 or 3 nm)/SiN(110nm)/Si substrate was measured at 633 nm wavelength depending on various RIE time shown in figure 5.4. As RIE time increases, the reflectance decreases to nearly zero and then increases again. This means there is an optimum RIE time giving the lowest reflectance (near-zero reflectance) in accordance with optimum mesa depth. For 2, 2.5 and 3 nm-thick TiO$_2$ films, 6, 9 and 12 min etching time gives the lowest reflectance. According to the SEM images shown in figure 5.3, the depth of nano-mesas formed at the optimum time is around 50 − 70 nm. Considering that a RIE time for etching 50 − 70 nm silicon nitride is 3 min at the same condition, the optimum RIE time range from 6 min to 12 min for TiO$_2$ nanoislands on SiN/Si is relatively long. This indicates that an extra etching time is consumed for etching initial TiO$_2$ nano-films on silicon nitride and then thinner TiO$_2$ area is etched into silicon nitride while thicker TiO$_2$ area is still being etched. Consequently, TiO$_2$ nanoisland mesa structure can be formed at an optimal

RIE time. The difficulty of TiO$_2$ nano-mesa fabrication is coming from the delicate optimization that includes proper thin TiO$_2$ thickness which can make discontinuous nanoislands yet enough TiO$_2$ thickness which can make substantial nano-mesas.
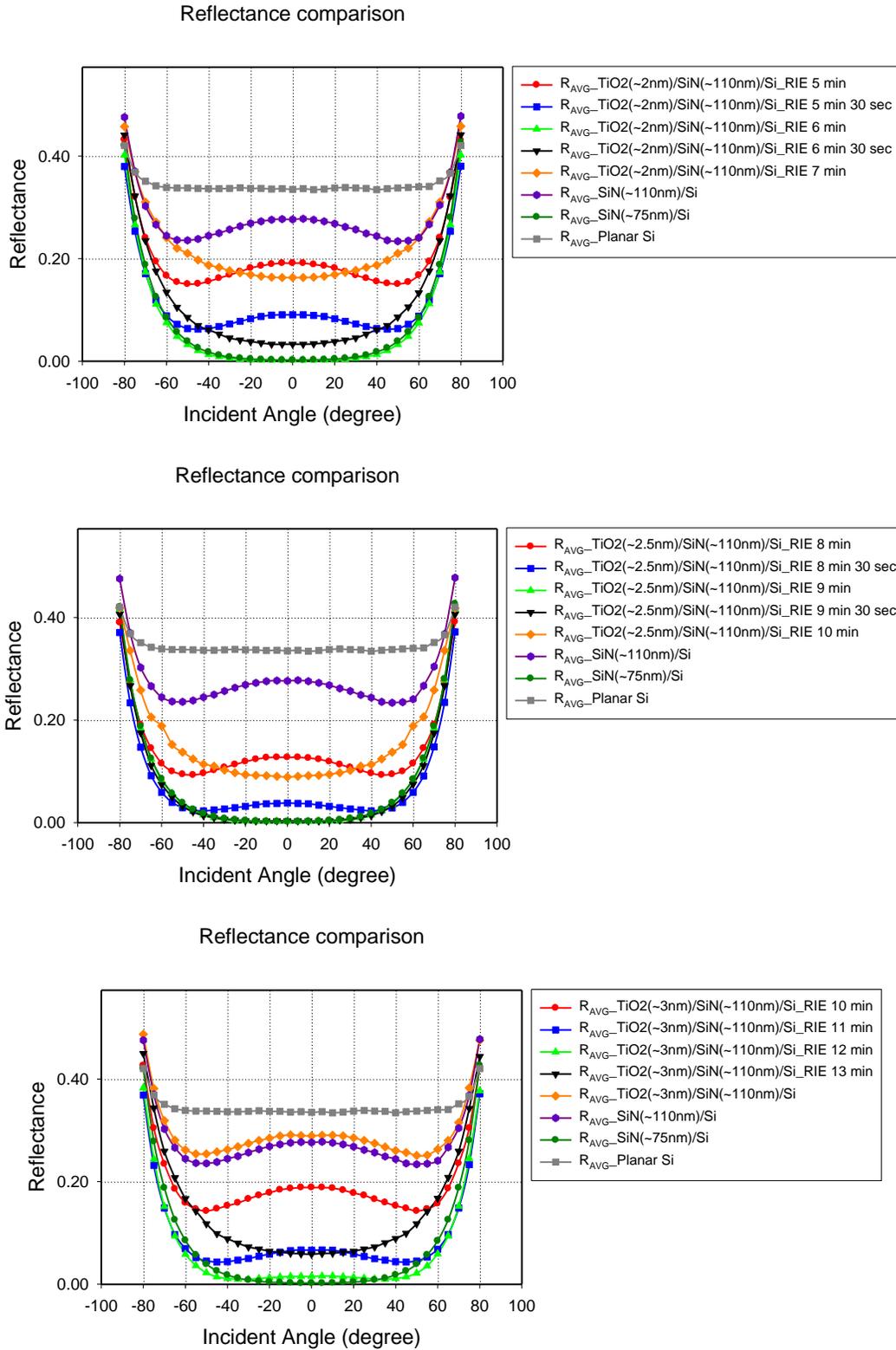
Figure 5.4 Reflectance measurements of 2, 2.5 and 3 nm-thick TiO$_2$ nanofilms on SiN/Si substrate after RIE at 633 nm wavelength.

5.4 ELECTRICAL CHARACTERIZATION

5.4.1 Introduction

Near-zero reflectance of TiO_2 nano-mesas on SiN/Si supports the possibility of higher photocurrent and higher conversion efficiency when the mesas are applied to real cells. The effect of TiO_2 nanoislands mesa structure on solar cell performance has been tested by I-V measurement. Similar to the measurement of silver nanoislands commercial cells, solar cell parameters were measured under 1 sun, air mass 1.5 illumination.

20 nm-thick additional silicon nitride PECVD-deposition was followed by 2.5 nm-thick TiO_2 sputter-deposition on c-Si (Hyundai) cells. RIE power of 20 W was applied to etch silicon nitride.

5.4.2 Results and discussion

The spectral dependence of reflectance was characterized for c-Si cells with and without a vertical-dipole nano-optic texture (Fig. 5.6). The reflectance remains low for most of the range. The nano-optic texture is found to reduce the reflectance in the visible to NIR range (600-1000nm).

Fig. 5.5 shows the current-versus-voltage (I-V) characteristics of c-Si cells with and without vertical dipoles measured under standard AM1.5 illumination. This measurement result was independently validated by Newport Corporation's ISO-certified photovoltaics measurement laboratory. The cell size was varied from 1.0 cm^2 to 6.0 cm^2. The vertical dipole cell (1.0 cm^2) shows 19.8 % efficiency. This is compared to 16.3% efficiency of a c-Si cell (1.0 cm^2) without

vertical dipoles. For larger size cells (6.0 cm^2) the vertical dipole cell shows 18.8% efficiency while a control cell without vertical dipoles shows 16.3 % efficiency. This corresponds to ~20 % improvement of commercial c-Si cells.

Table 5.2 summarizes measured cell performances: open circuit voltage (V$_{oc}$), short circuit current (J$_{sc}$), maximum voltage (V$_{max}$), maximum current (J$_{max}$), fill factor (FF), series resistance (R$_s$), and shunt resistance (R$_{sh}$). Comparing the two samples with and without vertical dipoles, it is clear that the efficiency improvement is mainly due to the enhanced photocurrent, i.e., J$_{max}$ of 40.6 mA/cm^2 for vertical dipole cell versus 33.6 mA/cm^2 for control cell (without vertical dipoles). This photocurrent enhancement is attributed to the enhanced performance of light absorption and carrier transport/collection enabled by glancing coupling of light via vertical dipoles at nano-mesas.

In order to develop a better understanding of the efficiency improvement, external quantum efficiencies (EQE) of both cells with and without vertical dipoles were characterized and compared (Fig. 5.6). The peak EQE reaches 98 % level at ~800 nm wavelength. A major improvement is observed in the NIR (100-1100 nm). The external quantum efficiency η_e refers to the ratio of photocarriers collected over incident photons and is related to the internal quantum efficiency (IQE) η_i, which is defined as the ratio of photocarriers collected over photons absorbed: $\eta_i = \eta_e/(1-R)$, where R is the reflectance at cell surface. Considering the reflectance and EQE spectra of both cells it is clear that the efficiency improvement in vertical dipole cells is contributed by: enhanced absorption of light in 600-1100 nm ranges and enhanced transport/collection of photocarriers in the same wavelength range. The enhanced absorption can be ascribed to reduced reflection and/or enhanced absorption of transmitted photons. Here a reduced reflection is a simple antireflection effect of textured surface, whereas the enhanced

absorption of transmitted light is due to the glancing coupling by vertical dipoles. In the 600-1100 nm range, the IQE improvement is more significant than the reflectance change, and this indicates the dominant contribution of glancing coupling for enhanced absorption.
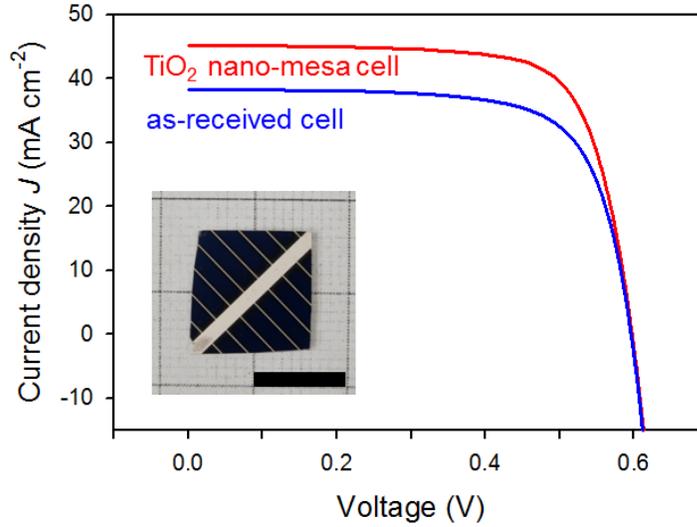
Figure 5.5 I-V characteristics of a reference cell and a TiO_2 nano-mesa cell.

Table 5.2 Efficiency table for Hyundai c-Si (as-received and nanopillar cell).

Sample #	Area (cm²)	V_{oc} (V)	J_{sc} (mA /cm²)	V_{max} (V)	J_{max} (mA /cm²)	Efficiency (%)	FF (%)	R_s (Ω)	R_{sh} (Ω)
as-received cell (small size)	1.37	0.595	38.3	0.486	33.6	16.3	71.7	0.9	9.4×10^2
nano-mesa cell (small size)	1.18	0.597	45.1	0.488	40.6	19.8	73.7	1.0	1.4×10^3
as-received cell (large size)	6.20	0.615	35.7	0.503	32.4	16.3	74.1	0.24	1.5×10^2
nano-mesa cell (large size)	5.99	0.620	39.0	0.514	36.6	18.8	77.8	0.22	8.4×10^2
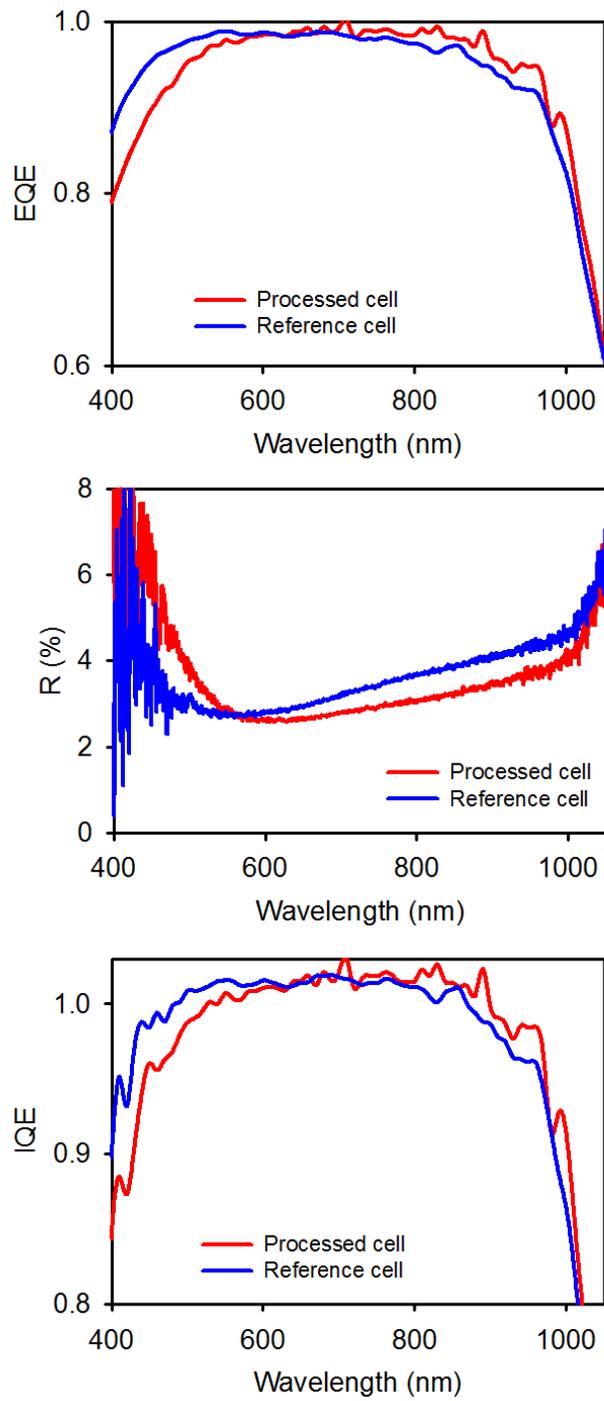
Figure 5.6 Measured reflectance, EQE and IQE spectra of c-Si cells with and without vertical dipoles.

5.5   SUMMARY

A TiO$_2$-basedvertical-dipole nano-optic structure was developed and applied on a finished c-Si cell surface. The TiO$_2$ at the thickness range of nucleation stage forms nano-islands as-deposited. Thess self-organized nano-islands are used as an etch mask in plasma etching into a SiN passivation layer. Etch selectivity of TiO$_2$/SiN is good enough to control the etch rate/depth for CF$_4$/O$_2$ etch gas.

The etch depth was controlled by etch time and was optimized by measuring the reflectance of nano-texture surface at 633 nm wavelength. Various thicknesses of TiO$_2$ nanofilms were also tested to find out the optimum mesa etching condition. The mesa-etched surface showing a lowest reflectance corresponds to the cell that demonstrates the highest efficiency. The *I-V* measurement of c-Si cells with and without vertical dipoles demonstrates an improved efficiency in the vertical dipole cell (16.3 % to 19.8 % for small cells and 16.3 % to 18.8 % for large cells). TiO$_2$ nano-mesas on the cell surface serve as vertical-dipoles, which couple more light into glancing directions inside Si. The vertical dipole cell shows improved EQE and IQE in the NIR (600-1100 nm) range. The glancing coupling by vertical dipoles leads to the enhanced absorption of transmitted light.

6.0 PHOTOCARRIER MULTIPLICATION IN TWO-DIMENTIONAL ELECTRON GAS OF A GRAPHENE/OXIDE/SI STRUCTURE

6.1 INTRODUCTION

Generating multiple electron-hole pairs from an absorbed photon is a promising approach to high-efficiency solar energy conversion. Carrier multiplication by impact ionization commonly requires high electric field or above-bandgap excess photon energy [41-54]. In semiconductor nanocrystals, quantum confinement effects relax the momentum conservation requirement, enabling multiple exciton generation (MEG) with reduced threshold energy [49]. Extracting the generated electron-hole pairs out of nanocrystals and transporting them into photocurrent, however, remains a challenge in device-level exploitation of the phenomenon. Unlike the case of MEG by excess photon energy, carrier multiplication by high-field impact ionization is attainable over a broad spectral range. The requisite field strength, however, translates to an excessively large bias, typically greater than 50 V when implemented in a bulk p-n junction structure [55], rendering it incompatible with photovoltaic devices. In a desirable scenario for field-assisted impact ionization, an electron must attain the threshold energy within the mean free path so that impact excitation can get a better chance than phonon scattering. In silicon the phonon mean free path is 6-8 nm and therefore a field strength $> 1\text{x}10^6$ V/cm would be needed to reach the threshold level (~3 eV) [55].

In this chapter, we report low-external-voltage and yet high-internal-field impact-ionization carrier multiplication in a 2DEG layer induced in a graphene/oxide/Si structure. Here the 2DEG channel at SiO_2/Si interface is designed to provide vertical (transverse) confinement of photocarriers generated in Si, while the channel itself serves as a conduit for horizontal (longitudinal) transport as well. The 2DEG layer is terminated by a vertical trench, which is covered by suspended graphene on top. Photoelectrons at the edge of 2DEG emit into air (nanoscale void channel) and make a ballistic transport toward graphene electrode [56, 57]. This hybrid configuration, *i.e.*, a 2DEG channel cascaded by a vertical void channel in a capacitor structure, is found to enable accumulation of carriers to large concentration at the channel edge, thereby highly-localized strong electric field, inducing impact-ionization at low bias. This broadband, low-voltage photocarrier multiplication offers a new approach to developing high-efficiency solar cells when the structure is designed to have sufficient built-in field (*i.e.*, open-circuit voltage) by choosing junction materials with proper work functions [58, 59].

6.2 METHODS

6.2.1 Fabrication

The graphene/SiO$_2$/Si structure with a void channel was fabricated by employing electron-beam lithography (EBL) and reactive-ion etching (RIE) process (Fig. 6.1). A 23-nm-thick SiO$_2$ layer was first grown by thermal oxidation on p-type silicon (boron-doped, resistivity = 10 Ω-cm) wafers ((100)-oriented; thickness, 525 μm). An Al Ohmic contact was prepared on the back side of Si substrate by thermal evaporation (Al thickness, ~150 nm), followed by annealing at 350˚C. A narrow stripe pattern (340-nm-width, 1-mm-length trench) was defined in the polymethylmethacrylate (PMMA, ~200nm thickness) layer using electron-beam lithography (Raith e-Line: 10keV, beam current 220pA). The e-beam patterned substrate was etched to 210nm depth by performing RIE in CF$_4$/O$_2$ ambient. The PMMA was removed in acetone. Finally, a monolayer graphene was transferred to the trench-etched SiO$_2$/Si substrate. The sample was dried at ~70˚C for 2 hours to remove moisture trapped in the void-channel. The thus-fabricated samples reveal graphene membranes that are suspended flat on trench-etched substrate (Fig. 6.2b).

6.2.2 Characterization

I-V characteristics of the graphene/SiO$_2$/Si structure were measured in room-temperature air ambient, with a semiconductor parameter analyzer (HP4145B) in conjunction with use of a probe station. Tungsten probes (tip radius of curvature, ~2 μm) were used in contacting the top (graphene) and bottom (Al) electrodes. The voltage scan was performed with a step size of 0.015

V. Photo *I-V* characteristics were measured in the UV-to-IR range, using He-Cd laser (325nm), He-Ne laser (633nm), diode-pumped solid state lasers (532nm and 1064nm), and semiconductor diode lasers (407nm, 653nm, 780nm, 808nm, 850nm, and 980nm) as input light source. The input power was calibrated with a digital optical power meter (Thorlabs PM100 with S130A or S130VA sensor).
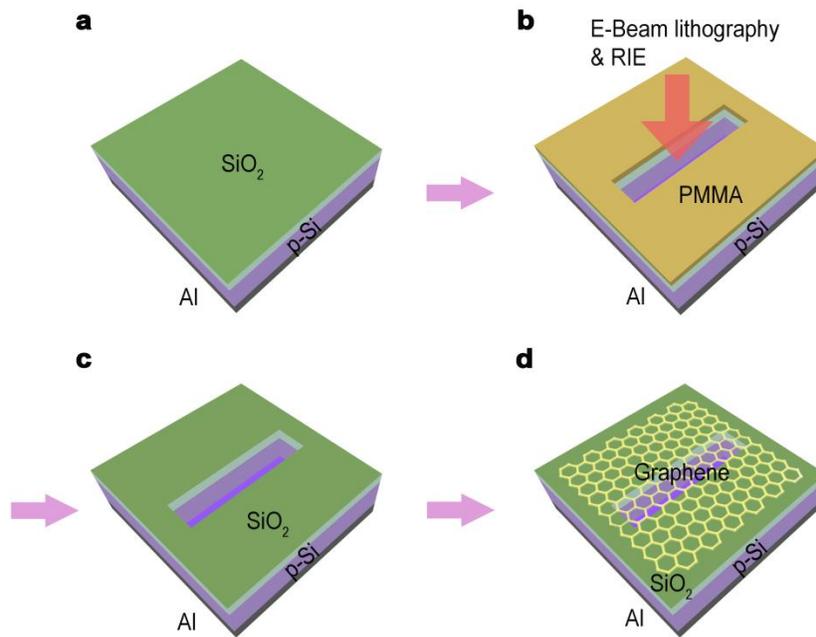
Figure 6.1 Schematic of fabrication process of the graphene/SiO$_2$/Si structure.
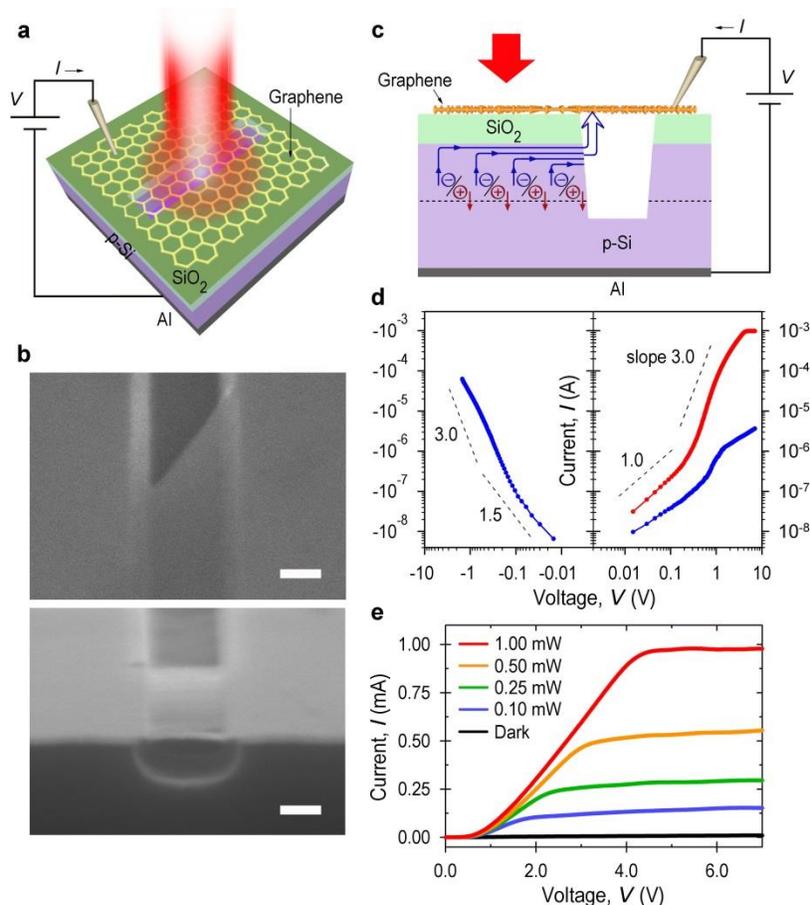
Figure 6.2 Photocurrent-versus-voltage characteristic. **a**, Schematic of a graphene/SiO$_2$(23nm)/p-Si structure with a trench (340nm width, 210nm depth, 1-mm length) covered by a suspended graphene electrode (3mm x 4mm). A laser beam (1mm diameter) illuminates the graphene electrode. **b**, SEM images of monolayer graphene placed on top of a trench: plan view (top) and cross-section (bottom) images. Scale bar, 200 nm. **c**, Schematic of photocurrent flow under reverse bias. Photocarriers generated in Si are separated by depletion field: photoelectrons form a 2DEG at Si/SiO$_2$ while photoholes flow to substrate. The 2DEG flows into/accumulate at the channel edge while some are exiting into air and traveling toward graphene electrode. **d**, Measured *I-V* characteristics: dark- (blue) and photo-current (red) under 1-mW illumination (633-nm wavelength). **e**, Measured photo *I-V* for different input power levels.

6.3   RESULTS AND DISCUSSION

6.3.1   Dark and photo I-V analysis

First, the dark current-versus-voltage (*I-V*) characteristic was analyzed in order to understand the emission and transport properties of the quasi-two-dimensional electron gas accommodated at the materials interface in the Si or graphene side. In the case of forward bias (*i.e.*, graphene electrode negatively biased with respect to p-Si substrate; Fig. 6.2d, blue: $V < 0$), a 2D hole system (2DHS) develops in Si while a 2DEG forms in graphene. Due to Coulombic repulsion of electrons around the aperture edge, the 2DEG in graphene emits into air and travels down toward the edge of 2DHS at SiO_2/Si [56, 57]. The electrons injected into air form a space charge around the bottom part of the channel [60 ,61]. As the forward bias increases, more electrons are induced in the suspended graphene. Presence of electrons in the void channel (top part) results in reducing the space charge field originating from the bottom part, similar to the case of space charge neutralization in a graphene/SiO_2/n-Si structure under forward bias [57,62]. The decrease of space charge field at larger bias enhances cathode-emission (2DEG emission from graphene edge), as demonstrated by a faster rise of channel current compared to that at lower bias (*i.e.*, V^3 versus $V^{1.5}$). In reverse bias, most of initial voltage goes to depletion region formation in Si, therefore the *I-V* characteristic demonstrates a slope smaller than 1.5 (Fig. 6.2d, blue: $V > 0$).

The photo *I-V* characteristic of graphene/SiO_2/p-Si structure was measured under illumination with a 633-nm laser light (1-mm beam diameter) (Fig. 6.2a). In reverse bias the photocurrent saturates at 1.8-4.3V for 0.1-1.0mW input power (Fig. 6.2e). Under 0.25-mW illumination, the saturation photocurrent is read to be 0.25 mA at 2.7 V (Fig. 6.2e, green). This

corresponds to a responsivity of 1.0 A/W and external quantum efficiency (EQE) of 200% (internal quantum efficiency of 300%). The dark current is measured to be 1.6-3.6 μA at 2.2-7.0 V, resulting in an on/off current ratio of 225–270 at 1.0 mW input power (Fig. 6.2d, e). The responsivity measured at input power of 0.1 to 1.0 mW remains nearly constant at 0.9-1.1 A/W, demonstrating reasonably good linearity.

The absorption depth of Si is 3.0 μm at 633 nm wavelength. Since a monolayer graphene absorbs only 2.3 % of incident light, most photons are absorbed in/near the depletion region (910-940nm width at 2-5V reverse bias). The photogenerated carriers are separated by depletion field, and photoelectrons drift to the Si/SiO_2 interface forming a 2DEG inversion layer. Similar to the dark forward-bias case [57], Coulombic repulsion among electrons around the channel edge enables low-voltage emission of 2DEG into air. Emitted electrons travel ballistically in the nano-void channel. Some of them are captured/collected at the edge of 2DHS induced in the graphene side, while majority pass through the suspended graphene (Fig. 6.2c). The transmitted electrons form a space charge outside the suspended graphene. Once a space charge region is established, further transmitting electrons are collected by the graphene electrode on SiO_2. Photoholes separated in the depletion region drift down to the substrate side. Photoelectrons in 2DEG, traveling along the horizontal (longitudinal) direction, accumulate at the channel edge, while some exit through the edge, emitting into air. This local accumulation of electrons around the edge induces some of the photoholes to be held back near the depletion region boundary. The closed-circuit nature (*i.e.*, charge conservation) of this two-terminal operation with a suspended graphene electrode (Fig. 6.2c) was confirmed by performing *I-V* measurements in air or vacuum ($\sim 10^{-6}$ Torr) with the system ground connected to the bottom (cathode) or top (anode), which demonstrate the same amount of channel current for given bias voltage [57].

Here we note that the measured photo *I-V* of reverse-biased p-Si sample reveals the same voltage dependence as the dark forward-biased n-Si case [57]: V^3 dependence of photocurrent at 0.3-1.0 V (Fig. 6.2d, red), much faster than the $V^{1.5}$ dependence of Child-Langmuir's space charge limited current [60, 61]. This observation confirms that a suspended graphene electrode plays the same role of neutralizing electron space charge in the void channel and thereby enhancing cathode emission.

6.3.2   Spectral dependence of photocarrier multiplication

The spectral dependence of photocurrent responsivity was characterized in the UV-to-NIR range (325-1064 nm) at input power of ~0.25 mW (Fig. 6.3). The internal quantum efficiency (IQE) shows a three-step cascade profile: an initial rise to 230% level at ~850 nm, followed by an increase to 300% level at ~650 nm, and a ramp-up to 380% at <400 nm. At steady state the saturation photocurrent is balanced by the photocarrier generation in Si. The IQE greater than 100% indicates multiplication of photocarriers. The spectral dependence of IQE without a carrier multiplication effect is calculated and shown for comparison (Fig. 6.3a, dashed) [55].

The three-step-cascade profile observed with the graphene/SiO_2/p-Si structure suggests that different mechanisms are involved in carrier multiplication depending on spectral range. The first regime that covers the NIR (>~800 nm) corresponds to near-band-edge absorption. Since the amount of above-bandgap excess energy is negligible in this regime, the underlying mechanism is believed to involve a field-assisted process. In order to substantiate this observation and to elucidate the underlying mechanisms we have analyzed the electric field distribution in the

graphene/SiO$_2$/Si structure and calculated impact ionization rates and carrier multiplication factor under illumination (Fig. 6.4).

The saturation photocurrent is determined by photocarrier generation rate in Si and is expressed as $q\eta P_{in}/h\nu$, where q is the electron charge, η is the external quantum efficiency, P_{in} is the power incident to graphene electrode, and $h\nu$ is the photon energy. For 1-mW illumination with 800-nm light (1-mm beam diameter), the photogeneration rate is calculated to be 2.7×10^{17} s^{-1}cm^{-2}. This corresponds to a photocarrier density of 8.2×10^{12} cm^{-2} when assuming a minority carrier (electron) lifetime of 30 μs in Si [63]. The photogenerated electrons drift to the Si/SiO$_2$ interface and flow along the 2DEG channel. The channel edge at the trench becomes a bottleneck for continuous flow of electrons (*i.e.*, exit flux into air), since the emission of 2DEG at the edge is limited by the space charge effect in the void channel. Photoelectrons then accumulate at the edge while some return. The local 2DEG density at the bottleneck is expected to stabilize at a certain level due to a negative feedback effect discussed below.

Across the oxide layer of the capacitor structure, the graphene side will have accumulation of positive charge (holes) to the same level as that of net negative charge in Si [64]. The peak hole concentration in graphene is expected to be limited to/stabilized at $\sim 1 \times 10^{13}$ cm^{-2}. Beyond this level the electric field in SiO$_2$ ($> \sim 5 \times 10^6$ V/cm) would reach the breakdown regime [65], and carriers (holes) generated by an avalanche process will neutralize the photoelectrons accumulated in Si reducing the concentration to a stable level. At this level of hole concentration the Fermi level of graphene is ~ 0.4 eV below the Dirac point [64]. A further rise of hole density would lower the graphene's Fermi level and thereby decrease the flat band voltage (V_{FB}) such that the band bending in Si becomes less, lowering the 2DEG density. Overall this negative feedback effect is expected to limit/stabilize electron accumulation to

~$1\text{x}10^{13}$ cm^{-2} level. In the Si side the accumulated electrons will attract holes that are being generated in the depletion/neutral region. The photoholes induced by this Coulombic interaction will form a space charge region at the depletion/neutral boundary, altering the field and potential distributions.
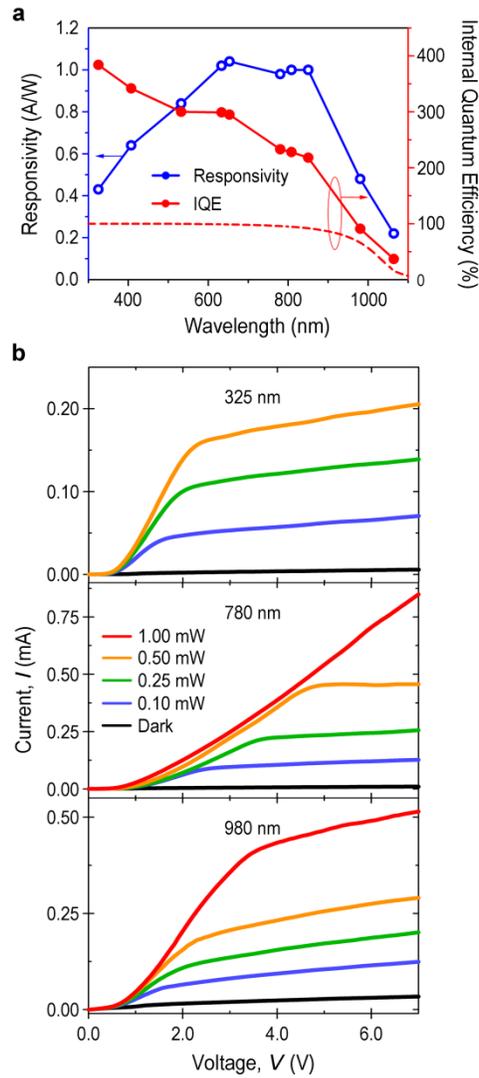
Figure 6.3 Spectral dependence of photocurrent responsivity and quantum efficiency. **a**, The photo *I-V* characteristics of a graphene/SiO$_2$(23nm)/p-Si structure with a trench were measured at 325–1064nm with input power of ~0.25 mW. The spectral dependence reveals a three-step cascade profile with internal quantum efficiency of 220-380% at <850nm, implying broadband photocarrier multiplication. The internal quantum efficiency calculated without a multiplication effect is shown for comparison (red, dashed). **b**, Photo *I-V* characteristics measured at three different wavelengths (325, 780, and 980nm) with different input power.

6.3.3 Impact ionization in 2D electron gas

Fig. 6.4 shows the field and potential profiles at the channel edge calculated assuming the following charge distribution: holes in graphene (1.0×10^{13} cm^{-2}); electrons in 2DEG (1.0×10^{13} cm^{-2}); depletion charge (1.3×10^{11} cm^{-2} = 1.3×10^{15} cm^{-3} x 1 µm); holes at depletion boundary (1.3×10^{11} cm^{-2} = 1.4×10^{14} cm^{-3} x 9 µm). Note that the hole density in Si is assumed to be equal to the original (dark) depletion charge (1.3×10^{11} cm^{-2}) and the width of hole space charge region be equal to the absorption depth (10 µm at 800nm wavelength) minus the dark depletion width (1 µm). Note also that the depletion field switches its polarity around the edge of 2DEG (Fig. 6.4a). With this nearly-suppressed depletion width, an overflowing electron in 2DEG can cross the boundary and recombines with a hole. Through this spill-over process, the channel edge area maintains the peak electron concentration at a stable level. Here we note that the hole space charge in Si and part of the original depletion region now develops a negative voltage drop while other components (V_{ox} and V_{2DEG}) take a positive drop (see Fig. 6.4a, potential profile). Owing to this voltage compensation effect of primarily the hole space charge region, a large internal voltage (~9V, far greater than the applied bias of 2V) develops across the oxide layer and thereby enables the peak electric field in Si to exceed the 1×10^{6} V/cm level.

In this calculation the photoelectron concentration in 2DEG is assumed to be constant (3×10^{18} cm^{-3}) over 37 nm thickness of inversion layer (Fig. 6.4a) [66]. The electric field in Si shows a triangular profile with a peak value ($\varepsilon_{m,Si}$) of 1.5×10^{6} V/cm at the oxide interface. The ionization rates for electrons (α_{n}) and holes (α_{p}) depend on the probability for the carriers to reach the threshold energy [67], and were first calculated from the field distribution. The carrier multiplication factor M_{n} was then calculated, referring to the following relationship [55].

$$M_n = \left\{ 1 - \int_0^W \alpha_n \exp\left[-\int_0^x (\alpha_n - \alpha_p) dx' \right] dx \right\}^{-1}$$

where W is the width of space charge field region. Considering the exponential dependence of ionization rates on field, it is obvious that carrier multiplication occurs primarily in the high-field 2DEG region (within ~20nm effective width) (Fig. 6.4b). The multiplication factor is estimated to be 2.4. The internal quantum efficiency (230%) measured at 808 nm (Fig. 6.3a) shows a good agreement with this model calculation (240%), supporting the proposed mechanism of high-field impact-ionization in 2DEG.

It should also be noted that the measured quantum efficiency remains constant at 530 to 650 nm wavelength (Fig. 6.3a). Photocarriers are generated in the depletion and neutral regions, in which the carrier transport is governed by a drift or diffusion process, respectively. A crossing occurs at ~530nm wavelength, and the diffusion transport becomes dominant over the drift one at longer wavelengths. In the case of current multiplication by photoconductive effect, the current gain is determined by the ratio of carrier lifetime to transit time. Considering the fact that the carrier transit time in the diffusion-limited regime is many orders of magnitude greater than that in the drift regime, the photoconductive gain would then be expected to change dramatically in this spectral range. The observed constancy of quantum efficiency at 530-650nm excludes an involvement of photoconductive effect and corroborates the mechanism of photocarrier multiplication by impact ionization.

Figure 6.4 Photocarrier multiplication in 2DEG: space charge and field distributions, ionization rates, and multiplication factor. **a**, Schematic illustration (drawn not to scale) of space charge, field, and potential profiles at the edge of 2DEG in a graphene/SiO$_2$/p-Si structure under illumination. **b**, Electric field, ionization rates (α_n for electrons and α_p for holes) and multiplication factor calculated for the charge distribution shown in (**a**). 2DEG density of 1×10^{13} cm^{-2} is assumed with 37 nm width. Ionization rates and multiplication were calculated from the resulting field distribution. Strong accumulation of photoelectrons results in high electric field ($\sim1\times10^6$ V/cm) in 2DEG, resulting in carrier multiplication of 240% at low bias (~2V).

6.3.4 Field-assisted hot-carrier multiplication

The appearance of 2nd plateau (300% level at <~650nm) indicates that another multiplication process kicks in with a threshold energy of ~1.9 eV (Fig. 6.3a). This step-increase of IQE (from 230% to 300%) is ascribed to a combined effect of hot-carrier excitation and field-assisted energy gain occurring in 2DEG. In direct-bandgap semiconductors with parabolic bands the ionization threshold energy is known to follow the $1.5E_g$ rule, with E_g being the bandgap energy [68]. Contrastingly, the ionization transition in Si requires a large amount of momentum transfer involving reciprocal-lattice vectors (so-called, the 'umklapp' process) [68, 69]. This 'umklapp' process in Si is known to result in a lower threshold (*i.e.*, $1.0E_g$ as opposed to $1.5E_g$): the electron-initiated ionization in the [100]-direction shows the lowest threshold of 1.1 eV relative to the conduction band minima. The ~1.9-eV photon threshold behaviour observed in the present work then suggests that photoexcited electrons attain extra energy (~0.3 eV) from the field on top of the excess energy (0.8 eV), fulfilling the 1.1-eV threshold requirement for impact ionization (Fig. 6.5). Since the field-assisted energy gaining event must occur on hot carriers before losing the excess energy to phonon scattering, this multiplication process will be most effective where field strength is the highest, that is, in the 2DEG along the SiO_2/Si interface. This multiplication is additive to the process occurring at channel edge, since the photocarriers generated/multiplied in 2DEG area will transport to and pass through the same exit at the edge. The steady rise of quantum efficiency for <400 nm corresponds to the direct bandgap transition of Si, and has been reported in the literature [43, 70]. The enhanced efficiency in UV is ascribed to a carrier multiplication process involving direct-bandgap transitions (Fig. 6.5: Γ-point with energy gap of 3.4 eV).

For a given level of input power, *e.g.*, 0.25 mW in Fig. 6.4, the photocurrent-saturation voltage (V_{sat}) shows a characteristic spectral dependence: a monotonic increase from 2.0 V to 3.8 V in 325-to-850 nm, followed by a decrease to 2.0 V in 980-1064 nm. This can be explained as follows. In the pre-saturation regime ($V < V_{sat}$) the channel current is limited by the electron emission/transport process in the void channel, which is bias-voltage dependent (Fig. 6.2d). In 325-850nm the photogeneration rate increases with increasing wavelength, as can be seen from the responsivity curve (Fig. 6.3a, blue). The increase of photocurrent incurs correspondingly larger saturation voltage. Near band-edge (>850 nm) the absorption of light sharply drops and therefore the photocurrent decreases, resulting in a decrease of saturation bias. It is important to note that the photocarrier multiplication shows no (or weak) dependence on input power for the range tested in this work (0.1-1.0 mW) (Fig. 6.2e). This is explained by that carrier multiplication occurs primarily in the localized region (channel edge), where the photocarriers originating from the entire illuminated area accumulate to the level close to a dielectric breakdown regime.
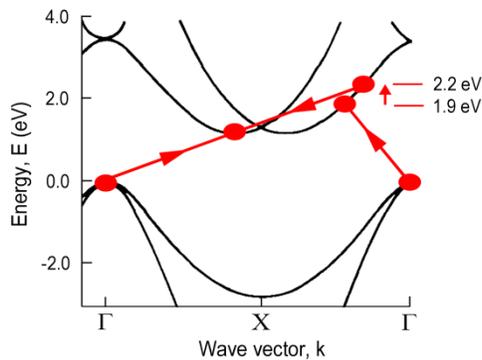
Figure 6.5 Impact ionization by field-assisted and hot-carrier effects. An energy band diagram illustrating the 'umklapp' process in Si. The electrons excited by photons (>~1.9eV) attain extra energy (>~0.3eV) from the field on top of the excess energy (0.8eV) above bandgap. This fulfills the 1.1-eV threshold requirement for impact ionization along [100] direction. This field-assisted and excess-energy effect corresponds to the 2nd plateau at <650nm in Fig. 6.3a. Direct transitions in the Γ-valley (energy gap of 3.4 eV) corresponds to the 3rd step increase of quantum efficiency at <400nm.

6.3.5 Discussion

An enabling nature of our device structure is that a strong field builds up at the edge of a 2DEG layer at low external bias. This can be compared with the n^+-p-π-p^+ reach-through avalanche photodiode (APD) structure, in which a thin p-layer adjacent to the n^+-layer provides extra space charge, enhancing the local depletion field to maximum and thereby inducing avalanche multiplication[2]. Note that in our case the local field enhancement at the channel edge is self-induced by photocarriers. This is contrasting to the APD case where a large external bias is required to form the depletion field and yet the peak electric field is lower than our case.

The broadband photocarrier multiplication phenomenon observed in this work holds an interesting potential for high-efficiency solar cell applications. The maximum open-circuit voltage of solar cells is determined by the work function difference of junction materials (*i.e.*, flat band voltage) and typically ranges around 1 V. The low voltage operation (1.5-2.0 V, reverse bias) of photocarrier multiplication demonstrated in this work is expected to be compatible with photovoltaic operation when the structure is designed to have sufficient built-in field by choosing junction materials with proper work functions. Consider, for example, incorporating low-work-function metal, such as Mg (3.7 eV) or Cs (2.2 eV), as a top electrode on a SiO_2/p-Si structure [71]. The flat band voltage is estimated to be 1.2-2.7 V. This will support sufficient built-in field (*i.e.*, internal reverse bias) for carrier separation in the depletion region and carrier multiplication in the 2DEG layer while allowing a proper amount of open circuit voltage (~1 V, external forward).

6.4   SUMMARY

One of the approaches for high-efficiency PV energy conversion is generating multiple electron-hole pairs when a photon is absorbed. Exploiting this phenomenon for device-level applications, however, has been hampered by intrinsic difficulties, such as excessively large field/bias requirement or low throughput in extracting generated carriers out of nanocrystals. We have developed low-external-voltage and yet high-internal-field impact-ionization carrier multiplication in a 2DEG layer induced in a graphene/oxide/Si structure.

A graphene/SiO_2/Si structure with a void channel was fabricated by employing electron-beam lithography, plasma etching, and graphene transfer processes. In brief, a vertical trench structure (340 nm width, 210 nm depth, 1-mm trench length) was formed by plasma reactive ion etching (RIE) of a 23-nm-thick-SiO_2-covered (100)-Si substrate (p-type doped with resistivity of 10 Ω-cm). A monolayer graphene (3mm x 4mm) was then transferred to the trench-etched substrate.

We have investigated low-voltage (<~2V) broadband photocarrier multiplication in a graphene/SiO_2/Si structure that demonstrates external quantum efficiency 146-200% (internal quantum efficiency 218-384%) as measured with photocurrent in UV-to-NIR (325-850nm). A two-dimensional electron gas (2DEG) channel induced at Si/SiO_2 is utilized as a conduit for carrier confinement and transport in conjunction with use of a vertical trench covered with suspended graphene for low-voltage emission of electrons. Photoelectrons, separated by depletion field, accumulate at the channel edge to the level of 1×10^{13} cm^{-2}. The self-induced electric field (~10^6 V/cm) in 2DEG enables impact ionization at low bias, in the way promising and compatible with photovoltaic operation.

7.0   CONCLUSIONS

In this thesis, we have investigated a new method of light coupling for high-efficiency solar cells. The scope of this study covers simulation, design, fabrication and characterization of vertical dipole nano-optic structure.

Conventional refractive transmission at a dielectric interface limits the maximum angle of transmission to be small in high-index media. The proposed vertical dipole nanostructures mitigate these fundamental issues and provide maximum synergistic effects among the elemental processes for the benefit of achieving enhanced conversion efficiencies. In order to corroborate the proposed concept, radiation patterns of a nanoscale vertical dipole placed on or underneath a dielectric surface have been modeled and calculated. When the vertical dipole is placed in the air side on the surface of SiN, Si and Ag, a tilt radiation $(30 - 40$ deg$)$ is observed for all three cases. A vertical dipole nanoaperture was formed on metal (Ag) surface to experimentally confirm the oblique transmission pattern. The main lobe from the nanoaperture scanned by NSOM was tilted $\sim 45^o$, well matching the model simulation. When the vertical dipole is placed underneath a dielectric surface (Si), the main lobe is tilt-oriented to ~ 50 deg. This tilt angle is significantly greater than the conventional refraction limit (~ 15 deg for air/Si interface). The radiation patterns for both cases are composed of the direct propagation and the reflection components. The radiation pattern of a vertical dipole embedded in the passivation layer of Si demonstrates enhanced transmission angle and intensity compared to those of the air/Si case.

127

To demonstrate the beneficial effects of vertical-dipole nano-optic structures, one-dimensional grating structures were fabricated by holographic lithography. Gratings were formed by constructive and destructive interference from holographic lithography. For the final electronic structure, the fabrication process involved holographic lithography followed by plasma reactive ion etching. The reflectance measurement was performed on grating surface at 633 nm wavelength. As the grating period decreases from 720 nm to 270 nm, the reflectance significantly decreases down to 4 %. Since the grating period is much smaller than the wavelength of light, high-order diffractions are suppressed, resulting in low reflectance. Vertical dipoles formed at facet edges re-radiate the incident light into the medium with glancing angle that is beneficial for reducing reflectance. The prototype solar cell with 270 nm grating period performed better (15 %) than the planar cell (8 %). We have applied two-dimensional nanoscale vertical dipoles on finished Si cells and demonstrated a major improvement of cell efficiency. Pyramid-textured surface with vertical dipole make glancing coupling which increases the path length of light and also alleviates the lensing effect of pyramid-textured surface. In order to implement the vertical dipole structure on finished c-Si cells, two approaches have been explored: One is using self-organized Ag nano-disks and the other one is using TiO_2 nanoislands. First, self-organized Ag nano-particles are applied to pyramid-textured finished cell surface by the thermal deposition, annealing and RIE process. These nano-textured structures serve as vertical dipoles, therefore reduce the reflectance optically and enhance the photocurrent electrically. The efficiency of the cell improved from $13 - 14$ % (without nanostructure) to $16 - 17$ % (with nanostructure). In order to overcome/bypass the issues associated the meta-assisted etching phenomenon, we have further studied the non-etching process based on reactively

sputtered AgO nanoparticles. Improvement on conversion efficiency was observed in this case, too.

A TiO$_2$-basedvertical-dipole nano-optic structure was developed as an alternative to the Ag nanoislands approach. At the nucleation stage of TiO$_2$ film, discontinuous TiO$_2$ nanoislands can be formed. They are used as an etch mask on a SiN passivation layer so that narrow trenches/holes (vertical dipole structure) are fabricated into SiN layer. By adjusting RIE time, an optimum etch depth was determined that produces the lowest reflectance. The optimum etching condition, when applied to c-Si cells, demonstrate the largest amount of photocurrent and the highest cell efficiency. The efficiency increases from 16.3 % with a reference cell (control cell without vertical dipoles) to 19.8 % with a processed cell. This major improvement is ascribed to the photocurrent increase observed with vertical dipole structures. From EQE and IQE measurement, the improvement came from the longer wavelength region (600-1100nm) of solar spectrum.

Finally, we have investigated impact-ionization carrier multiplication in a 2DEG layer with low-external-voltage and high-internal-field in a graphene/oxide/Si structure. The electron-beam lithographye and plasma reactive ion etching processes were employed to form the graphene/SiO$_2$/Si with a nanoscale void channel. Dark and photo *I-V* characteristics were analyzed. Spectral dependence of photocarrier multiplication, impact ionization in 2DEG and field-assisted hot-carrier multiplication were studied to understand the underlying mechanisms. With the graphene/SiO$_2$/Si structure, external quantum efficiency 146-200% (internal quantum efficiency 218-384%) was achieved as measured with photocurrent in UV-to-NIR (325-850nm) with low-voltage ($<\sim2V$). Strong accumulation of photoelectrons (1×10^{13} cm^{-2}) enables high electric field ($\sim1\times10^6$ V/cm) in 2DEG. The low-voltage broad-band photocarrier multiplication is

compatible with a photovoltaic operation and is promising for potentially very high efficiency solar cells.

BIBLIOGRAPHY

[1]   "Global Market Outlook for Photovoltaics 2014-2018". *EPIA-publications*. European Photovoltaic Industry Association. March 2014. Archived from the original on 4 April 2014.

[2]   M. A. Green and M. J. Keevers, "Optical properties of intrinsic silicon at 300 K", Prog Photovolt: Res. Appl. 3, 189 (1995).

[3]   T. Tiedje, E. Yablonovitch, G. D. Cody, and B. G. Brooks, "Limiting efficiency of silicon solar cells," IEEE Trans. Electron Devices 31, 711-716 (1984).

[4]   H. A. Atwater and A. Polman, "Plasmonics for improved photovoltaic devices," Nature Mater. 9, 205-213 (2010).

[5]   Z. Yu, A. Raman, and S. Fan, "Fundamental limit of nanophotonic light trapping in solar cells," PNAS 107, 17491 (2010).

[6]   S. Jeong, S. Wang, and Y. Cui, "Nanoscale photon management in silicon solar cells," J. Vac. Sci. Technol. A 30, 060801 (2012).

[7]   F. Priolo, T. Gregorkiewicz, M. Galli, and T. F. Krauss, "Silicon nanostructures for photonics and photovoltaics," Nature Nanotechnol. 9, 19-32 (2014).

[8]   R. B. Stephens and G. D. Cody, "Optical reflectance and transmission of a textured surface," Thin Solid Films 45, 19-29 (1977).

[9]   M. D. Kelzenberg et al., "Enhanced absorption and carrier collection in Si wire arrays for photovoltaic applications," Nature Mater. 9, 239-244 (2010).

[10]   E. Garnett and P. Yang, "Light trapping in silicon nanowire solar cells," Nano Lett. 10, 1082-1087 (2010).

[11]   S. E. Han and G. Chen, "Optical absorption enhancement in silicon nanohole arrays for solar photovoltaics," Nano Lett. 10, 1012-1015 (2010).

[12]   S. Koynov, M. S. Brandt, and M. Stutzmann, "Black nonreflecting silicon surfaces for solar cells," Appl. Phys. Lett. 88, 203107 (2006).

[13] H.-C. Yuan, V. E. Yost, M. R. Page, P. Stradins, D. L. Meier, and H. M. Branz, "Efficient black silicon solar cell with a density-graded nanoporous surface: optical properties, performance limitations, and design rules," Appl. Phys. Lett. 95, 123501 (2009).

[14] H. M. Branz, V. E. Yost, S. Ward, K. M. Jones, B. To, and P. Stradins, "Nanostructured black silicon and the optical reflectance of graded-density surfaces," Appl. Phys. Lett. 94, 231121 (2009).

[15] F. Toor, H. M. Branz, M. R. Page, K. M. Jones, and H.-C. Yuan, "Multi-scale surface texture to improve blue response of nanoporous black silicon cells," Appl. Phys. Lett. 99, 103501 (2011).

[16] J. Oh, H.-C. Yuan, and H. M. Branz, "An 18.2%-efficient black-silicon solar cell achieved through control of carrier recombination in nanostructures," Nature Nanotechnology 7, 743–748 (2012).

[17] M. A. Green, "Surface Texturing and Patterning in Solar Cells", in Advances in Solar Energy, edited by M. Prince (American Solar Energy Society, Boulder, 1993), Vol. 8, pp. 231-269.

[18] A. Rohatgi and P. Rai-Choudhury, "Design, fabrication, and analysis of 17-18% efficiency surface-passivated silicon solar cells," IEEE Trans. Electron Devices 31, 596-601 (1984).

[19] M. Otto, M. Kroll, T. Käsebier, R. Salzer, A. Tünnermann, and R. B. Wehrspohn, "Extremely low surface recombination velocities in black silicon passivated by atomic layer deposition," Appl. Phys. Lett. 100, 191603 (2012).

[20] J. Zhao, A. Wang, P. P. Altermatt, S. R. Wenham, M. A. Green, "24% efficient perl silicon solar cell: Recent improvements in high efficiency silicon cell research", Sol. Energy Mat. Sol. Cells 41-2, 87 (1996).

[21] J. Nelson, The Physics of Solar Cells (Imperial College Press, 2003).

[22] Lindholm FA, Fossum JG, Burgess EL. Application of the superposition principle to solar-cell analysis. IEEE Transactions on Electron Devices. 1979 ;26:165–171.

[23] M. Born and E. Wolf, Principles of Optics, 7th ed. (Cambridge University Press, Cambridge, 1999).

[24] G. Brucoli and L. Martín-Moreno, "Comparative study of surface plasmon scattering by shallow ridges and grooves," Phys. Rev. B 83, 045422 (2011).

[25] Y. S. Jung, J. Wuenschell, T. Schmidt, and H. K. Kim, "Near- to far-field imaging of free-space and surface-bound waves emanating from a metal nanoslit", Appl. Phys. Lett. 92, 023104 (2008).

[26] Y. S. Jung, Y. Xi, J. Wuenschell, and H. K. Kim, "Near- to far-field imaging of phase evolution of light emanating from a metal nanoslit", Opt. Express 16, 18875-18882 (2008).

[27] J. D. Jackson, Classical Electrodynamics, 3rd ed. (Wiley, Hoboken, 1999).

[28] C. V. Shank, and R. V. Schmidt, "Optical technique for producing 0.1-μ periodic surface structures", Appl. Phys. Lett. 23, 154 (1973).

[29] Y. Xi, Y. S. Jung, and H. K. Kim, "Interaction of light with a metal wedge: the role of diffraction in shaping energy flow", Opt. Express 18, 2588-2600 (2010).

[30] P. Yeh, Optical Waves in Layered Media (Wiley, 2005)

[31] SOPRA N&K Database.

[32] M.C. Hutley, Diffraction Gratings (Academic Press, 1982).

[33] M. A. Green, "Limits on the open-circuit voltage and efficiency of silicon solar cells imposed by intrinsic Auger processes," IEEE Trans. Electron Devices 31, 671-678 (1984).

[34] P. Campbell and M. A. Green, "The limiting efficiency of silicon solar cells under concentrated sunlight," IEEE Trans. Electron Devices 33, 234-239 (1986).

[35] S. Pillai, K. R. Catchpole, T. Trupke, and M. A. Green, "Surface plasmon enhanced silicon solar cells", J. Appl. Phys. 101, 093105 (2007).

[36] Z. Huang, N. Geyer, P. Werner, J. de Boor, and U. Gösele, "Metal-assisted chemical etching of silicon: a review," Adv. Mater. 23, 285-308 (2011).

[37] M. A. Green, and K. Emery "Solar cell efficiency tables", Prog. Photovolt. Res. Appl. 1, 25 (1993).

[38] W. K. Choi, T. H. Liew, and M. K. Dawood, "Synthesis of Silicon Nanowires and Nanofin Arrays Using Interference Lithography and Catalytic Etching", Nano Lett. 8, 3799 (2008).

[39] T. James, Y. V. Kalinin, C-C Chan, J. S. Randhawa, M Gaevski, and D. H. Gracias, "Voltage-Gated Ion Transport through Semiconducting Conical Nanopores Formed by Metal Nanoparticle-Assisted Plasma Etching", Nano Lett. 12, 3437 (2012).

[40] B. S. Richards, J. E. Cotter, C. B. Honsberg, and S. R. Wenham, "Novel uses of TiO_2 in crystalline silicon solar cells", Proc. IEEE 28, 375-378 (2000).

[41] Robbins, D. J. Aspects of the theory of impact ionization in semiconductors (I). *Phys. Stat. Sol. B* **97**, 9-50 (1980).

[42]   Ruegg, H. W. An optimized avalanche photodiode. *IEEE Trans. Electron Devices* **14**, 239-251 (1967).

[43]   Kolodinski, S. *et al.* Quantum efficiencies exceeding unity due to impact ionization in silicon solar cells. *Appl. Phys. Lett.* **63**, 2405-2407 (1993).

[44]   Califano, M., Zunger, A. & Franceschetti, A. Direct carrier multiplication due to inverse Auger scattering in CdSe quantum dots. *Appl. Phys. Lett.* **84**, 2409-2411 (2004).

[45]   Schaller, R. D. & Klimov, V. I. High efficiency carrier multiplication in PbSe nanocrystals: implications for solar energy conversion. *Phys. Rev. Lett.* **92**, 186601 (2004).

[46]   Ellingson, R. J. *et al.* Highly efficient multiple exciton generation in colloidal PbSe and PbS quantum dots. *Nano Lett.* **5**, 865-871 (2005).

[47]   Sukhovatkin, V. *et al.* Colloidal quantum-dot photodetectors exploiting multiexciton generation. *Science* **324**, 1542-1544 (2009).

[48]   Gabor, N. M. *et al.* Extremely efficient multiple electron-hole pair generation in carbon nanotube photodiodes. *Science* **325**, 1367-1371 (2009).

[49]   Beard, M. C. *et al.* Comparing multiple exciton generation in quantum dots to impact ionization in bulk semiconductors: implications for enhancement of solar energy conversion. *Nano Lett.* **10**, 3019-3027 (2010).

[50]   Winzer, T., Knorr, A. & Malic, E. Carrier multiplication in graphene. N*ano Lett.* **10**, 4839-4843 (2010).

[51]   Semonin, O. E. *et al.* Peak external photocurrent quantum efficiency exceeding 100% via MEG in a quantum dot solar cell. *Science* **334**, 1530-1533 (2011).

[52]   Tielrooji, K. J. *et al.* Photoexcitation cascade and multiple hot-carrier generation in graphene. *Nature Phys.* **9**, 248-252 (2013).

[53]   Gabor, N. M. Impact excitation and electron–hole multiplication in graphene and carbon nanotubes. *Acc. Chem. Res.* **46**, 1348-1357 (2013).

[54]   Congreve, D. N. *et al.* External quantum efficiency above 100% in a singlet-exciton-fission-based organic photovoltaic cell. *Science* **340**, 334-337 (2013).

[55]   Sze, S. M. *Physics of Semiconductor Devices* 2nd edn (Wiley, 1981).

[56]   Srisonphan, S., Jung, Y. S. & Kim, H. K. Metal-oxide-semiconductor field-effect transistor with a vacuum channel. *Nature Nanotechnol.* **7**, 504-508 (2012).

[57]   Srisonphan, S., Kim, M. & Kim, H. K. Space charge neutralization by electron-transparent suspended graphene. *Sci. Rep.* **4**, 3764 (2014).

[58]   Zhou, Y. *et al.* A universal method to produce low-work function electrodes for organic electronics. *Science* **336**, 327-332 (2012).

[59]   Pospischil, A., Furchi, M. M. & Mueller, T. Solar-energy conversion and light emission in an atomic monolayer p-n diode. *Nature Nanotechnol.* **9**, 257-261 (2014).

[60]   Child, C. D. Discharge from hot CaO. *Phys. Rev.* **32**, 492-511 (1911).

[61]   Langmuir, I. The effect of space charge and residual gases on thermionic currents in high vacuum. *Phys. Rev.* **2**, 450-486 (1913).

[62]   Langmuir, I. & Kingdon, K. H. Thermionic effects caused by alkali vapors in vacuum tubes. *Science* **57**, 58-60 (1923).

[63]   Law, M. E. *et al.* Self-consistent model of minority-carrier lifetime, diffusion length, and mobility. *IEEE Electron Device Lett.* **12**, 401-403 (1991).

[64]   Das, A. *et al.* Monitoring dopants by Raman scattering in an electrochemically top-gated graphene transistor. *Nature Nanotechnol.* **3**, 210-215 (2008).

[65]   Ponomarenko, L. A. *et al.* Cloning of Dirac fermions in graphene superlattices. *Nature* **497**, 594-597 (2013).

[66]   King, Y.-C. *et al.* DC electrical oxide thickness model for quantization of the inversion layer in MOSFETs. *Semicond. Sci. Technol.* **13**, 963-966 (1998).

[67]   Van Overstraeten, R. & de Man, H. Measurement of the ionization rates in diffused silicon p-n junctions. *Solid State Electron.* **13**, 583-608 (1970).

[68]   Anderson, C. L. & Crowell, C. R. Threshold energies for electron-hole pair production by impact ionization in semiconductors. *Phys. Rev. B* **5**, 2267-2272 (1972).

[69]   Sano, N. & Yoshii, A. Impact-ionization theory consistent with a realistic band structure of silicon. *Phys. Rev. B* **45**, 4171-4180 (1992).

[70]   Geist, J., Gardner, J. L. & Wilkinson, F. J. Surface-field-induced feature in the quantum yield of silicon near 3.5 eV. *Phys. Rev. B* **42**, 1262-1267 (1990).

[71]   Deal, B. E., Snow, E. H. & Mead, C. A. Barrier energies in metal-silicon dioxide-silicon structures. *J. Phys. Chem. Solids*. **27**, 1873-1879 (1966).

[72]   Jung, Yun Suk. Study of Plasmonic Phenomena in Metal Nanostructure Arrays, PhD Thesis, University of Pittsburgh (2009).

[73]   Xi, Yonggang. Electromagnetic Theory and Simulations of Optical Interactions with Metal Nanostructures. PhD Thesis, University of Pittsburgh (2010).